Physicochemical Study of Automotive Catalysts for Emission Control(Dissertation_全文)

AUTHOR(S):

Nagai, Yasutaka

CITATION:

Nagai, Yasutaka. Physicochemical Study of Automotive Catalysts for Emission Control. 京都大学, 2007, 博士(工学)

ISSUE DATE:

2007-07-23

URL:

https://doi.org/10.14989/doctor.r12102

Physicochemical Study of Automotive Catalysts for Emission Control

YASUTAKA NAGAI

2007

Preface

This thesis is concerning the automotive catalysts to remove the harmful emission from automotive engines. Today, the automobile society is growing on the global scale, and vehicles are essential to make our living more convenient and richer. On the other hand, vehicles have a great effect on the global environment and natural resources. Recently, due to increasing demands for global environmental protection, more stringent regulations have been imposed on the automobile industry. Automobile companies are striving to purify automobile exhaust emissions. Consequently, there is a strong demand to produce more advanced automotive catalysts by technical innovation. Here, the author presents the physicochemical study of automotive catalysts. Using advanced analysis techniques such as synchrotron radiation analysis can make it possible to design catalysts for practical use, rather than adopting a trial-and-error approach. The author hopes that his studies can pave the way for planed catalytic design in the future. In the near future, this approach of designing catalysts at an atomic level by using advanced synchrotron radiation analysis must enable the realization of an ultimate clean car which completely removes harmful components from exhaust gases.

The present study has been carried out in the catalyst laboratory at the TOYOTA Central R&D Labs. Inc. (TCRDL) during the years 1999-2006. During this time, the author has been in charge of the development of new automotive catalysts. The main subject of his work was “Synchrotron radiation analysis of automotive catalysts”. The aims of the project were the knowledge on the relationship between catalytic activity and the atomic structure, and the development of more advanced catalysts. The author started the synchrotron radiation analysis at SPring-8 (Hyogo, Japan) in 1999. After that, he also carried out the synchrotron radiation experiment at ESRF (Grenoble, France)

and PF (Tsukuba, Japan). The author has met many people and gained a lot of experience.

The author would like to thank his supervisors, Drs. Masahiro Sugiura and Hirofumi Shinjoh and Mr. Hideo Sobukawa, the heads of the catalyst laboratory at TCRDL, for offering him an opportunity to work in the field of automotive catalyst. The author is also grateful to Dr. Shin'ichi Matsumoto at TOYOTA Motor Corporation (TMC) for giving him a chance to learn the advanced research on automotive catalysts. The author's supervisors have given the instruction of "TOYOTA-Way" to him.

The author is grateful to Professors Satohiro Yoshida, Takuzo Funabiki and Tsunehiro Tanaka for their teaching to grow him up at Kyoto University. The author would give his special thanks to Professor Tsunehiro Tanaka for the comments and clarifications regarding his present thesis, publications and manuscripts. In addition, Professor Tsunehiro Tanaka built up the author's basic knowledge of XAFS analysis in his university days.

The author would also like to thank all of co-researchers, especially Professor Tokuhiko Okamoto, Drs. Akihiko Suda and Takamasa Nonaka, Messrs. Kazuhiko Dohmae, Toshitaka Tanabe, Naoki Takahashi at TCRDL, Takeshi Hirabayashi, Nobuyuki Takagi at TMC, Yasuo Ikeda, Takashi Kuzuya, Naoyuki Hara and Ms. Muriel Lepage at TOYOTA Motor Europe, and Dr. Paul Fanson at TOYOTA Technical Center, USA. They are his dear friends as well as his colleagues. The author owes his sincere thanks to people at SPring-8, ESRF and PF, especially to Drs. Tomoya Uruga (SPring-8)

and Sakura Pascarelli (ESRF) and Professor Masaharu Nomura (PF) for their excellent work.

The author tenders his warmest thanks to his parents, his brother, and his grandmother for their generous aid and encouragement throughout his life as a researcher. Finally, his heartfelt gratitude is due to his loving wife Momoko and to their little Asumi and Chikara for continuous loving support and encouragement. Without the affection of his family, this thesis might not have existed.

Yasutaka Nagai

Aichi,

March, 2007

- CONTENTS -

Chapter 1: General introduction;
~Automotive catalysts for emission control~

History of automotive catalysts

In 1955, smog in Los Angels was worse than it is in Mexico City today [1]. Along with a sharp increase of vehicles in use from 1950s, automobile pollution problem surfaced in the urban areas. In the USA, a stringent automobile emission control law called Muskie Act was enacted and Japan followed suit. Table 1 shows the automotive emission regulation value in the USA and Japan. These regulations required over 90 percent reduction in hydrocarbon (HC), carbon monoxide (CO) and nitrogen oxide (NOx) emissions over uncontrolled levels. At that time the technology needed to meet those standards did not exist.

Table 1. Emission regulations in the USA and Japan

	USA (Muskie Act)[1)] [g/mile]	Japan (1978 regulation)[2)] [g/km]
Hydrocarbon (HC)	0.41	0.25
CO	3.4	2.1
NOx	0.4	0.25

[1)] LA(Los Angels)#4 mode examination
[2)] Japan 10 mode examination

Various studies on emission purification device were conducted to overcome this standard. A lot of attempt such as engine modification, exhaust gas recirculation system, manifold reactor, fuel reforming, catalytic converter and so on were explored. It was found from these studies that a catalyst device was most effective method of clearing these stringent emission controls. In 1974, the first catalyst was installed in the form of catalytic converters on vehicles to meet the 1975 control regulations in Japan and the 1975 model control in the USA. The first product was so-called oxidation catalyst that purifies unburned HC and CO in the exhaust gas into harmless CO_2 and H_2O by reaction with oxygen. Next product was the three-way catalyst (TWC) that reduces NOx into harmless N_2 in addition to the function of oxidation catalyst. This type of catalyst was put into practical use in 1977 as the first established catalyst technology for vehicular exhaust emission control. Since then, the use of the TWC system has spread rapidly. Today, it has been implemented in production on almost gasoline powered vehicles around the world [2]. TWCs could reduce the harmful emission to one-tenth of uncontrolled emission level. They have played an important role in environmental protection.

Recently, due to increasing demands for global environmental protection, emission regulations have strengthened step by step on a world scale. Examples of emission standards of recent years in Europe, USA and Japan are presented in Figure 1. The severest stage under these standards demands the emission to be reduced to one-hundredth of uncontrolled emission level. These more stringent standards have been imposed on the automobile industry. Automobile companies are striving to purify automobile exhaust emissions. Consequently, there is a strong demand to produce more advanced TWCs by technical innovation.

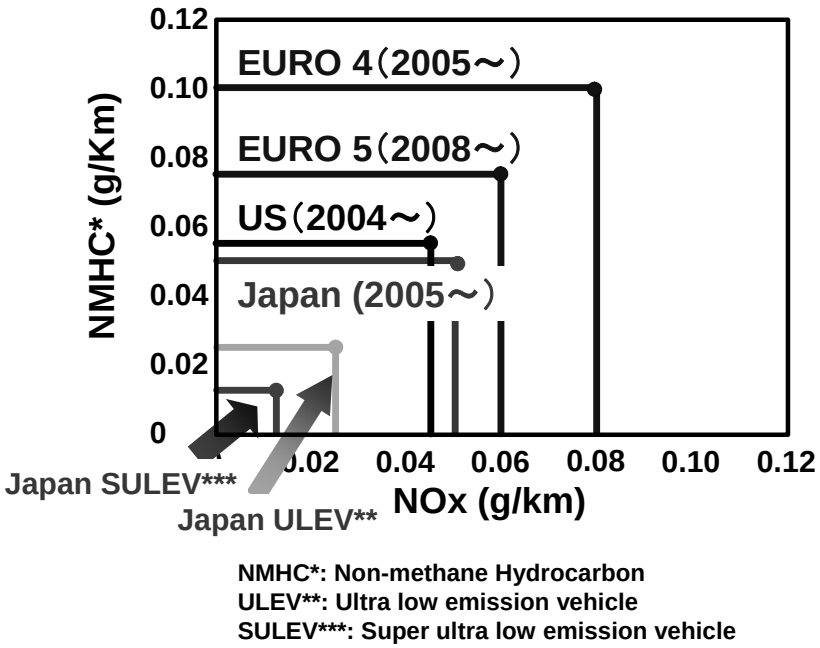

Figure 1. Outline of emission standards in Europe, USA and Japan.

Features of automotive catalysts

Automotive exhaust gases formed in the gasoline engines contain environmentally harmful compounds. Air-to-fuel ratio (A/F) contributes significantly to the concentrations of exhaust gases. Figure 2 presents an example of the concentration of CO, NOx , HC and O_2 from gasoline engine as a function of A/F [3].

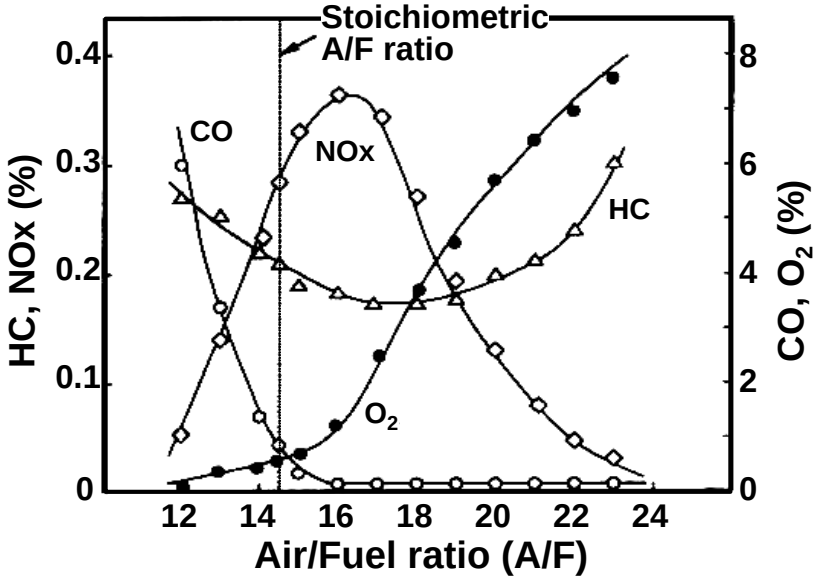

Figure 2 Example of concentration of CO, NOx, HC and O_2 from gasoline engine as a function of air to fuel ratio.

TWCs can efficiently purify harmful automobile emissions such as unburned HC, CO and NOx into harmless CO_2, N_2 and H_2O. TWC converter has three simultaneous tasks (the name "three-way catalyst" derives its origin from this function):

1. Reduction of nitrogen oxides to nitrogen and oxygen: $2NOx \rightarrow xO_2 + N_2$
2. Oxidation of carbon monoxide to carbon dioxide: $2CO + O_2 \rightarrow 2CO_2$
3. Oxidation of unburned HC to carbon dioxide and water: $CxHy + nO_2 \rightarrow xCO_2 + mH_2O$

Figure 3 shows the removal efficiency of TWC as a function of A/F. The purifications of CO, HC and NOx occur most efficiently when the catalytic converter receives exhaust from an engine running at the stoichiometric point. This is 14.6 parts oxygen to 1 part fuel, by weight, for gasoline. When there is more oxygen than required, then the engine is running lean, and the system is in oxidizing condition. In that case, the converter's

two oxidizing reactions (oxidation of CO and HC) are favored, at the expense of the reducing reaction. When there is excessive fuel, then the engine is running rich. The reduction of NOx is favored, at the expense of CO and HC oxidation. If an engine could be held at the strict stoichiometric point for the fuel used, it is theoretically possible to reach almost 100% conversion efficiencies.

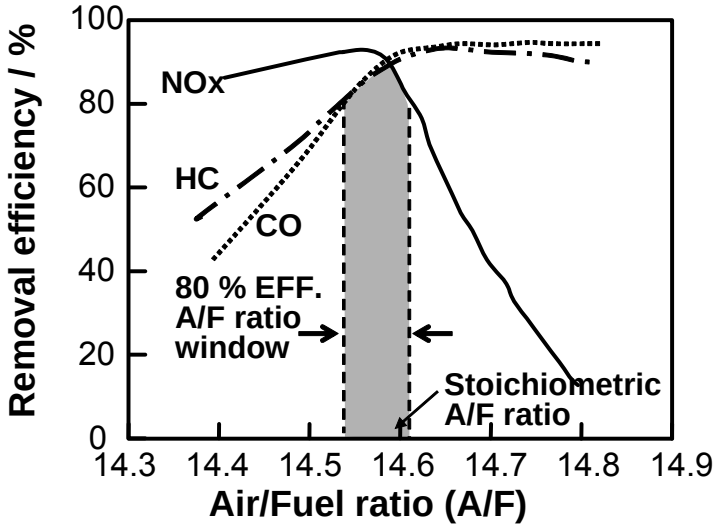

Figure 3. Removal efficiency of TWC as a function of air to fuel ratio.

In order to keep the A/F ratio within the high efficiency window (as presented in Figure 3), the currently-used TWC system consists of a catalytic converter and an electronically controlled A/F management system as shown in Figure 4. The oxygen sensor measures the net oxygen content that is proportional to stoichiometry in the exhaust gas. By using an air flow meter and electronic fuel injection (EFI), the air inlet and fuel injection are controlled to provide a stoichiometric ratio between air and fuel.

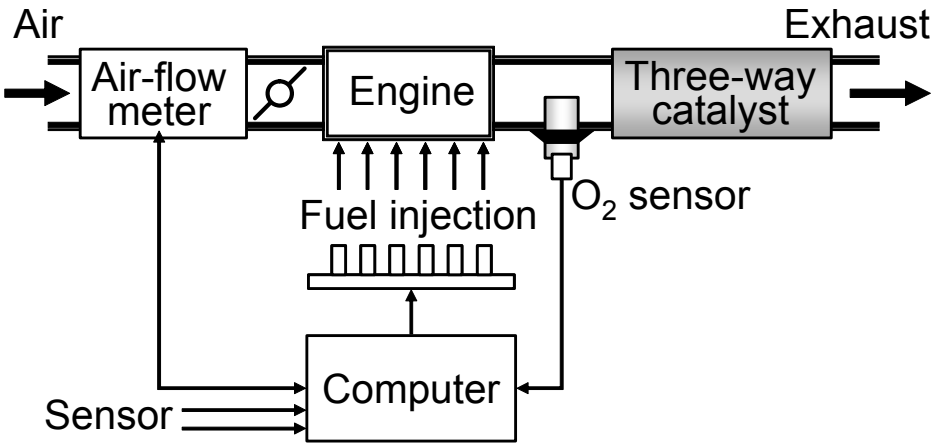

Figure 4. TOYOTA EFI (Electronic Fuel Injection) engine control system

Basically, TWC converter is placed in exhaust manifold and/or under floor of a vehicle. Two different types of TWC converters have been used on vehicles. Some early vehicles used a palletized TWC that was constructed of catalyst coated pellets tightly packed in a sealed shell, while later model vehicles are equipped with a monolith type converter that uses a honeycomb shaped catalyst element. Today, a monolith type becomes main stream, because the monolith design creates less exhaust backpressure and provides ample surface area to efficiently convert feed gases. The monolith support is made either from metallic (stainless steel) or ceramic (cordierite made of $2MgO•2Al_2O_3•5SiO_2$) material. The structure of a cordierite monolith is presented in Figure 5. The monolith contains small channels, each about 1 mm in diameter (300-600 channels per square inch). The wash coat, which includes the active catalyst material, is impregnated on these channel walls. The thickness of the washcoat layer is circa 20-60 μm. The wash coat of three-way catalysts are composed of three main components, namely, a precious metal such as Pt, Pd and Rh, a support such as Al_2O_3, and an oxygen

storage component which is generally a ceria-based oxide [4-6]. The precious metal particles in fresh catalysts are a few nanometers in diameter and are dispersed on a support oxide with a high surface area. These precious metals function as active sites for catalytic reaction to extract harmful components from automotive exhausts, such as NOx, CO, HC. The oxygen storage/release capacity (OSC) is one of the important functions required for TWCs. Although the A/F is controlled to provide a stoichiometric ratio with the EFI system, the oscillation cycle of the engine's A/F fluctuates close to the stoichiometric value, because of the feedback system. Under these conditions, the high OSC is of crucial importance. In the TWCs, Ceria-based oxide is widely used as a promoter due to its high OSC based on the reversible redox reaction ($CeO_2 \leftrightarrow CeO_{2-x} + x/2\ O_2$; $x = 0 - 0.5$) [4]. Ceria stores oxygen under oxygen excess conditions, and releases it under oxygen deficient conditions in order to maintain the stoichiometry. The recent use of large levels of Ceria-based promoters provides a way to increase the efficiency of TWC's by enlarging the air-to-fuel operating window as shown in Figure 3. Therefore, the development of OSC materials is one of important research in automotive catalysts.

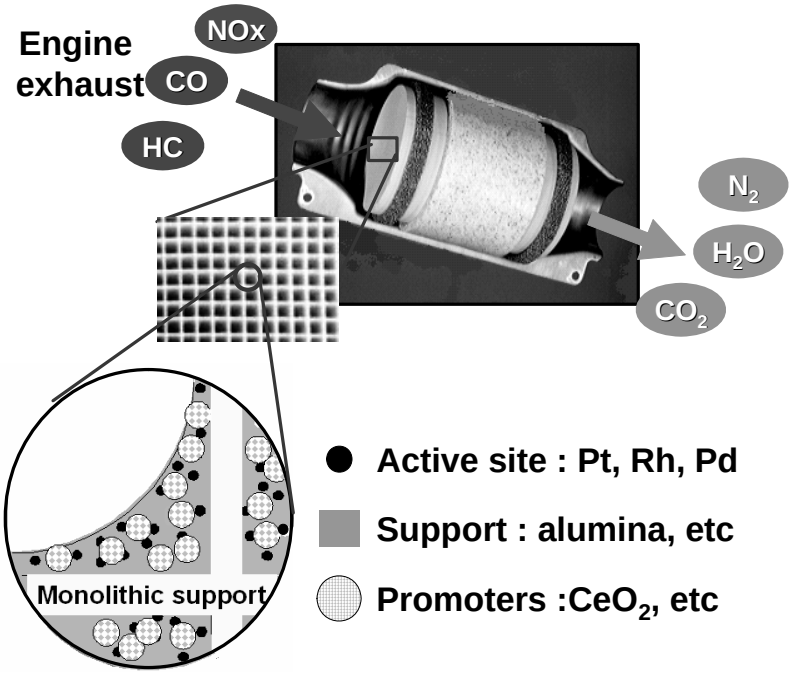

Figure 5. The structure of a monolithic exhaust gas catalyst.

TWCs operate under dynamic and fluctuating conditions and catalytic reactions occur at normal exhaust gas temperatures which, in warmed-up gasoline engines, can vary from 300 °C to 400 °C during idle, even up to about 1000–1100 °C, depending on the driving conditions. When a TWC is exposed to a high temperature of about 800 °C or greater, the precious metal will agglomerate and sinter, reducing the active surface area of the catalyst [7-10]. Generally, sintering of the precious metal particles during operation is mainly considered to reduce the catalytic activity, that is, degrade the catalyst. Therefore, the development of advanced catalysts without the sintering of precious metal particles is required to maintain the high catalytic performance for long period.

Roles of automotive catalysts in reducing fuel consumption

Global warming is one of the crucial environmental issues presently facing the world, and its solution calls for the reduction of CO_2 emission and specifically for the improvement of fuel economy of vehicles. Lean combustion engines such as gasoline lean-burn and diesel are known to be highly effective in improving fuel economy. However, the conventional TWCs cannot perform NOx purification in the lean air-fuel combustion zone, because removal of NOx in an oxygen-rich exhaust is extremely difficult. Hence, new approaches for treating the NOx emissions from diesel and gasoline lean-burn engines are needed [11, 12]. This situation for gasoline lean-burn engines has prompted the research the development of a new catalyst technology that is capable of reducing NOx in excess oxygen, that is, the NOx storage-reduction (NSR) catalyst [13, 14]. As shown in Figure 6, the catalysts most commonly used for NOx storage applications comprise combinations of precious metals for oxidation and reduction purposes and barium oxide/carbonate as the storage material. During the lean period of usual driving, NOx is oxidized on the precious metal, react with the storage component, and then NOx is stored as nitrate. On the other hand, in the rich periods, the NOx stored in the lean periods is decomposed and subsequently reduced to nitrogen on the precious metal. The NSR catalyst for gasoline lean-burn engines has been put to practical use in 1994 in Japan [15].

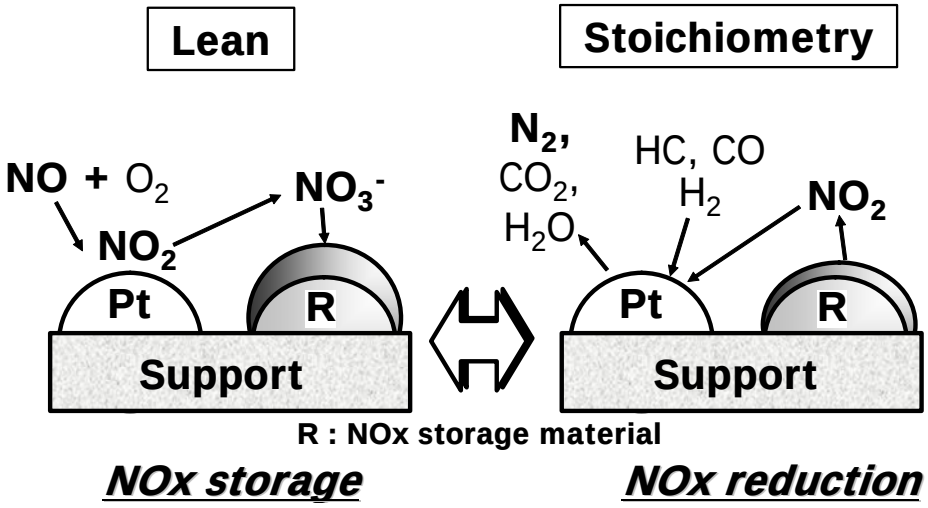

Figure 6. Schematic illustration of NOx storage reduction (NSR) catalyst .

For a long time it was not necessary to apply any exhaust catalyst in diesel engines to meet existing emission standards, since the engine-out gaseous emissions NOx, HC and CO have been much lower than those of gasoline engines. However, with the great development progress of TWC for gasoline engines, the diesel engines' exhaust gas emissions are coming under increasing public pressure all over the world, and reducing tailpipe gaseous emissions, particularly NOx is now one of the main task in diesel engine development. Additionally, the emission characteristics for the gasoline and diesel engines are quite different. Diesel emissions are composed of three phases in contrast to the single gaseous phase emissions of a gasoline engine:

1) Solids (dry carbon or soot)

2) Liquids (soluble liquid organic fraction and liquid sulphate)

3) Gases (CO, HC, NOx, SO_2, etc.)

Diesel particulate filters (DPF) with oxidation catalysts have been used for reducing HC,

CO and particulate matter in the exhaust of diesel engines [16]. Any sulfur compound contained in the diesel fuel is oxidized to SO_2 during the engine combustion cycle. In the presence of an oxidation catalyst, SO_2 is further oxidized to SO_3, which quickly reacts with the moisture in the exhaust to form sulfate [17]. The sulfate leads to an increase in the weight of the total particulates emitted from the diesel engine and also causes acid rain. Therefore, a highly selective oxidation catalyst, which has a higher oxidation activity for carbon, CO and HC compounds than that for SO_2, is required.

Conservation of precious metal resources

Movement of strengthening emission regulations is spreading universally not only to Japan, USA and Europe, but to Asia, Central and South America, Oceania and so on. Therefore, the demand for automotive catalysts attached to vehicles is increasing. It is expected to invite an increased consumption of precious metals which are the active components of automotive catalysts. The precious metals demand in Figure 7 shows that the use for automotive catalysts account for a large portion in each of Pt, Pd and Rh. Especially, 80 % and more of Rh consumption is used for automotive catalysts. Additionally, as shown in Figure 8, the total demand of precious metals trend to increase basically year by year. Effective use of these limited resources is important task imposed on the automobile industry.

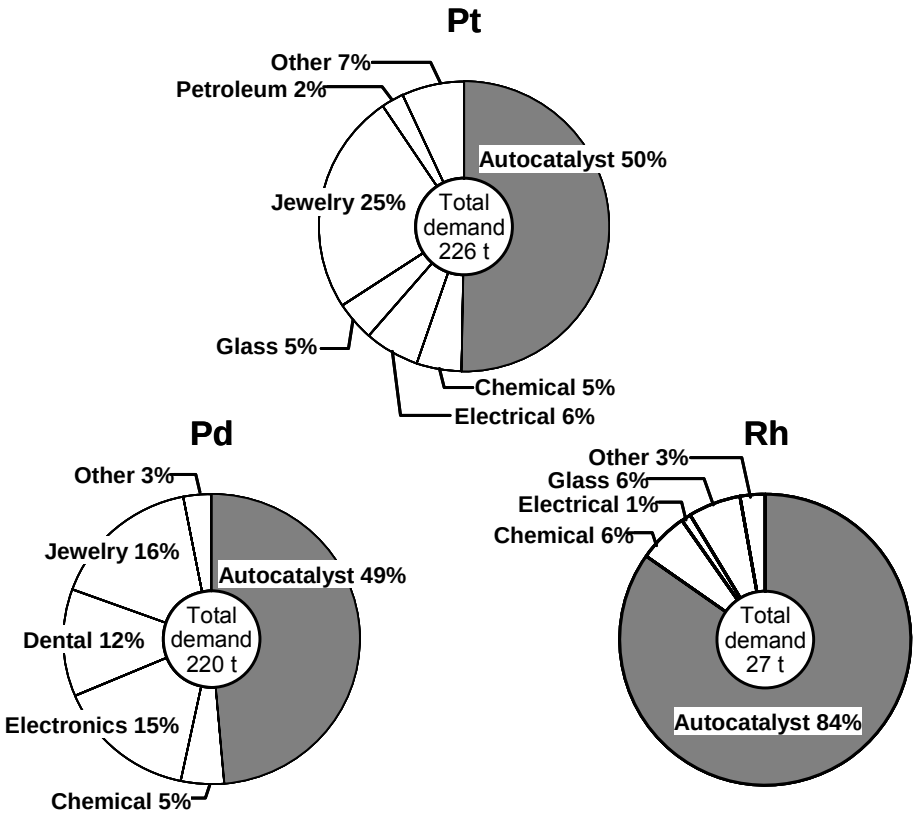

Figure 7. Demand of precious metals in 2006 [18]

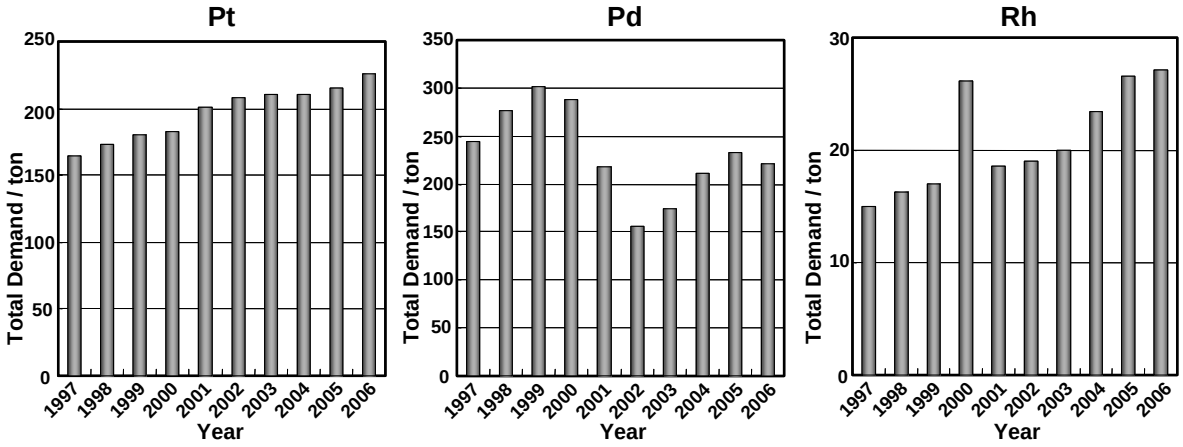

Figure 8. Change in demand of precious metals [18]

Scope and outline of this research

The goal of this thesis is to accelerate the speed of the development of high-performance catalysts for practical use by the physicochemical study. Recent progress of analysis techniques such as synchrotron radiation analysis has been achieving a remarkable breakthrough. These advanced analysis techniques gain a deeper appreciation on catalysts. A basic understanding of the structure of automotive catalysts at an atomic level can pave the way for planed catalytic design, which is based on scientific notion, rather than adopting a trial-and-error approach. In fact, a lot of trial-and-error efforts have been given on the synthesis of automotive catalysts. This physicochemical study will change the development process of the catalysts for practical use.

The brief of this thesis is summarized in Table 2. This thesis can be divided into two main branches from the view point of material. One is CeO_2-ZrO_2 mixed oxide as an OSC promoter used for TWCs, the other is Pt supported catalyst to purify the harmful emissions from diesel and gasoline powered vehicles. In Chapters 2 and 3, the relationship between the OSC performance of CeO_2-ZrO_2 mixed oxide and the atomic structure is mainly investigated. In Chapters 4, 5 and 6, on the basis of Pt-support interaction, the reaction selectivity, Pt sintering and Pt redispersion in Pt supported catalysts are studied. It is well known that for many metal-catalyzed reactions the support influences the chemical property of the metal particles. For example, it has been observed that the electronic structure op the supported Pt depend on the acid/base properties of the support. However, the nature of this interaction between metal and support is poorly understood. Therefore, another important purpose in these chapters is to systematically understand the nature of the Pt-support interaction. The details of each

chapter are described below.

Table 2. Brief of this thesis

	Catalyst	Application	Purpose
Chapter 2	Ceria-Zirconia	OSC promoter for TWC	Relationship between the OSC performance and its atomic structure
Chapter 3	Ceria-Zirconia	OSC promoter for TWC	Structural change along with the thermal degradation of the OSC performance
Chapter 4	Pt supported on Zirconia	Diesel catalyst	Reaction selectivity and Pt-support interaction
Chapter 5	Pt supported on Ceria-based oxide	TWC	Pt sintering inhibition and Pt-support interaction
Chapter 6	Pt supported on Ceria-based oxide	TWC	Pt redispersion and Pt-support interaction

The main purpose of Chapter 2 is to systematically clarify the relationship between the OSC and the structure of CeO_2-ZrO_2 at the atomic level. Three types of CeO_2-ZrO_2 compounds with the same composition (Ce/Zr = 1) are prepared by different methods, and exhibit different OSC efficiencies. The local structure around both Ce and Zr of these CeO_2-ZrO_2 samples will be investigated using the X-ray absorption fine structure (XAFS) and X-ray diffraction (XRD) methods in order to clarify the cation-cation (cation = Ce, Zr) network and the oxygen environment around the cation. This chapter elucidates that the OSC performance strongly depends on the subtle structural change. Moreover, the mechanism of the OSC improvement is postulated

from obtained results on the structure.

The previous chapter discovers that the homogeneous CeO_2-ZrO_2 solid solution has an ordered cation arrangement, and exhibits the highest OSC among a several types of CeO_2-ZrO_2 with the same composition (Ce/Zr = 1). The crystal structure of this CeO_2-ZrO_2 solid solution is usually termed as "κ-$CeZrO_4$ phase". However, it is clarified in Chapter 3 that the OSC performance of κ-$CeZrO_4$ degrades upon a high-temperature treatment under an oxidative atmosphere. It is presumed that this thermal degradation is resulted from the subtle structural change. In Chapter 3, by using XAFS and powder XRD, the author will try to investigate what exactly happened to its structure along with the thermal degradation of κ-$CeZrO_4$, and correlates with its OSC performance.

The key factor in improving the OSC and the mechanism of thermal degradation are elucidated in Chapter 2 and 3, respectively. Both high performance and high durability are essential function for practical use. The deep understanding based on scientific notion can eradicate trouble in the market and provide highly dependable vehicles.

In Chapter 4, the subject moves on to Pt supported on ZrO_2 as active sites for catalytic reaction. First, in this chapter, the reaction selectivity for diesel catalyst comes up for debate. As mentioned above, a highly selective oxidation catalyst, which has a higher oxidation activity for carbon, CO and HC compounds than that for SO_2, is required for diesel catalyst. The oxidation of *n*-hexane (gaseous HC) and SO_2 over two types of Pt/ZrO_2 catalysts with low and high ZrO_2 support surface areas is investigated. These Pt/ZrO_2 catalysts exhibit different selectivity for the oxidation of *n*-hexane and SO_2. The purpose of this chapter is to clarify the cause of this oxidation selectivity. This

chapter clarifies that the difference in the oxidation state of Pt sites as catalytic active sites causes the apparent selectivity to change. Moreover, the knowledge of Pt-support interaction obtained from this chapter plays an important part in an introduction of following chapters.

Chapter 5 describes a study of sintering inhibition mechanism of Pt supported on ceria-based oxide and Pt-oxide–support interaction. Sintering of the Pt metal particles during operation at high temperatures is considered to reduce the catalytic activity, that is, degrade the catalyst. The development of advanced catalysts without the sintering of Pt metal particles is required in automotive industrial research. In this chapter, two objects are investigated. First one is to understand the sintering inhibition mechanism of Pt particles on ceria-based oxide at the atomic level by using XAFS analysis. Secondly, the author will conduct further systematic investigation on various Pt catalysts, and clarifies the essence of the Pt-oxide-support interaction and its relation to Pt sintering in an oxidizing atmosphere.

Pt particles supported on ceria-based oxide does not sinter under oxidizing condition at 800 °C while Pt atoms on Al_2O_3 sinter significantly in the preceding chapter. However, even Pt/ceria-based oxide catalyst would sinter at higher temperature of 900 °C and above. In Chapter 6, Pt redispersion on ceria-based support is studied. A real-time observation of the redispersion behavior of sintered Pt on ceria-based oxide is made possible by a novel technique of in-situ time-resolved Turbo-XAS in fluorescence mode. This is the first observation of dynamic Pt redispersion and provides the potential for practical use. In addition, this chapter proposes the mechanism of Pt redispersion. Strong Pt-oxide-support interaction under oxidizing condition as has been pointed out in Chapter 5 is required to produce the redispersion of the aged catalyst.

The study in Chapters 5 and 6 aims at the development of highly durable catalysts without Pt sintering. Generally, a fresh catalyst is loaded with an excessive amount of precious metals, in expectation of the degradation of catalytic performance. If ultimate catalysts without deterioration are put into practice, superfluous amount of precious metal will be unnecessary. Therefore, these studies will accept an important part of effective use of these limited resources.

REFERENCES

[1] B.I. Bertelsen, *Platinum Metals Rev.* **45** (2001) 50.

[2] S. Matsumoto, *Toyota Tec. Rev.* **44** (1995) 10.

[3] J.C. Kummer, *Prog. Energy Combust. Sci.* **6** (1980) 177.

[4] H.C. Yao, Y.F. Yao, *J. Catal.* **86** (1984) 254.

[5] M. Ozawa, M. Kimura, A. Isogai, *J. Alloys Comp.* **193** (1993) 73.

[6] Y. Nagai, T. Yamamoto, T. Tanaka, S. Yoshida, T. Nonaka, T. Okamoto, A. Suda, M. Sugiura, *Catal. Today* **74** (2002) 225.

[7] P. J. F. Harris, *J. Catal.* **97** (1986) 527.

[8] R. M. J. Fiedorow, B. S. Chahar, S. E. Wanke, *J. Catal.* **51** (1978) 193.

[9] C. H. Bartholomew, *Appl. Catal. A* **212** (2001) 17.

[10] H. Birgersson, L. Eriksson, M. Boutonnet, S. G. Järås, *Appl. Catal. B* **54** (2004) 193.

[11] P.N. Hawker, *Platinum Met. Rev.* **39 (2)** (1995) 2.

[12] A. Fritz, V. Pitchon, *Appl. Catal. B* **13** (1997) 1.

[13] N. Miyoshi, S. Matsumoto, M. Ozawa, M. Kimura, *SAE Technical Paper* 891970 (1989).

[14] N. Takahashi, H. Shinjoh, T. Iijima, T. Suzuki, K. Yamazaki, K. Yokota, H. Suzuki, N. Miyoshi, S. Matsumoto, T. Tanizawa, T. Tanaka, S. Tateishi, K. Kasahara, *Catal. Today* **27** (1996) 63.

[15] S. Matsumoto, *Catal. Today* **29** (1996) 43.

[16] J. Suzuki, S. Matsumoto, *Topics in Catal.* **28** (2004) 171.

[17] R.J. Farrauto, K.E. Voss, *Appl. Catal. B* **10** (1996) 29.

[18] *Platinum 2006 Interim Review*, Johnson Matthy Public Ltd., UK (2006).

Chapter 2: XAFS and XRD analysis of CeO_2-ZrO_2 mixed oxides with the same composition ratio (Ce/Zr = 1)

ABSTRACT

Oxygen storage/release (OSC) capacity is an important feature common to all three-way catalysts that enables them to efficiently remove harmful compounds such as hydrocarbons, CO and NOx in automotive exhaust gases. In this report, three types of CeO_2-ZrO_2 (Ce:Zr = 1:1 molar ratio) compounds with different OSC were characterized by means of XRD (X-ray diffraction) and XAFS (X-ray absorption fine structure). The relationship between the compounds' OSC and molecular structure was investigated by quantitative EXAFS curve-fitting analysis. Enhancing the homogeneity of the Ce and Zr atoms in the CeO_2-ZrO_2 solid solution increased OSC performance, and greatly changed the local oxygen environment around Ce and Zr. The improvement in OSC was attributed to the increase in homogeneity of the CeO_2-ZrO_2 solid solution and to the change in the oxygen environment.

1. INTRODUCTION

The oxygen storage/release capacity (OSC) is one of the important functions required for automobile three-way catalysts (TWCs) in order to efficiently remove harmful compounds such as hydrocarbons, CO and NOx in automotive exhaust gases [1, 26]. In the TWCs, Ceria is widely used as a promoter due to its high OSC based on the reversible redox reaction ($CeO_2 \leftrightarrow CeO_{2-x} + (x/2)O_2$; x = 0 - 0.5). Ceria stores oxygen under oxygen excess conditions and releases it under oxygen deficient conditions in order to maintain the stoichiometric conditions. The highest catalytic performance is attained at stoichiometric conditions. However, the OSC performance of pure CeO_2 and the durability are still inadequate for practical use, and the improvement of the OSC of CeO_2 is required to develop highly efficient TWCs. Over 10 years ago, our laboratory discovered that the addition of ZrO_2 to CeO_2 would enhance the OSC as well as improve its thermal stability [2-4]. Thereafter, CeO_2-ZrO_2 has been widely utilized for commercial catalysts, and the research on CeO_2-ZrO_2 has been receiving increasing attention. A considerable number of studies have been conducted on the physical properties and structure of CeO_2-ZrO_2 by many groups, and significant progress in knowledge has been made [*e.g.* 5-11]. However, the key factor in improving the OSC by the addition of ZrO_2 to CeO_2 remains unclear. The main purpose of this study is to systematically clarify the relationship between the OSC and the structure of CeO_2-ZrO_2 at the atomic level. Three types of CeO_2-ZrO_2 compounds with the same composition (Ce/Zr = 1) were prepared by different methods, and exhibited different OSC efficiencies. We investigated the local structure around both Ce and Zr of these CeO_2-ZrO_2 samples using the X-ray absorption fine structure (XAFS) method in order to clarify the cation-cation (cation = Ce, Zr) network and the oxygen environment

around the cation.

Although several groups have reported the XAFS analysis of CeO_2-ZrO_2, all of them have utilized Ce L_3-edge (5.7 keV) XAFS [6, 24] while there have been no studies employing Ce K-edge (40.5 keV) XAFS. The usable data region of Ce L_3-edge EXAFS is limited to ca. 3 - 9 $Å^{-1}$ in electron wavenumber (k) due to the presence of the Ce L_2-edge (6.2 keV). Since Ce and Zr contributions to the EXAFS signals are remarkable in the high-k part [14], the XAFS measurement of the Ce K-edge with a wide k-range is required to obtain precise information on the Ce-Ce and Ce-Zr bonding, and to clarify the cation-cation network. As a result, conventional characterizations leave controversy about the homogeneity at the atomic level for Ce and Zr atoms in the CeO_2-ZrO_2 solid solution [6, 22, 23]. The high-energy X-ray at the SPring-8 synchrotron radiation facilities (Hyogo, Japan) makes it possible to record the XAFS spectra with an excellent signal-to-noise ratio at the K-edges of heavy elements, and to obtain precise information on the Ce-cation bonding [12, 13, 15]. In addition to the foregoing main purpose of clarifying the relationship between the OSC and the atomic structure, another important purpose of this study is to precisely estimate the homogeneity of the CeO_2-ZrO_2 solid solution by both Ce K-edge and Zr K-edge XAFS.

2. EXPERIMENTAL

2.1. Preparation

Three types of CeO_2-ZrO_2 compounds with the same composition (Ce/Zr = 1; CZ55-1, CZ55-2 and CZ55-3) were prepared by the following methods. CZ55-1 was prepared by precipitation with aqueous NH_3 using CeO_2 powder (Anan Kasei, 99.9 %, 120 m^2/g) and $ZrO(NO_3)_2$ aqueous solution. The precipitate was dried at 363 K and calcined in air at 773 K for 3 h. CZ55-2 was prepared by coprecipitation with aqueous NH_3 using $Ce(NO_3)_3$ and $ZrO(NO_3)_2$ aqueous solutions. The precipitate was dried at 363 K and calcined in air at 773 K for 3 h. CZ55-3 was synthesized by the same coprecipitation process as CZ55-2, except that the dried powder was reduced at 1473 K for 4 h in flowing pure CO and further oxidized in air at 773 K for 3 h. All the samples were finally calcined in air at 773 K. Oxygen was fully stored in the Ce compounds by this treatment.

2.2. Characterization

2.2.1. Oxygen storage/release capacity (OSC) measurements

The OSC was estimated by a thermo-gravimetric analysis [11]. The 1 wt.% platinum-loaded CeO_2-ZrO_2 samples were cyclically reduced by 20 % H_2 (N_2 balance) for 5 min then oxidized by 50 % O_2 (N_2 balance) for 5 min at 773 K. The weight loss and gain were measured using a thermo-gravimetric analyzer (TGA-50, Shimadzu). The reductive/oxidative conditions were maintained until the weight became constant. The value of the weight change between the reductive and oxidative conditions corresponds to the total OSC at 773 K.

2.2.2. Surface area measurements

The specific surface areas of the samples were estimated using the N_2 adsorption isotherm at 77 K by the one-point Brunauer-Emmett-Teller (BET) method using an automatic surface analyzer (Micro Sorp 4232II, Micro Data). The samples were degassed in flowing N_2 at 473 K for 20 min.

2.2.3. X-Ray diffraction (XRD)

The powder XRD experiments were carried out using a RINT2000 (Rigaku) diffractometer with Cu-K_α radiation (1.5406 Å). The identification of the phase was made with the help of the JCPDS cards (Joint Committee on Powder Diffraction Standards).

2.2.4. X-ray absorption fine structure (XAFS)

The Ce K-edge (40.45 keV) and Zr K-edge (18.00 keV) XAFS spectra were measured at BL01B1 and BL16B2 of SPring-8 (Hyogo, Japan). The storage ring energy was operated at 8 GeV with a typical current of 100 mA. The measurements were carried out using a Si (3 1 1) double crystal monochromator in the transmission mode at room temperature. Data reduction of the XAFS was carried out as described elsewhere [16]. The quantitative curve-fitting analysis of the EXAFS spectra was performed for the inverse Fourier transforms on the cation-cation (cation = Ce, Zr) and cation-oxygen shells. Empirical parameters in the analysis were obtained from standard compounds, e.g., cubic CeO_2 for Ce-Ce and Ce-O bonding, 8 mol% Y-doped cubic ZrO_2 for Zr-Zr and Zr-O bonding, and cubic $Ce_{0.9}Zr_{0.1}O_2$ for Zr-Ce bonding. The parameter for the Ce-Zr bonding was calculated from the extracted Ce-Ce, Zr-Zr and Zr-Ce parameters.

3. RESULTS AND DISCUSSION

3.1. Oxygen storage/release capacity (OSC) and BET surface area

Table 1 shows the OSC properties and BET surface area of the samples. The Ce efficiency means the ratio of $Ce^{3+}/(Ce^{3+} + Ce^{4+})$ under reductive conditions. The Zr oxidation state in the CeO_2-ZrO_2 remains at Zr^{4+} under both the reductive and oxidative conditions at 773 K [17]. Thus, only the Ce atoms contribute to the OSC through the Ce^{3+}/Ce^{4+} redox couple. The OSC value increases in the order of CZ55-1 < CZ55-2 < CZ55-3. CZ55-3 exhibited the highest OSC, and its Ce efficiency was 88.6 %. It is noteworthy that almost all of the Ce in the CZ55-3 contributes to the OSC. Also, several groups showed that a high temperature reductive treatment followed by a mild oxidation strongly modifies the oxygen release behavior of the CeO_2-ZrO_2 mixed oxide [5, 27].

Table 1. OSC property and BET surface area of CeO_2-ZrO_2 mixed oxides.

Sample [a]	OSC [b] (μmol-O/g)	Ce efficiency [c] (%)	BET surface area (m^2/g)
CZ55-1	160	9.6	125
CZ55-2	880	51.7	89
CZ55-3	1500	88.6	1

[a] For sample description, see Section 2.
[b] OSC (Oxygen Storage/Release Capacity) of 1 wt.% Pt-loaded Ce compounds was measured at 773 K.
[c] The ratio $Ce^{3+}/(Ce^{3+} + Ce^{4+})$ under reductive condition.

The BET surface areas ranged from 1 to 125 m^2/g (Table 1). The BET surface areas depend on the preparation methods. Especially, the BET surface area of CZ55-3 is very low due to its high-temperature treatment during its synthesis, indicating that the OSC is not related to the surface area. The number of surface oxygen atoms can be estimated to be ca. 3 μmol-O/m^2 for CeO_2-ZrO_2 (Ce:Zr = 1:1 molar ratio) [18]. The experimental OSC values per m^2 of the samples were 1.3, 9.9 and 1500 μmol-O/m^2 for CZ55-1, CZ55-2 and CZ55-3, respectively. Therefore, the oxygen storage/release of CZ55-1 is limited to the surface at 773 K. In the case of CZ55-2, the oxygen storage/release progresses from the surface to ca. 3 layers. For CZ55-3, almost all the bulk oxygen atoms contribute to the OSC.

3.2. XRD

Figure 1 shows the XRD patterns of the samples. The phase identification of the samples is summarized in Table 2. Broad XRD peaks were observed for CZ55-1 and CZ55-2, while sharp peaks for CZ55-3. CZ55-1 was shown to be a mixture of cubic CeO_2 (lattice parameter: a = 5.41 Å) and tetragonal ZrO_2 (lattice parameter: a = 3.58 Å, c = 5.21 Å), although CZ55-2 and CZ55-3 have a cubic structure (lattice parameter: CZ55-2, a = 5.29 Å; and CZ55-3, a = 5.26 Å). The lattice constants of the cubic phase for the samples decrease in the order of CZ55-1, CZ55-2 and CZ55-3. This means that the unit cell of the cubic phase shrinks in this order.

In CZ55-3, we could observe small peaks indicated with an asterisk, except for the principal peaks which are attributed to the cubic CeO_2-ZrO_2. These small peaks are due to the ordered arrangement of the cations [9]. It is well known that a pyrochlore-type $Ce_2Zr_2O_7$ forms by the high temperature reduction of CeO_2-ZrO_2, which possesses the

ordered arrangement of Ce and Zr ions [5]. The κ-$CeZrO_4$ phase is prepared by mild-oxidation of the pyrochlore-type precursor, which maintains the ordered arrangement [5]. The XRD patterns of CZ55-3 almost correspond to that of κ-$CeZrO_4$. Therefore, it is suggested that CZ55-3 is cubic CeO_2-ZrO_2 with an ordered arrangement of the cations.

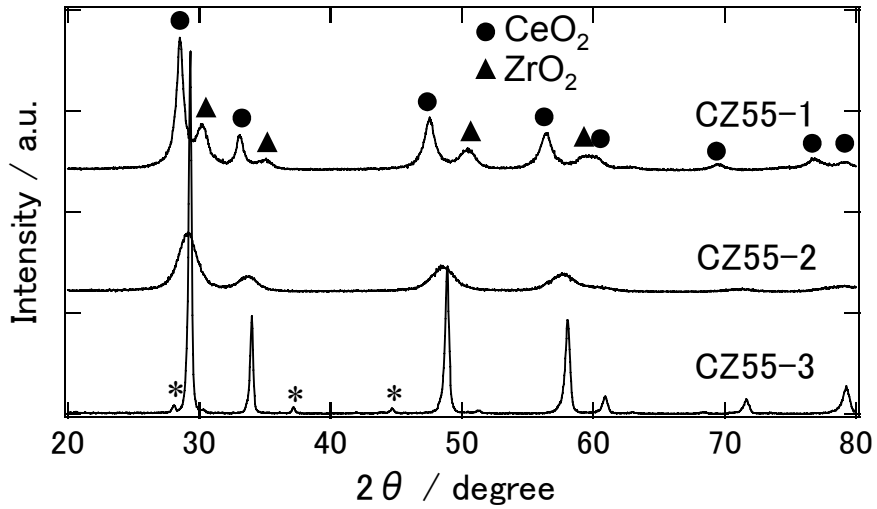

Figure 1. XRD patterns of CeO_2-ZrO_2 samples with the same composition ratio (Ce/Zr = 1). Small peaks indicated with asterisks are characteristic of κ-$CeZrO_4$ due to the ordered arrangement of the cations, see [5].

Table 2. Phases identified and lattice parameters determined by XRD.

Sample	Phase	Lattice parameters (Å)
CeO_2 [a]	Cubic	a = 5.41
CZ55-1	Cubic (CeO_2)	a = 5.41
	Tetragonal (ZrO_2)	a = 3.58 c = 5.21
CZ55-2	Cubic	a = 5.29
CZ55-3	Cubic	a = 5.26

[a] Standard compound. The data refer to JCPDS cards No. 34-0394.

3.3. XAFS

3.3.1. Fourier transforms (FTs) of Ce K-edge and Zr K-edge EXAFS spectra

Figures 2 and 3 show Ce and Zr K-edges EXAFS spectra of the samples, respectively. The spectra with a good signal-to-noise ratio at both of Ce and Zr K-edges were obtained in the wide region of 3.0 - 17.0 $Å^{-1}$. At the high-k part 9.0 - 17.0 $Å^{-1}$ of Ce K-edge, we could observe the apparent EXAFS signals caused mainly by Ce and/or Zr. Ce K-edge EXAFS signals of CZ55-1, CZ55-2 and CZ55-3 are obviously different from each other. On the other hand, the spectrum of CZ55-1 is very similar to that of CeO_2 in points of frequencies and amplitudes. Also the Zr K-edge EXAFS spectra of the CeO_2-ZrO_2 samples have different features respectively.

FTs were performed on the Ce and Zr K-edges EXAFS spectra in about the 3.0 - 17 $Å^{-1}$ region. The FTs of the Ce K-edge EXAFS spectra are presented in Figure 4 (a). The first peak at 1.8 Å and the second peak at 3.5 Å correspond to the Ce-O and

Ce-cation (cation = Ce, Zr) bonds, respectively. The position and amplitude of the Ce-O peaks for CZ55-1, CZ55-2 and CZ55-3 are slightly different from each other. CZ55-2 and CZ55-3 exhibit lower Ce-cation peak intensities than that of CZ55-1. Additionally, the Ce-cation peak of CZ55-3 appears to have split in two. These clear differences among the Ce-cation peaks could not be observed for the Ce L_3-edge (Figure 4 (b)). Especially, the Ce-cation peaks of CZ55-2 and CZ55-3 in the Ce L_3-edge almost disappear due to the lack of an EXAFS signal for heavy elements in the high-k part. Therefore, the measurements of the Ce K-edge XAFS spectrum are necessary to obtain precise information about the Ce-cation bonding. Figure 5 shows the FTs of the Zr K-edge EXAFS spectra. The first peak at 1.7 Å was assigned to Zr-O bonds and the second peak at 3.5 Å to Zr-cation bonds. The shape of the FTs for CZ55-1, CZ55-2 and CZ55-3 are obviously different. According to the results mentioned above, it is thus suggested that the OSC exhibits a significant correlation with the local structure around Ce and Zr.

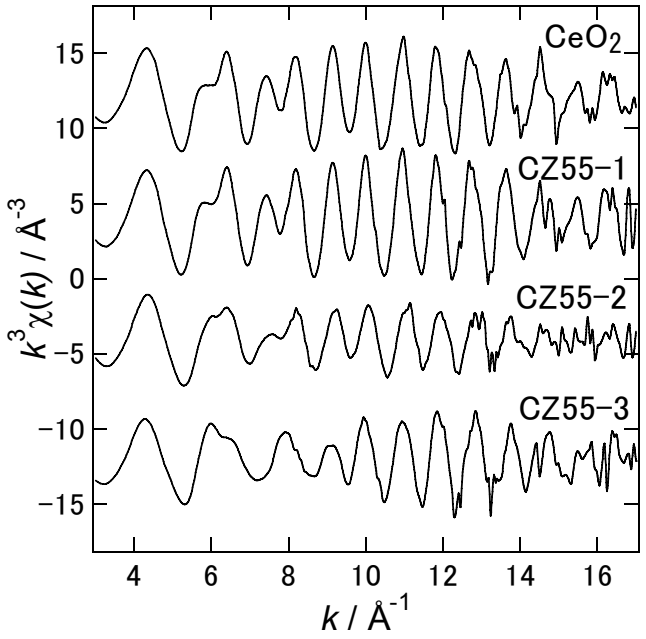

Figure 2. The k^3-weighted Ce K-edge EXAFS spectra.

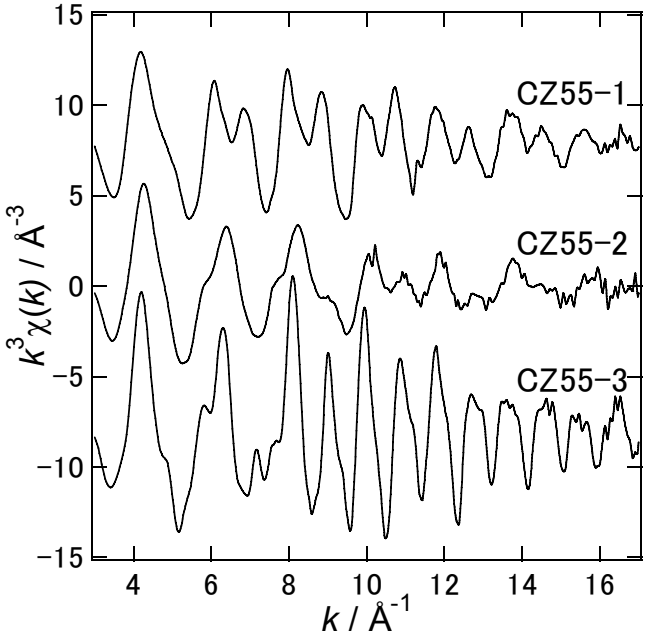

Figure 3. The k^3-weighted Zr K-edge EXAFS spectra.

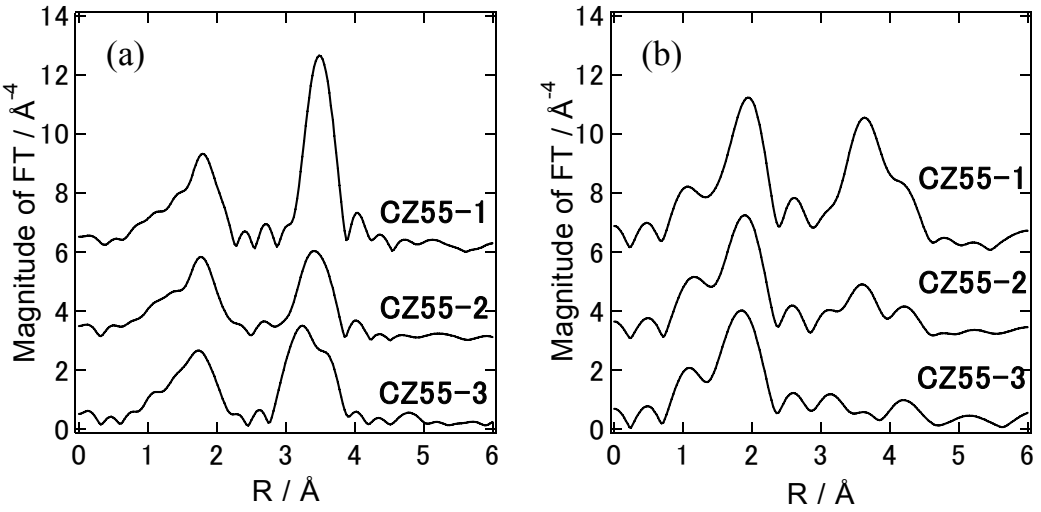

Figure 4. Fourier-transformed k^3x data of (a) Ce K-edge and (b) Ce L_3-edge EXAFS of CeO_2-ZrO_2 samples.

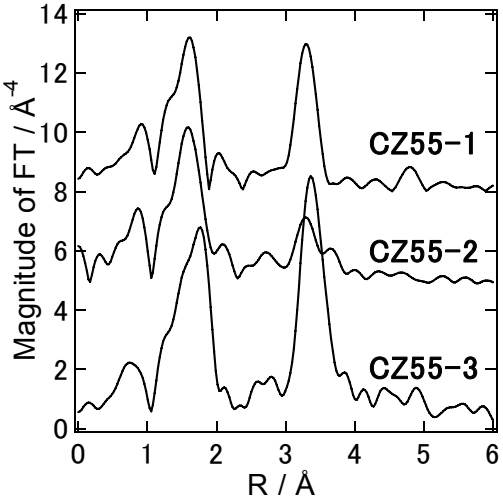

Figure 5. Fourier-transformed k^3x data of Zr K-edge EXAFS of CeO_2-ZrO_2 samples.

3.3.2. Zr K-edge XANES spectra

The XANES spectra at the Zr K-edge are shown in Figure 6. A comparison of the spectra indicated by *A* or *B* was carefully made. To begin with, peak *A*, a weak shoulder on the steeply rising absorption edge, is more apparent in CZ55-1 and CZ55-2 than in CZ55-3. This pre-edge absorption can be assigned to the 1s → 4d which is sensitive to the cation-O geometry. This transition is stronger in compounds that are distorted from centrosymmetry, and significantly appear for pure tetragonal ZrO_2 [19]. In fact, the feature of the XANES spectrum of CZ55-1 is very similar to that of pure tetragonal ZrO_2 [19]. Furthermore, tetragonal ZrO_2 was identified by the XRD result described above. CZ55-2 also possesses a tetragonal environment of the Zr-O coordination. On the other hand, it is postulated that CZ55-3 possesses a higher centrosymmetry of Zr-O coordination than those of CZ55-1 and CZ55-2. The feature of the XANES spectrum of CZ55-3 is very similar to that of cubic ZrO_2 [19]. Next, peak *B* in CZ55-1 shows a single broad peak, whereas that in CZ55-2 shows a slight splitting, and in CZ55-3, a clear splitting. A similar splitting has been reported for the Y_2O_3-ZrO_2 solid solution by Li et al. [20]. Li et al. reported that the splitting becomes progressively more pronounced as the Y_2O_3 concentration increases from 3 mol% Y_2O_3-ZrO_2 (tetragonal) to 20 mol% Y_2O_3-ZrO_2 (cubic). They also observed that peak *A* decreases with the increasing Y_2O_3 concentration. Therefore, the results derived from the XANES spectra in our system indicate that the concentration of Ce insertion into ZrO_2 increases along the series: CZ55-1, CZ55-2 and CZ55-3. Additionally, as more CeO_2 is inserted into the ZrO_2 lattice, the CeO_2- ZrO_2 is expected to form a more cubic structure.

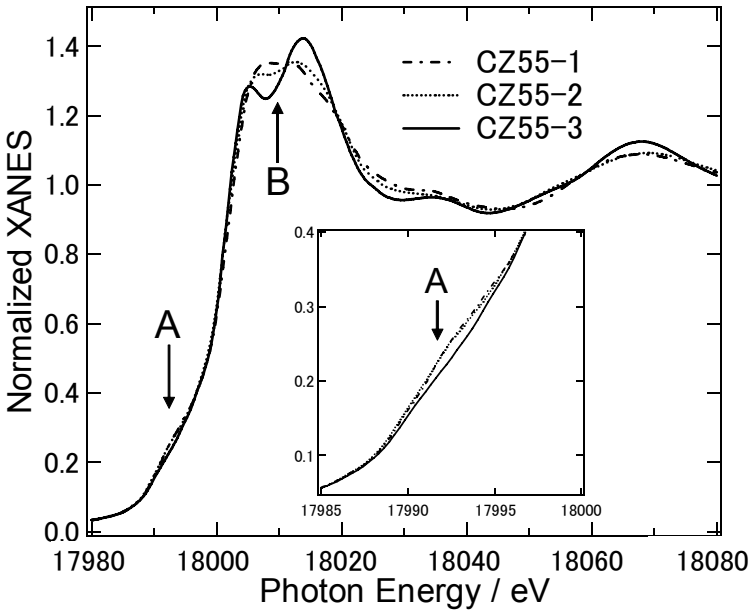

Figure 6. Zr K-edge XANES spectra of CeO_2-ZrO_2 samples.

3.3.3. Cation-cation network

A quantitative curve-fitting analysis was performed for the cation-cation shells in the FTs to clarify this network. For example, Figure 7 shows the fit of inverse Fts of the cation-cation shells for CZ55-3. The curve-fitting results of the Ce and Zr K-edges EXAFS are summarized in Tables 3 and 4, respectively. Figure 8 shows a model illustration of the cation-cation network for the CeO_2-ZrO_2 samples, which is proposed from the curve-fitting analysis. First, the Ce-cation shell for CZ55-1 was fitted with a single Ce-Ce bond, and the Zr-cation shell was also fitted with a single Zr-Zr bond. The distance (R = 3.82 Å) and coordination number (CN = 11.9) of the Ce-Ce bond is consistent with the values for CeO_2. Thus CZ55-1 is a mixture of pure CeO_2 and ZrO_2 (Figure 8 (a)). The CN of the Zr-Zr bond for CZ55-1 (6.6) is lower than 12. It could be considered that the size of the formed ZrO_2 crystallite was small. The average particle

size was estimated from the XRD peak using the Scherrer equation. The particle sizes of CeO_2 and ZrO_2 in CZ55-1 were about 130 and 80 Å, respectively. This result supports the decrease in the CN of the Zr-Zr bond for CZ55-1. Secondly, for CZ55-2, not only Ce-Ce (Zr-Zr), but also Ce-Zr (Zr-Ce) bonds were required to obtain an appropriate fit for the cation-cation shell at the Ce (Zr) K-edge. The Ce-cation shell was fitted with Ce-Ce (CN = 8.0) and Ce- Zr (CN = 3.6) bonds. The CN of the Ce-Ce bond is larger than that of the Ce-Zr bond. The CN of the Ce-Zr bond (3.6) is close to that of the Zr-Ce bond (4.0). This indicates that a CeO_2-ZrO_2 solid solution in CZ55-2 forms, but a Ce rich domain and Zr rich one still remain (Figure 8 (b)). As for the Zr-Zr bond of CZ55-2, we could not obtain the appropriate fit. The relative Debye-Waller factor ($\Delta\sigma^2$) is too large. This may mean that the distribution of the Zr-Zr bond distances is broad due to the presence of some structural disorder. Finally, the Ce-cation shell for CZ55-3 was fitted with Ce-Ce (CN = 6.0) and Ce-Zr (CN = 6.0) bonds. The Zr-cation shell was also fitted with Zr-Zr (CN = 6.0) and Zr-Ce (CN = 6.0) bonds. The CN ratios of Ce-Ce to Ce-Zr and Zr-Zr to Zr-Ce are just 1. These CN ratios are equal to the Ce/Zr composition ratio of the sample. It is clear that the $Ce_{0.5}Zr_{0.5}O_2$ solid solution in CZ55-3 homogeneously forms at an atomic level. Furthermore, as we mentioned in the XRD section, CZ55-3 possesses an ordered arrangement of Ce and Zr ions (Figure 8 (c)). The homogeneity of the CeO_2-ZrO_2 solid solution increases in the order of CZ55-1, CZ55-2 and CZ55-3. This is in agreement with the suggestion derived from the result of the Zr K-edge XANES. These results lead to the conclusion that the OSC increases by enhancing the homogeneity of the Ce and Zr atoms in the CeO_2-ZrO_2 solid solution.

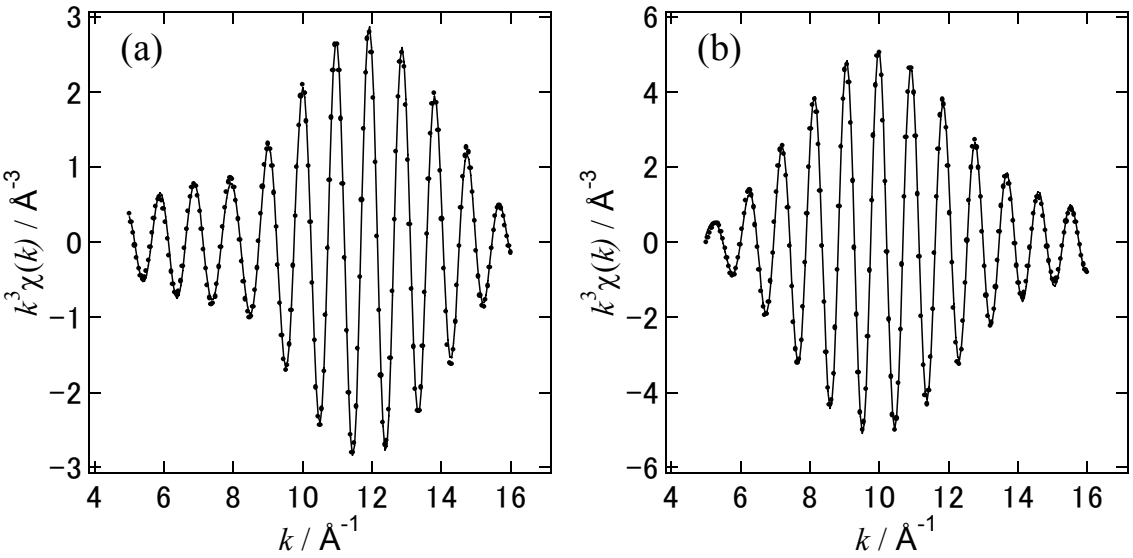

Figure 7. Inverse Fourier-transforms of (a) Ce-cation and (b) Zr-cation shells for CZ55-3 and the corresponding curve-fit. Experimental (—) and curve-fit (•).

Table 3. Results of curve-fitting analysis for Ce-cation shells [a].

Sample	Bond	CN	R (Å)	$\Delta\sigma^2$ (Å^2) [b]
Cubic ZrO_2 [c]	Zr-Zr	12	3.628	
CZ55-1	Zr-Zr	6.6(2)	3.66(0)	0.0061(1)
CZ55-2	Zr-Zr	3.0(6)	3.69(0)	0.0124(19)
	Zr-Ce	4.0(3)	3.76(0)	0.0030(3)
CZ55-3	Zr-Zr	6.0(4)	3.62(0)	0.0086(6)
	Zr-Ce	6.0(3)	3.75(0)	-0.0010(1)

[a] The standard deviation is given in parentheses.
[b] Relative Debye-Waller factor
[c] Standard compound

Table 4. Results of curve-fitting analysis for Zr-cation shells [a].

Sample	Bond	CN	R (Å)	$\Delta\sigma^2$ (Å^2) [b]
Cubic CeO_2 [c]	Ce-Ce	12	3.826	
CZ55-1	Ce-Ce	11.9(2)	3.82(0)	0.0026(1)
CZ55-2	Ce-Ce	8.0(4)	3.78(0)	0.0034(2)
	Ce-Zr	3.6(5)	3.71(0)	0.0063(13)
CZ55-3	Ce-Ce	6.0(3)	3.78(0)	0.0016(2)
	Ce-Zr	6.0(3)	3.72(0)	0.0022(3)

[a] The standard deviation is given in parentheses.

[b] Relative Debye-Waller factor

[c] 8 mol% Y-doped cubic ZrO_2 as standard compound

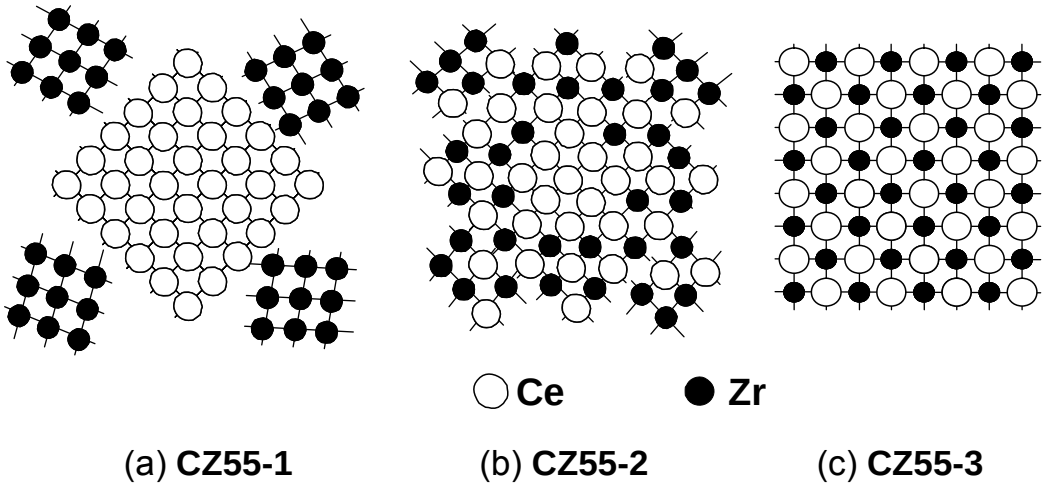

Figure 8. Model illustration of cation-cation network for the CeO_2-ZrO_2 samples with the same composition (Ce/Zr = 1). CZ55-1 consists of pure CeO_2 and ZrO_2. A CeO_2-ZrO_2 solid solution forms in CZ55-2, but the Ce rich domain and Zr rich one still remain. The $Ce_{0.5}Zr_{0.5}O_2$ solid solution in CZ55-3 homogeneously forms at an atomic level, and possesses the ordered arrangement of Ce and Zr ions.

3.3.4. Oxygen environment around cation

We will now discuss the cation-oxygen shells of these samples. Tables 5 and 6 present the curve-fitting results for the Ce-oxygen and Zr-oxygen shells, respectively. First, the CN of Ce-O for all samples was eight. The Ce-O bond length (R = 2.33 Å) of CZ55-1 is almost consistent with that of CeO_2 as a standard compound. In contrast, the Ce-O bond length gradually shortens in the order of CZ55-1, CZ55-2 and CZ55-3. Since the CeO_2-ZrO_2 solid solution in CZ55-2 is nonhomogeneous, its Ce-O bond length is the average value of all the Ce-O bonds. A model illustration of the oxygen environment around Ce is proposed in Figure 9. This phenomenon of the gradual compression of the Ce-O bonding is interpreted as follows. Since the ionic radius of Zr^{4+} (0.84 Å) for an 8-fold coordination is smaller than that of Ce^{4+} (0.97 Å) [21], the unit cell of the cubic CeO_2-ZrO_2 solid solution decreases with the increasing undersized Zr^{4+} concentration inserted into the Ce network, causing the Ce-O bond length to shorten. The decreasing of the lattice constant for the CeO_2-ZrO_2 samples result supports this result for the compression of the Ce-O bonding.

Secondly, the Zr-O bond for CZ55-1 was fitted with two sets of short and long Zr-O bond lengths. Its bond length and the CN of Zr-O are close to the values for typical tetragonal ZrO_2 [19]. The Zr-O bond for CZ55-2 also consisted of two sets of Zr-O bond lengths. However, the CN of the Zr-O bond for CZ55-2 (6 + 2) is different from that (4 + 4) for a typical tetragonal ZrO_2. In contrast, the Zr-O bond for CZ55-3 was fitted with a single Zr-O bond. The model illustration of the oxygen environment around Zr is proposed in Figure 10. This phenomenon is interpreted as follows. In CZ55-1, a pure tetragonal ZrO_2 forms and has two sets (4 + 4) of short and long Zr-O

bond lengths. For CZ55-2, the symmetry of the Zr-O coordination is, on average, somewhat more centrosymmetric than that of the tetragonal ZrO_2 due to the introduction of some Zr ions into the cubic CeO_2 framework. Because of the nonhomogeneous CeO_2-ZrO_2 solid solution in CZ55-2, Figure 10 (b) indicates the average structure of the oxygen environment around all the Zr atoms, and its average structure is an intermediate state between CZ55-1 and CZ55-3. For CZ55-3, a cubic $Ce_{0.5}Zr_{0.5}O_2$ solid solution homogeneously forms at the atomic level. Hence, the configuration of the oxygen around Zr for CZ55-3 has a good symmetric 8-fold coordination. These results are in accord with the Zr K-edge XANES observations that CZ55-3 possesses a higher centrosymmetry of Zr-O coordination than those of CZ55-1 and CZ55-2.

Table 5. Results of curve-fitting analysis for Ce-oxygen shells [a].

Sample	Bond	CN	*R* (Å)	$\Delta\sigma^2$ [b] (Å^2)
Cubic CeO_2[c]	Ce-O	8	2.343	
CZ55-1	Ce-O	8.0(1)	2.33(0)	0.0035(1)
CZ55-2	Ce-O	8.0(1)	2.30(0)	0.0052(3)
CZ55-3	Ce-O	8.0(2)	2.27(0)	0.0044(2)

[a] The standard deviation is given in parentheses.

[b] Relative Debye-Waller factor

[c] Standard compound

Table 6. Results of curve-fitting analysis for Zr-oxygen shells [a]

Sample	Bond	CN	R (Å)	$\Delta\sigma^2$ [b] (Å^2)
Cubic ZrO_2[c]	Zr-O	8	2.222	
CZ55-1	Zr-O Zr-O	4.0(5) 4.0(6)	2.17(0) 2.36(0)	-0.0081(5) 0.0067(28)
CZ55-2	Zr-O Zr-O	6.0(5) 2.0(5)	2.19(0) 2.37(3)	-0.0059(4) -0.0017(11)
CZ55-3	Zr-O	8.0(2)	2.27(0)	-0.0046(2)

[a] The standard deviation is given in parentheses.

[b] Relative Debye-Waller factor

[c] 8 mol% Y-doped cubic ZrO_2 as standard compound

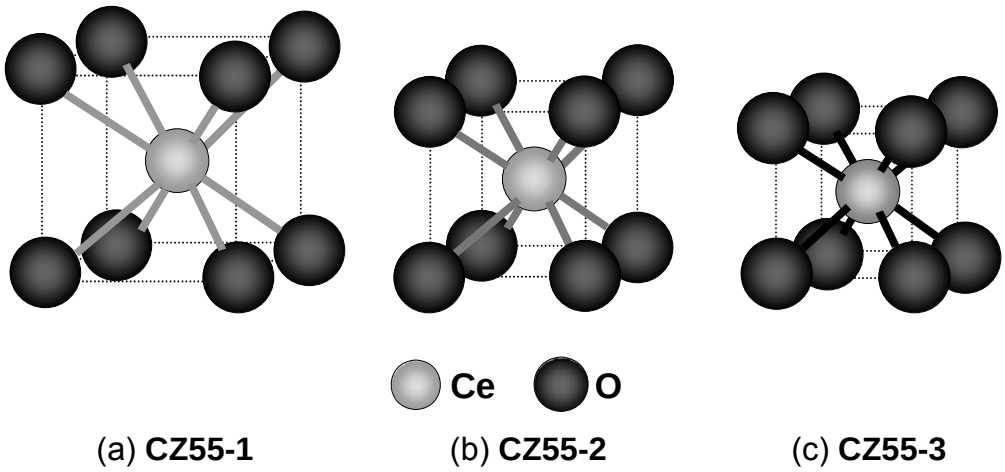

Figure 9. Model illustration of oxygen environment around Ce. The Ce-O bond length gradually shortens in the order of CZ55-1, CZ55-2 and CZ55-3.

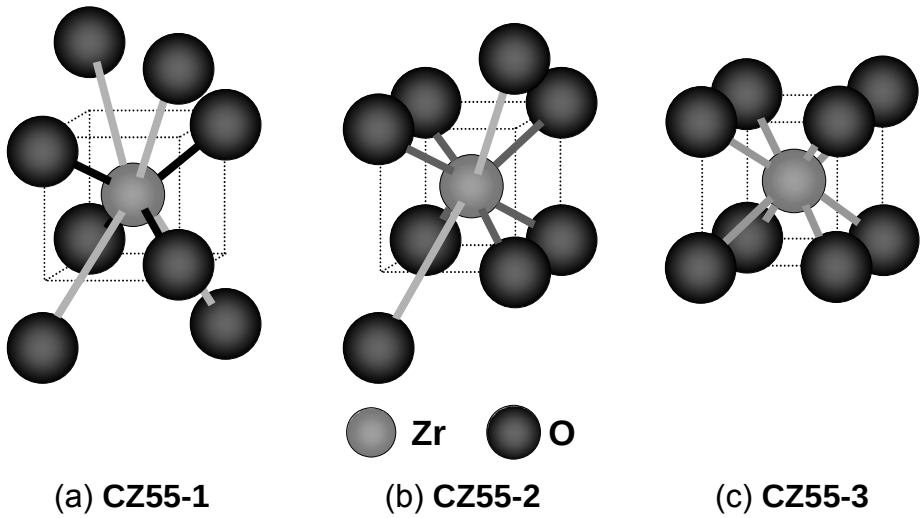

Figure 10. Model illustration of oxygen environment around Zr. In CZ55-1, a pure tetragonal ZrO_2 forms and has two sets of short and long Zr-O bond lengths. For CZ55-2, the symmetry of Zr-O coordination is, on average, somewhat more centrosymmetric than that of tetragonal ZrO_2. The configuration of the oxygen around Zr for CZ55-3 has a good symmetric 8-fold coordination.

3.4. Mechanism of the OSC improvement

Here, we discuss the mechanism of the OSC improvement from the points of the homogeneity and the oxygen environment. First, the effective ionic radii of Ce^{4+}, Ce^{3+} and Zr^{4+} are 0.97, 1.14 and 0.84 Å, respectively [21]. During the oxygen release process, the volume of the Ce compound increases in proportion to the change of the Ce oxidation state from Ce^{4+} to Ce^{3+}. The stress energy arising from this volume increment would restrict any further valence change of the Ce. The introduction of downsized Zr ions into the Ce framework could compensate for the volume increment, and ease the valence change ($Ce^{4+} \rightarrow Ce^{3+}$). In fact, a computer simulation study by Balducci et al. indicates that the Ce^{4+}/Ce^{3+} bulk reduction energy in model cubic CeO_2-ZrO_2 solid solutions was significantly reduced even with small amounts of ZrO_2 [25]. This point would be the main reason why the enhancement of the homogeneity of Ce and Zr atoms in the CeO_2-ZrO_2 solid solution improves the OSC performance. Secondly, by the atomically homogeneous introduction of Zr ions into the cubic CeO_2 framework, the Ce-O bond length shortens, and the configuration of the oxygen around Zr has a more centrosymmetric coordination. In particular, CZ55-3 has a good symmetric 8-fold coordination around the Zr. This symmetric 8-fold coordination state around Zr is generally considered to be spatially tight and unstable, because the ionic radius of Zr^{4+} (0.84 Å) is much smaller than that of O^{2-} (1.38 Å) [21]. On the other hand, the oxygen environment around Ce for CZ55-3 is also considered to be tight, because the Ce-O bond length for CZ55-3 is much shorter than that for the stable pure CeO_2. Actually, CZ55-3, the κ-$CeZrO_4$ solid solution, is not a stable phase but a metastable one in an oxidative atmosphere [5]. At 1273 K or less, CZ55-3 maintains its structure. However, if the temperature goes over 1473 K, a phase separation occurs in the oxidative

atmosphere, and part of the CZ55-3 is divided into stable CeO_2 and ZrO_2. We confirmed these phenomena by XRD. This instability of the oxygen environment around Ce and Zr will generate some active oxygens which are responsible for the improved OSC. However, our suggestion about the Zr-O local structure for the improved OSC differs from previous results. For example, Vlaic et al. [6] reported the following: "by introducing Zr ions into the CeO_2 lattice, the oxygen sublattice becomes significantly distorted. Zr-O coordination of the type 4 + 2 (short and long Zr-O) is found due to a displacement of two oxygens to a nonbonding distance. This distortion of the oxygen sublattice generates some mobile oxygens." On the other hand, Lemaux et al. [10] reported the following: "a lamellar-type structural model explains the high OSC of $Ce_{0.5}Zr_{0.5}O_2$, the short Zr-O_I (CN = 4) corresponds to the *intra* layer Zr-O bond and the much weaker and long Zr-O_{II} (CN = 4) to the *inter* layer Zr-O interaction. The OSC is determined by the *inter*layer Zr-O interaction." In both cases, they insist that the distortion of the short and long Zr-O coordination enhances the OSC. In contrast, we suggest that the instability of the symmetric 8-fold coordination around Zr, as shown in CZ55-3, will generate some active oxygens. Vlaic and Lemaux et al. investigated the local structure of the CeO_2-ZrO_2 solid solution prepared by a high temperature firing or a precipitation process, not by a high temperature reduction. A high temperature reductive treatment followed by a mild oxidation causes the ordered arrangement of the cations, and that treatment could construct a specific oxygen environment around the cations. However, at present, we have no definite explanation for these different opinions. Further work is required to estimate the general validity.

4. CONCLUDING REMARKS

The present study clearly showed the relationship between the OSC and local structure around Ce and Zr in three types of CeO_2-ZrO_2 mixed oxides (Ce:Zr = 1:1 molar ratio). In conclusion, the OSC increases by enhancing the homogeneity of the Ce and Zr atoms in the CeO_2-ZrO_2 solid solution. Especially, an atomically homogeneous $Ce_{0.5}Zr_{0.5}O_2$ solid solution exhibited the highest OSC among these CeO_2-ZrO_2 samples. The enhancement of the homogeneity of the Ce and Zr atoms could ease the valence change of the Ce ($Ce^{4+} \rightarrow Ce^{3+}$). By the atomically homogeneous introduction of Zr ions into the cubic CeO_2 framework, the Ce-O bond length in the CeO_2-ZrO_2 shortens, and the configuration of the oxygen around Zr has a more centrosymmetric 8-fold coordination. This modification of the local oxygen environment around Ce and Zr will generate some active oxygens for the OSC improvement. We postulated that the enhancement of the homogeneity of the CeO_2-ZrO_2 solid solution and the modification of the oxygen environment would be the source for the OSC improvement. Additionally, we could clarify the cation-cation network by using the high-energy X-ray at SPring-8, and precisely estimate the homogeneity at the atomic level of the CeO_2-ZrO_2 solid solution.

The mechanism of the OSC improvement is not yet completely understood. Especially, the oxygen environment around cations remains a matter of debate. The XAFS analysis only provides the average local structure. To clarify this point, we have to obtain detailed information on the structure of the homogeneous CeO_2-ZrO_2 solid solution. We plan to investigate the precise crystal structure of the homogeneous CeO_2-ZrO_2 solid solution by using synchrotron X-ray and pulsed neutron scattering.

Finally, through this research, we have determined an important guide that catalyst

design at the atomic level is necessary in order to develop high performance catalysts for practical use.

ACKNOWLEDGEMENTS

The X-ray absorption experiments were performed at the SPring-8 with the approval of the Japan Synchrotron Radiation Research Institute (JASRI) (Proposal No. 2000A0143-NX-np and C99B16B2-417N). We greatly thank Drs. Uruga and Tanida at SPring-8 for the X-ray measurements.

REFERENCES

[1] S. Matsumoto, *Toyota Tec. Rev.* **44** (1994) 10.

[2] Japanese unexamined patent publication, 116741 (1988).

[3] S. Matsumoto, N. Miyoshi, T. Kanazawa, M. Kimura, M. Ozawa, in S. Yoshida, N. Tabezawa, T. Ono (Eds.), *Catalysis Science and Technology*, **Vol. 1**, Kodansha/VCH, Tokyo/Weinheim, 1991, p. 335.

[4] M. Ozawa, M. Kimura, A. Isogai, *J. Alloys Comp.* **193** (1993) 73.

[5] T. Omata, H. Kishimoto, S. Otsuka-Yao-Matsuo, N. Ohtori, N. Umesaki, *J. Solid. State Chem.* **147** (1999) 573.

[6] G. Vlaic, P. Fornasiero, S. Geremia, J. Kašpar, M. Granziani, *J. Catal.* **168** (1997) 386.

[7] Y. Madier, C. Descorme, A. M. Le Govic, D. Duprez, *J. Phys. Chem. B* **103** (1999) 10999.

[8] E. Mamotov, T. Egami, R. Brezny, M. Koranne, S. Tyagi, *J. Phys. Chem. B* **101** (2000) 11110.

[9] H. Kishimoto, T. Omata, S. Otsuka-Yao-Matsuo, K. Ueda, H. Hosono, H. Kawazoe, *J. Alloys Comp.* **312** (2000) 94.

[10] S. Lemaux, A. Bensaddik, A.M.J. van der Earden, J.H. Bitter, D.C. Koningsberger, *J. Phys. Chem. B* **105** (2001) 4810.

[11] A. Suda, H. Sobukawa, T. Suzuki, T. Kandori, Y. Ukyo, M. Sugiura, *J. Ceram. Soc. Japan* **109** (2001) 177.

[12] Y. Nagai, T. Yamamoto, T. Tanaka, S. Yoshida, T. Nonaka, T. Okamoto, A. Suda, M. Sugiura, *J. Synchrotron Rad.* **8** (2001) 616.

[13] Y. Nagai, T. Yamamoto, T. Tanaka, *SPring-8 Research Frontiers* 1999/2000, p. 46.

[14] B.K. Teo, EXAFS: *Basic Principles and Data Analysis*, Springer, Berlin (1986).

[15] T. Uruga, H. Tanida, Y. Yoneda, K. Takeshita, S. Emura, M. Takahashi, M. Harada, Y. Nishihata, Y. Kubozono, T. Tanaka, T. Yamamoto, H. Maeda, O. Kamishima, Y. Takabayashi, Y. Nakata, H. Kimura, S. Goto, T. Ishikawa, *J. Synchrotron Rad.* **6** (1999) 143.

[16] T. Tanaka, H. Yamashita, R. Tsutitani, T. Funabiki, S. Yoshida, *J. Chem. Soc., Farad. Trans.* **84** (1988) 2987.

[17] P. Fornasiero, R. Di Monte, G. Rao Ranga, J. Kašpar, S. Meriani, A. Trovarelli, M. Granziani, *J. Catal.* **151** (1995) 168.

[18] T. Tanabe, A. Suda, C. Deccorme, D. Duprez, H. Shinjoh, M. Sugiura, *Stud. Surf. Sci. Catal.* **138** (2001) 135.

[19] P. Li, I.-W. Chen, J.E. Penner-Hahn, *Phys. Rev. B* **48** (1993) 10063.

[20] P. Li, I.-W. Chen, J.E. Penner-Hahn, *Phys. Rev. B* **48** (1993) 10074.

[21] R.D. Shannon, C.T. Prewitt, *Acta Cryst.* **B25** (1969) 925.

[22] Y.K. Voronko, A.A. Sobol, V.A. Ushakov, L.Y. Tsymbal, *Inorg. Mater.* **30** (1994) 747.

[23] T. Hirata, E. Asari, M. Kitajima, *J. Solid State Chem.* **110** (1994) 201.

[24] P. Li, I.-W. Chen, J.E. Penner-Hahn, *J. Am. Ceram. Soc.* **77** (1994) 1281.

[25] G. Balducci, J. Kašpar, P. Fornasiero, M. Granziani, M. S. Islam, J.D. Gale, *J. Phys. Chem. B* **101** (1997) 1750.

[26] H.C. Yao, Y.F. Yao, *J. Catal.* **86** (1984) 254.

[27] P. Fornasiero, G. Balducci, R. Di Monte, J. Kašpar, V. Sergo, G. Gubitosa, A. Ferrero, M. Granziani, *J. Catal.* **164** (1996) 173.

Chapter 3: Study on the thermal degradation of κ-$CeZrO_4$ solid solution by XAFS and XRD

ABSTRACT

The homogeneous CeO_2-ZrO_2 solid solution has an ordered cation arrangement, and exhibits the highest oxygen storage/release capacity (OSC) among a several types of CeO_2-ZrO_2 with the same composition (Ce/Zr = 1). The crystal structure of this CeO_2-ZrO_2 solid solution is usually termed as "κ-$CeZrO_4$ phase". Its OSC performance degrades upon a high-temperature treatment under an oxidative atmosphere. By using Ce K- and Zr K-edges XAFS and powder XRD, this research investigated the structural change along with the thermal degradation of κ-$CeZrO_4$. The fresh sample was aged at 973 K, 1273 K and 1473 K under an oxidative atmosphere, respectively. Their OSC performances were characterized at 773 K by thermo-gravimetric method. The OSC performance deteriorated as: the fresh sample ≈ 973 K > 1273 K > 1473 K-aged samples. We also found that, if the temperature was beyond 1273 K, the Ce/Zr ordered arrangement would collapse and the local structure around Ce and Zr ions would also changed remarkably. These results indicated that OSC was strongly dependent on its atomic structure.

1. INTRODUCTION

Oxygen storage/release capacity (OSC) is one of the important functions required for automotive three-way catalysts (TWCs), and plays a critical role for efficiently detoxifying the harmful compounds, such as hydrocarbons, CO and NOx in automotive exhaust [1]. In TWCs, Ceria is widely used for its high OSC based on the reversible redox reaction ($CeO_2 \leftrightarrow CeO_{2-x} + x/2\ O_2$; x = 0 - 0.5). The OSC performance and the durability of the pure CeO_2 were inadequate for a practical application in the actual TWCs. More than ten years ago, our laboratory discovered that the addition of ZrO_2 to CeO_2 enhances the OSC as well as improve its thermal stability [2-4]. Following this discovery, CeO_2-ZrO_2 has been widely utilized in the commercial catalysts. So far, a considerable number of studies have been focused on the physical properties and structure of CeO_2-ZrO_2, and a significant progress has been gained to deepen our understanding about this material [*e.g.* 5-11]. Recently, we discovered that, the homogeneous CeO_2-ZrO_2 solid solution had an ordered cation arrangement, and exhibited the highest OSC among a several types of CeO_2-ZrO_2 with the same composition (Ce/Zr = 1) [12, 13]. The crystal structure of this CeO_2-ZrO_2 solid solution is usually termed as "κ-$CeZrO_4$ phase" [9], which corresponds to CZ55-3 in Chapter 2. However, the OSC performance of κ-$CeZrO_4$ degrades upon a high-temperature treatment under an oxidative atmosphere. In order to develop more efficient TWCs, it is really meaningful to investigate and clarify what caused this thermal degradation. We assumed that the OSC exhibited a significant correlation with the molecular structure of the CeO_2-ZrO_2 samples. Therefore, it is presumed that this thermal degradation is resulted from the subtle structural change. In this research, we carried out powder XRD measurement to characterize the solid phase, and Ce K-edge and Zr K-edge XAFS

measurements to investigate the local structure around Ce and Zr. By using XAFS and powder XRD, we tried to investigate what exactly happened to its structure along with the thermal degradation of κ-$CeZrO_4$, and correlated with its OSC performance [14].

2. EXPERIMENTAL

2.1. Catalysts preparation and ageing treatment

CeO_2-ZrO_2 solid solution (Ce:Zr=1:1 molar ratio), which has κ-$CeZrO_4$ structure, was prepared by a coprecipitation process using $Ce(NO_3)_3$ and $ZrO(NO_3)_2$ aqueous solutions. The precipitate was reduced at 1473 K for 4 h with pure CO flowing and then oxidized in air at 773 K for 3 h. This sample is referred to as "fresh". The fresh sample was aged in air for 3h at 973 K, 1273 K and 1473 K, respectively. These obtained samples are referred as "aged". All the samples were finally calcined in air at 773 K prior to XAFS and XRD measurements. Through the above treatment, oxygen was fully stored in the Ce oxides.

2.2. Characterization

2.2.1. Oxygen storage/release capacity (OSC) measurements

The oxygen storage/release capacity (OSC) was estimated by thermo-gravimetric analysis [11]. The 1 wt% platinum loaded CeO_2-ZrO_2 samples were cyclically reduced by 20 % H_2 (N_2 balance) for 5 min then oxidized by 50 % O_2 (N_2 balance) for 5 min at 773 K. The weight loss and gain were measured using a thermo-gravimetric analyzer (TGA-50, Shimadzu Corp.). The reductive/oxidative conditions were maintained until the weight became constant. The value of the weight change between the reductive and oxidative conditions corresponds to the total OSC at 773 K.

2.2.2. Surface area measurements

The specific surface areas of the samples were estimated using the N_2 adsorption

isotherm at 77 K by the one-point Brunauer-Emmett-Teller (BET) method using an automatic surface analyzer (Micro Sorp 4232II, Micro Data Co., Ltd.). The samples were degassed in flowing N_2 at 473 K for 20 min.

2.2.3. X-Ray diffraction (XRD)

The powder XRD experiments were carried out using a RINT2000 (Rigaku Co., Ltd.) diffractometer with Cu-K_α radiation (1.5406 Å). The catalyst powder samples were pressed into wafers and affixed to standard-sized microscope slides. The identification of the phase was made with the help of the JCPDS cards (Joint Committee on Powder Diffraction Standards).

2.2.4. X-ray absorption fine structure (XAFS)

The Ce K-edge (40.45 keV) and Zr K-edge (18.00 keV) XAFS spectra were measured at BL01B1 and BL16B2 of SPring-8 (Hyogo, Japan). The storage ring energy was operated at 8 GeV with a typical current of 100 mA. The measurements were carried out using a Si (311) double crystal monochromator in the transmission mode at room temperature. Data reduction of the XAFS was carried out as described elsewhere [15]. The quantitative curve-fitting analysis of the EXAFS spectra was performed for the inverse Fourier transforms on the cation-cation (cation = Ce, Zr) and cation-oxygen shells. Empirical parameters in the analysis were obtained from standard compounds, e.g., cubic CeO_2 for Ce-Ce and Ce-O bonding, 8 mol% Y-doped cubic ZrO_2 for Zr-Zr and Zr-O bonding, and cubic $Ce_{0.9}Zr_{0.1}O_2$ for Zr-Ce bonding. The parameter for the Ce-Zr bonding was calculated from the extracted Ce-Ce, Zr-Zr and Zr-Ce parameters.

3. RESULTS AND DISCUSSION

3.1. OSC performances of fresh and aged samples.

Table 1 lists the OSC performances of the fresh and aged samples. The fresh sample exhibited a high OSC, and its Ce efficiency was 88.6 %. The OSC value of the 973 K-aged sample was almost equal to that of the fresh sample, while the OSC performance gradually decreased with increasing aging temperature. The OSC value of the 1473 K-aged sample was about 40 % of that of the fresh sample.

Table 1. OSC properties of the fresh and the aged κ-$CeZrO_4$ samples.

Sample [a)]	OSC [b)] (μmol-O_2/g)	Ce efficiency [c)] (%)
Fresh	750	88.6
973 K-aged	772	91.0
1273 K-aged	483	56.9
1473 K-aged	283	35.0

a) The fresh sample was aged in air at the indicated temperatures.
b) OSC (Oxygen Storage/Release Capacity) was measured at 773 K.
c) The ratio $Ce^{3+}/(Ce^{3+} + Ce^{4+})$ under the reductive condition.

3.2. XRD analysis

Figure 1 shows the XRD patterns of the fresh and aged κ-$CeZrO_4$ samples. For the fresh sample, we could observe small peaks, which marked here with an asterisk, except for the principal peaks which were attributed to the cubic fluorite $CeZrO_4$. These small peaks are characteristic of κ-$CeZrO_4$ due to the ordered arrangement of the cations

along the <110> direction similar to the pyrochlore-type precursor, as shown in Figure 2. The lattice parameter of κ-$CeZrO_4$ phase was a = 1.052 nm. This κ-structure was still maintained upon aging at 973 K. However, the ordering peaks disappeared upon aging at 1273 K or higher, and only the principal peaks of cubic $CeZrO_4$ remained observable. In addition, the principal peaks for the 1473 K-aged sample became broad and begun to split partially. Therefore, we can assume that a phase separation occurred at 1473 K, and that the $CeZrO_4$ solid solution becomes partially divided into more stable CeO_2 and ZrO_2.

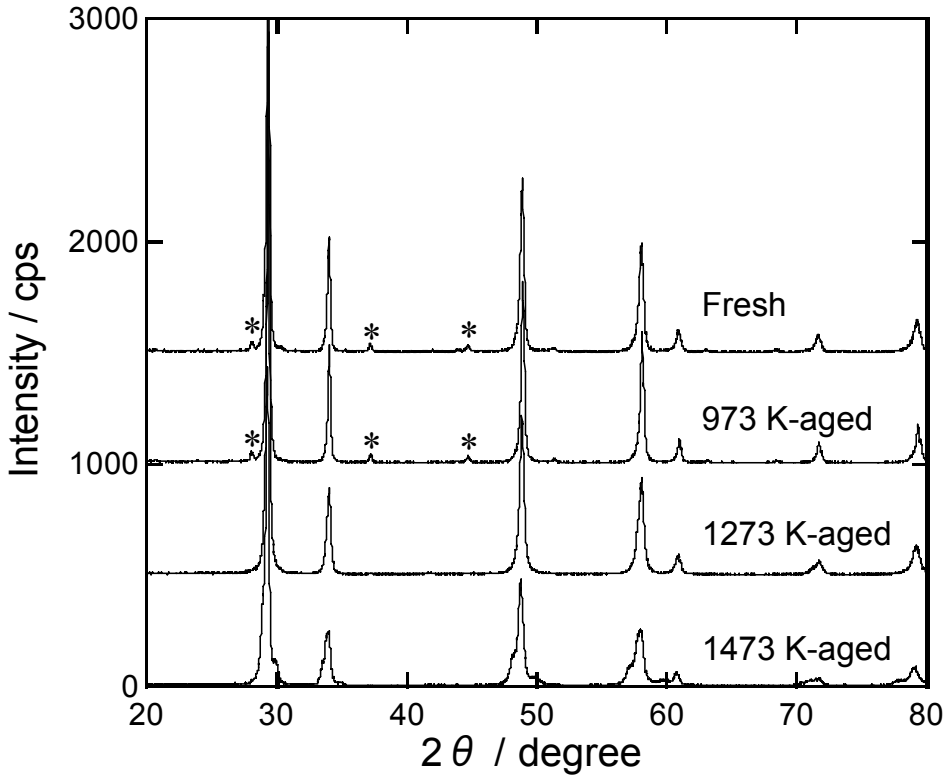

Figure 1. X-Ray diffraction patterns of the fresh and aged κ-$CeZrO_4$ samples. Small peaks marked with asterisks are characteristic of κ-$CeZrO_4$ due to the ordered arrangement of the cations.

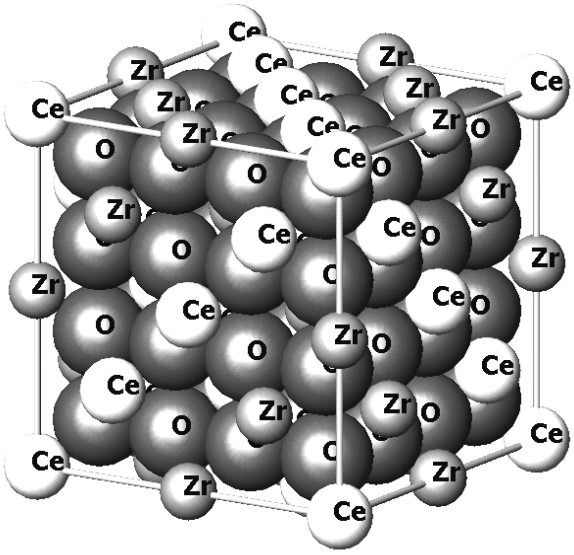

Figure 2. Crystal structure of κ-$CeZrO_4$ determined by XRD.

3.3. XAFS analysis

Fourier transforms (FTs) were carried out the Ce K- and Zr K-edges EXAFS spectra in about the 3.0 - 16 $Å^{-1}$ region. FTs of the Ce K-edge are presented in Figure 3 (a). The first peak at 1.8 Å and the second peak at 3.5 Å correspond to the Ce-O and Ce-cation (cation = Ce, Zr) bonds, respectively. The Ce-O and Ce-cation peaks of the 973 K-aged sample are located at the same positions as those of the fresh sample and have the same amplitude. On the other hand, the shapes of the FTs for the 973 K, 1273 K and 1473 K-aged samples are obviously different. Figure 3 (b) shows the FTs of the Zr K-edge EXAFS spectra. The first peak at 1.7 Å was assigned to Zr-O bonds and the second peak at 3.5 Å to Zr-cation bonds. The same observation for the Ce K-edge also applies to the Zr K-edge XAFS. The spectra of the fresh and 973 K-aged samples have the same features. The spectra of the aged samples are different from each other.

The XANES spectra at the Zr K-edge are shown in Figure 4. First, peak *A* was

more apparent for the 1273 K and 1473 K-aged samples than those of the fresh and 973 K-aged ones. As we mentioned in Chapter 2, this pre-edge absorption can be assigned to the 1s → 4d which is sensitive to the cation-O geometry. Especially, this pre-edge absorption is considerably strong in the case of pure tetragonal ZrO_2. Thus, it is clear that the 1273 K and 1473 K-aged samples have a tetragonal environment of the Zr-O coordination. As for peak *B*, it was in the form of a slight splitting in the 1273 K and 1473 K-aged samples, although it exhibited a clear splitting in the fresh and 973 K-aged samples. A clear splitting like this could also be observed for cubic ZrO_2. Clearly, the fresh and 973 K-aged samples have a cubic environment of the Zr-O coordination.

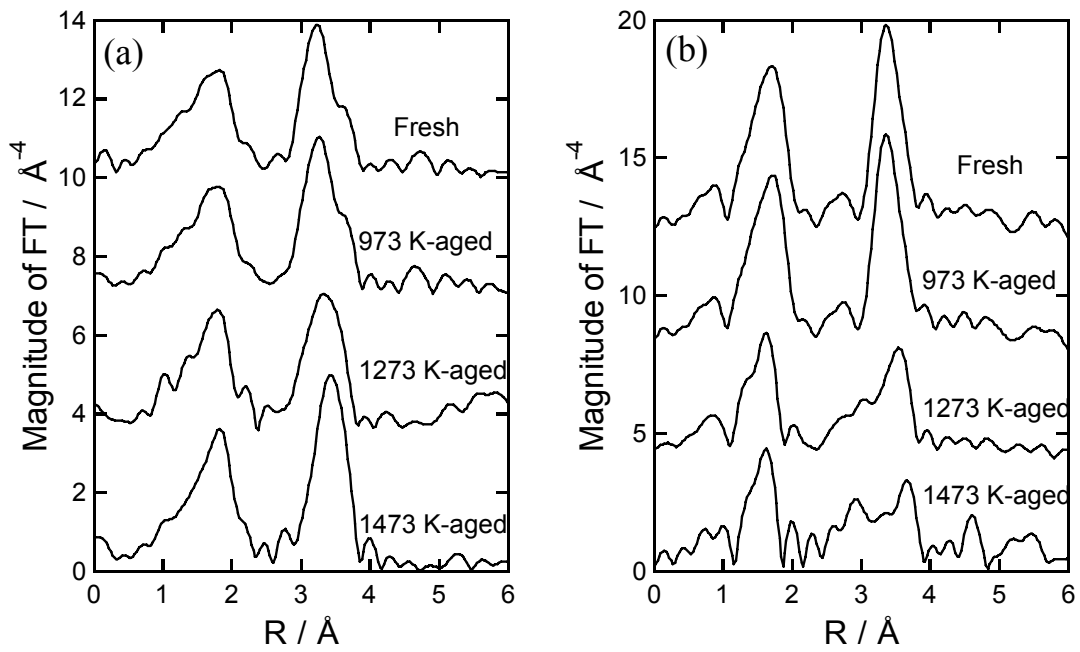

Figure 3. Fourier-transformed k^3x data of (a) Ce K-edge and (b) Zr K-edge EXAFS of the fresh and aged κ-$CeZrO_4$ samples.

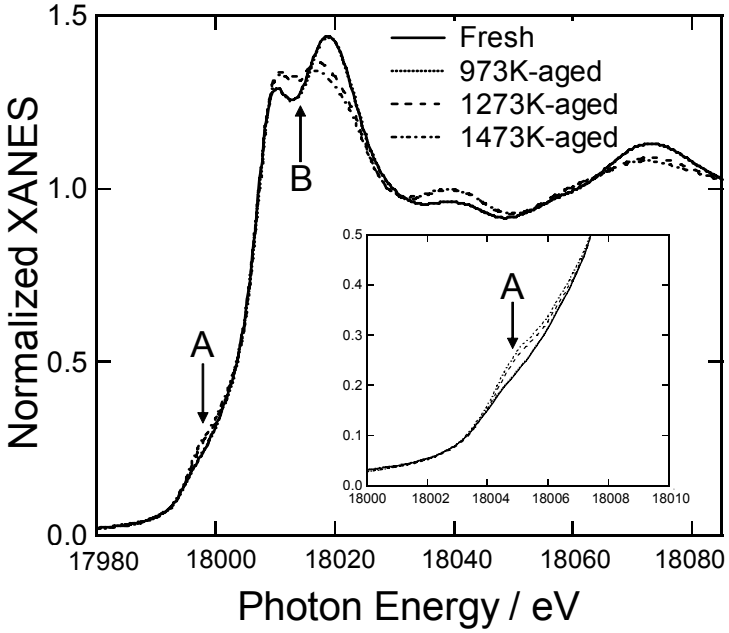

Figure 4. Zr K-edge XANES spectra of the fresh and aged κ-$CeZrO_4$ samples.

3.4. Cation-Cation network

A quantitative curve-fitting analysis was performed for the cation-cation shells in the FTs to clarify this network. The curve-fitting results of the Ce and Zr K-edges EXAFS are summarized in Tables 2 and 3, respectively. Figure 5 shows a model illustration of the cation-cation network for the CeO_2-ZrO_2 samples, which is proposed from the curve-fitting analysis. In the case of fresh and 973 K-aged samples, all the CNs of cation shells could be fitted to 6, and the CN ratios of Ce to Zr and Zr to Ce were exactly 1.This CN ratio was consistent with the composition ratio. Clearly, in these samples, homogeneous solid solution forms at an atomic level. Furthermore, as we mentioned in the XRD section, fresh and 973 K-aged samples possess an ordered arrangement of Ce and Zr ions (Figure 5 (a)). Secondly, all the CNs of cation shells for 1273 K-aged samples was also fitted to 6. However, the relative Debye-Waller factor ($\Delta\sigma^2$) of Zr-Zr bond for 1273 K-aged sample was too large. This indicates the presence of some structural disorder in the Zr-Zr bond distances for 1273 K-aged sample. Additionally, from the above XRD results, the ordering peaks disappeared upon aging at 1273 K. It follows from these results that the small portion of Zr ions is separated from the cubic CeO_2 framework, and that the homogeneity of Ce and Zr atom in 1273 K-aged sample is not perfect but quasi (Figure 5 (b)). Thirdly, in the case of the 1473 K-aged sample, the CN of Ce-Ce bond was not equal to that of Ce-Zr bond. Moreover, a reasonable fitting for Zr-cation shell could not be obtained. This is regarded to be caused by the partial phase separation. This result was in accord with the XRD data. The part of the CeO_2-ZrO_2 solid solution was divided into stable CeO_2 and ZrO_2 (Figure 5 (c)).

Table 2. Results of curve-fitting analysis of the fresh and the aged κ-$CeZrO_4$ samples for Ce-cation shells [a)]

Sample	Bond	Coordination Number	Length (Å)	$\Delta\sigma^{2}$ [b)] ($Å^2$)
Fresh	Ce-Ce	6.0(3)	3.78(0)	0.0016(2)
	Ce-Zr	6.0(3)	3.72(0)	0.0022(3)
973 K-aged	Ce-Ce	6.0(3)	3.78(0)	0.0032(3)
	Ce-Zr	6.0(3)	3.71(0)	0.0026(2)
1273 K-aged	Ce-Ce	6.0(1)	3.76(0)	0.0013(1)
	Ce-Zr	6.0(3)	3.68(0)	0.0042(3)
1473 K-aged	Ce-Ce	8.0(4)	3.79(0)	0.0020(2)
	Ce-Zr	3.6(5)	3.69(0)	0.0016(5)

a) The standard deviation is given in parentheses.
b) Relative Debye-Waller factor

Table 3. Results of curve-fitting analysis of the fresh and the aged κ-$CeZrO_4$ samples for Zr-cation shells [a)]

Sample	Bond	Coordination Number	Length (Å)	$\Delta\sigma^{2}$ [b)] ($Å^2$)
Fresh	Zr-Zr	6.0(4)	3.62(0)	0.0086(6)
	Zr-Ce	6.0(3)	3.75(0)	-0.0010(1)
973 K-aged	Zr-Zr	6.0(2)	3.63(0)	0.0044(2)
	Zr-Ce	6.0(2)	3.76(0)	0.0020(2)
1273 K-aged	Zr-Zr	6.0(2)	3.74(0)	0.0669(8)
	Zr-Ce	6.0(2)	3.75(0)	-0.0011(7)
1473 K-aged	Zr-Zr	— [c]	— [c]	— [c]
	Zr-Ce			

a) The standard deviation is given in parentheses.
b) Relative Debye-Waller factor
c) Reasonable fit could not be obtained.

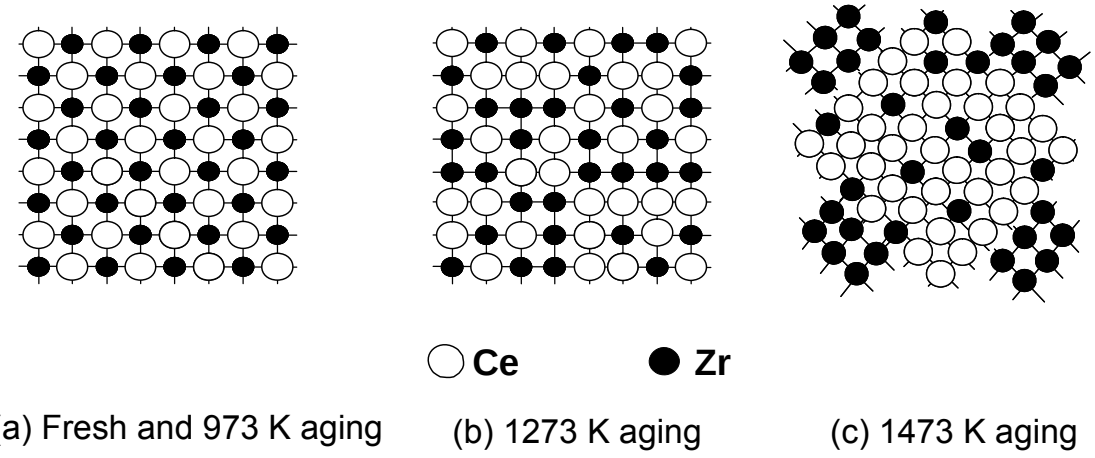

Figure 5. Model illustration of cation-cation network for the fresh and aged κ-$CeZrO_4$ samples.

3.5. Oxygen environment around cation

The quantitative curve-fitting results of Ce-oxygen and Zr-oxgen shells are presented in Tables 4 and 5, respectively. First, all the Ce-O shells were fitted with a single Ce-O bond, and the CN for all samples was 8. This indicates that Ce-O coordination for all samples has a symmetric 8-fold coordination. The Ce-O bond length gradually shortens in the order of 973 K-aged, 1273 K-aged and 1473 K-aged samples. Secondly, the Zr-O shells for the fresh and 973 K-aged samples were fitted with a single Zr-O bond. In contrast, the Zr-O shell for the 1273 K-aged sample was fitted with two sets of short and long Zr-O bond lengths. These short and long bond lengths and the CN (4 + 4) of Zr-O are close to the values for the typical tetragonal ZrO_2 [16]. But the distances of Zr-O for the 1273 K-aged sample is not equal to the values for the pure tetragonal ZrO_2, because a $CeZrO_4$ solid solution in the 1273 K-aged sample forms. These results indicate that Zr-O coordination in the fresh and 973 K-aged samples have a symmetric 8-fold coordination, while Zr-O coordination in the 1273 K-aged sample has two sets of nonequivalent tetrahedral geometry. This result is in agreement with the

Zr K-edge XANES data. Although we could not obtain a reasonable fitting for the Zr-O shell of the 1473 K-aged sample caused by the partial phase separation, we can determine from the Zr K-edge XANES that this sample also has the above tetrahedral geometry.

Table 4. Results of curve-fitting analysis of the fresh and the aged κ-$CeZrO_4$ samples for Ce-oxygen shells [a)]

Sample	Bond	CN	R (Å)	$\Delta\sigma^2$ [b] ($Å^2$)
Fresh	Ce-O	8.0(2)	2.27(0)	0.0044(2)
973 K-aged	Ce-O	8.0(1)	2.27(0)	0.0035(1)
1273 K-aged	Ce-O	8.0(1)	2.29(0)	0.0039(1)
1473 K-aged	Ce-O	8.0(1)	2.30(0)	0.0032(1)

a) The standard deviation at the last digit is given in parentheses.
b) Relative Debye-Waller factor

Table 5. Results of curve-fitting analysis of the fresh and the aged κ-$CeZrO_4$ samples for Zr-oxygen shells [a)]

Sample	Bond	CN	R (Å)	$\Delta\sigma^2$ [b] ($Å^2$)
Fresh	Zr-O	8.0(2)	2.27(0)	-0.0046(2)
973 K-aged	Zr-O	8.0(5)	2.26(0)	-0.0081(2)
1273 K-aged	Zr-O	4.0(5)	2.18(0)	-0.0072(5)
	Zr-O	4.0(5)	2.36(2)	0.0063(45)
1473 K-aged	Zr-O	— [c]	— [c]	— [c]

a) The standard deviation is given in parentheses.
b) Relative Debye-Waller factor
c) Reasonable fit could not be obtained.

3.6. Thermal degradation of κ-$CeZrO_4$ and its structure

The relationship between the thermal degradation of κ-$CeZrO_4$ and its structure was summarized in Table 4. The OSC performance degraded in the order: the fresh sample ≈ 973 K > 1273 K > 1473 K-aged samples. We found that κ-structure was still maintained at 973 K, but Ce/Zr ordering had broken at 1273 K. The solid solution was partially divided into CeO_2 and ZrO_2 at 1473 K. The homogeneity of the Ce and Zr atom decreased in the order: the fresh sample ≈ 973 K > 1273 K > 1473 K-aged samples. Moreover, Zr-O geometry also changed remarkably along with the thermal degradation.

It was observed in the Chapter 2 that the OSC performance strongly depends on its atomic structure. It was suggested that the OSC was dependent on the points of the homogeneity and the oxygen environment. The OSC increases by enhancing the homogeneity of the Ce and Zr atoms in the CeO_2-ZrO_2 solid solution. Especially, an atomically homogeneous $Ce_{0.5}Zr_{0.5}O_2$ solid solution exhibited the highest OSC among these CeO_2-ZrO_2 samples. The enhancement of the homogeneity of the Ce and Zr atoms could ease the valence change of the Ce ($Ce^{4+} \rightarrow Ce^{3+}$). The introduction of downsized Zr (Zr^{4+}; 0.84 Å) ions into the Ce (Ce^{4+}; 1.14 Å) framework could compensate for the volume increment, and ease the valence change ($Ce^{4+} \rightarrow Ce^{3+}$). In this thermal degradation of κ-$CeZrO_4$, the homogeneity of the Ce and Zr atom of CeO_2-ZrO_2 solid solution decreased in the order: the fresh sample ≈ 973 K > 1273 K > 1473 K-aged samples. Therefore, this the point of the homogeneity makes it clear that the OSC performance degrades in the order: the fresh sample ≈ 973 K > 1273 K > 1473 K-aged samples. Secondly, by the atomically homogeneous introduction of Zr ions into the cubic CeO_2 framework, the Ce-O bond length shortens, and the configuration of the oxygen around Zr has a more centrosymmetric coordination. In particular, the fresh and

973 K-aged samples have a good symmetric 8-fold coordination around the Zr. This symmetric 8-fold coordination state around Zr is generally considered to be spatially tight and unstable, because the ionic radius of Zr^{4+} (0.84 Å) is much smaller than that of O^{2-} (1.38 Å) [17]. On the other hand, the oxygen environment around Ce for the fresh and 973 K-aged samples is also considered to be tight, because the Ce-O bond length for these samples is much shorter than that for the stable pure CeO_2. This instability of the oxygen environment around Ce and Zr will generate some active oxygen which is responsible for the improved OSC. In the thermal degradation of κ-$CeZrO_4$, this instability of the oxygen environment decreased in the order: the fresh sample ≈ 973 K > 1273 K > 1473 K-aged samples. The κ-$CeZrO_4$ solid solution is not a stable phase but a metastable one in an oxidative atmosphere. A phase separation occurs in the oxidative atmosphere at high temperatures of 1273 K and above, and part of the κ-$CeZrO_4$ solid solution is divided into stable CeO_2 and ZrO_2.

Table 4. Thermal degradation of κ-$CeZrO_4$ and its structure.

Sample	Fresh and 973 K-aged	1273 K-aged	1473 K-aged
OSC performance	High	Medium	Low
Ce/Zr ordering	Ordered	Disordered	Disordered
Ce/Zr homogeneity	Homogeneous	Quasi-homogeneous	Phase separation
Ce-O geometry	Cubic	Cubic	Cubic
Ce-O bond length	Long	Medium	Short
Zr-O geometry	Cubic	Tetrahedral	Tetrahedral

4. CONCLUSIONS

We could clarify the thermal degradation of κ-$CeZrO_4$ and its structure under an oxidative atmosphere at high temperature. The OSC performance deteriorated in the order: the fresh sample ≈ 973 K > 1273 K > 1473 K-aged samples.

Furthermore, we found that the κ-structure was still maintained upon aging at 973 K. However, if the temperature went beyond 1273 K, the Ce/Zr ordered arrangement would collapse. A phase separation occurred at 1473 K, and that the $CeZrO_4$ solid solution becomes partially divided into more stable CeO_2 and ZrO_2. The homogeneity of the Ce and Zr atom decreased in the order: the fresh sample ≈ 973 K > 1273 K > 1473 K-aged samples. Moreover, Zr-O and Ce-O geometry also changed remarkably in aged samples.

The OSC was dependent on the points of the homogeneity and the oxygen environment. Since the enhancement of the homogeneity of the Ce and Zr atoms could ease the valence change of the Ce ($Ce^{4+} \rightarrow Ce^{3+}$), the OSC increases by enhancing the homogeneity of the Ce and Zr atoms in the CeO_2-ZrO_2 solid solution. The lowering of the homogeneity of Ce and Zr would be the main reason why the OSC performance of κ-$CeZrO_4$ degrades upon a high-temperature treatment under an oxidative atmosphere. Additionally, the instability of the oxygen environment around Ce and Zr will generate some active oxygen which is responsible for the high OSC. In the thermal degradation of κ-$CeZrO_4$, this instability of the oxygen environment decreased in the order: the fresh sample ≈ 973 K > 1273 K > 1473 K-aged samples. These results indicated that OSC strongly depends on its atomic structure, and hinted us a key point on how to enhance or optimize the oxygen storage performance involved in three way catalysts.

ACKNOWLEDGEMENTS

The X-ray absorption experiments were performed at the SPring-8 with the approval of the Japan Synchrotron Radiation Research Institute (JASRI) (Proposal No. 2000A0143-NX-np, C99B16B2-417N and C01A16B2-4020N). We greatly thank Dr. Uruga and Dr. Tanida at SPring-8 for the X-ray measurements.

REFERENCES

[1] S. Matsumoto, *Catal. Today* **90** (2004) 183.

[2] Japanese unexamined patent publication, 116741 (1988).

[3] S. Matsumoto, N. Miyoshi, T. Kanazawa, M. Kimura and M. Ozawa, in S. Yoshida, N. Tabezawa and T. Ono (Editor), *Catal. Sci. & Tech.*, **Vol. 1**, Kodansha-VCH, 1991, p. 335.

[4] M. Ozawa, M. Kimura and A. Isogai, *J. Alloys Comp*. **193** (1993) 73.

[5] T. Omata, H. Kishimoto, S. Otsuka-Yao-Matsuo, N. Ohtori and N. Umesaki, *J. Solid. State Chem.* **147** (1999) 573.

[6] G. Vlaic, P. Fornasiero, S. Geremia, J. Kašpar and M. Granziani, *J. Catal.* **168** (1997) 386.

[7] Y. Madier, C. Descorme, A. M. Le Govic and D. Duprez, *J. Phys. Chem. B* **103** (1999) 10999.

[8] E. Mamotov, T. Egami, R. Brezny, M. Koranne and S. Tyagi, *J. Phys. Chem. B* **101** (2000) 11110.

[9] H. Kishimoto, T. Omata, S. Otsuka-Yao-Matsuo, K. Ueda, H. Hosono and H. Kawazoe, *J. Alloys Comp.* **312** (2000) 94.

[10] S. Lemaux, A. Bensaddik, A. M. J. van der Earden, J. H. Bitter and D. C. Koningsberger, *J. Phys. Chem. B* **105** (2001) 4810.

[11] A. Suda, H. Sobukawa, T. Suzuki, T. Kandori, Y. Ukyo and M. Sugiura, *J. Ceram. Soc. Japan* **109** (2001) 177.

[12] Y. Nagai, T. Yamamoto, T. Tanaka, S. Yoshida, T. Nonaka, T. Okamoto, A. Suda and M. Sugiura, *J. Synchrotron Rad.* **8** (2001) 616.

[13] Y. Nagai, T. Yamamoto, T. Tanaka, S. Yoshida, T. Nonaka, T. Okamoto, A. Suda, M.

Sugiura, *Catal. Today* **74** (2002) 225.

[14] Y. Nagai, T. Yamamoto, T. Tanaka, T. Nonaka, A. Suda, *Physica Scripta* **T115** (2002) 664.

[15] T. Tanaka, H. Yamashita, R. Tsutitani, T. Funabiki and S. Yoshida, *J. Chem. Soc., Farad. Trans.* **84** (1988) 2987.

[16] P. Li, I-W. Chen and J. E. Penner-Hahn, *Phys. Rev. B* **48** (1993) 10063.

[17] R.D. Shannon, C.T. Prewitt, *Acta Cryst.* **B25** (1969) 925.

Chapter 4: Oxidation reaction of *n*-hexane and sulfur dioxide in diesel simulated exhaust gases over platinum loaded zirconia

ABSTRACT

We examined the oxidation reaction of n-C_6H_{14} and SO_2 over two types of Pt/ZrO_2 catalysts with low (8 m^2/g) and high (75 m^2/g) surface areas of the ZrO_2 supports (referred to as ZrO_2-8 and ZrO_2-75, respectively). The catalytic activity was evaluated under simulated diesel exhaust gas which simultaneously contained n-C_6H_{14} and SO_2. The Pt/ZrO_2-75 exhibited a desirably higher selectivity for the complete oxidation of n-C_6H_{14} than that of SO_2, as compared with the Pt/ZrO_2-8. In order to clarify the cause of this selective oxidation, we investigated the Arrhenius parameter for these oxidation reactions and characterized these catalysts using XPS, XRD, TEM, IR and CO_2-TPD methods. The amount of Pt^0 (metal) in the Pt/ZrO_2-75 was significantly lower than that in Pt/ZrO_2-8, because the high basicity of the ZrO_2-75 support stabilized the high oxidation state of Pt such as Pt^{2+} and Pt^{4+}. It was concluded that the difference in the number of Pt^0 sites as catalytic active sites causes the apparent selectivity to change due to the much slower reaction rate for the SO_2 oxidation than that for the n-C_6H_{14} oxidation.

1. INTRODUCTION

Diesel emissions are composed of three phases; (1) solids (carbon or soot); (2) liquids (soluble organic fraction and liquid sulfate); and (3) gases (CO, hydrocarbon compounds, NOx and SO_2). The complete oxidation of carbon, CO and hydrocarbon (HC) compounds is required for the diesel oxidation catalyst [1, 2]. However, any sulfur compound contained in the diesel fuel is oxidized to SO_2 during the engine combustion cycle. In the presence of an oxidation catalyst, SO_2 is further oxidized to SO_3, which quickly reacts with the moisture in the exhaust to form sulfate. The sulfate leads to an increase in the weight of the total particulates emitted from the diesel engine and also causes acid rain. Therefore, a highly selective oxidation catalyst, which has a higher oxidation activity for carbon, CO and HC compounds than that for SO_2, is required.

Although it is important to investigate the key factor in developing a highly selective oxidation catalyst, surprisingly, few studies have been conducted [3]. In this study, we examined the oxidation of *n*-hexane (gaseous HC) and SO_2 over two types of Pt/ZrO_2 catalysts with low and high ZrO_2 support surface areas. These Pt/ZrO_2 catalysts exhibited different selectivity for the oxidation of *n*-hexane and SO_2. The purpose of this study is to clarify the cause of this oxidation selectivity. For this purpose, we investigated the Arrhenius parameter for this oxidation reaction and characterized the catalysts using XPS, XRD, TEM, IR and CO_2-TPD methods.

We employed *n*-hexane as a gaseous HC, because many *n*-alkane species are contained in the exhaust gas phase [4]. A number of studies have been conducted on the complete catalytic oxidation of the C_1-C_3 hydrocarbons such as methane, ethane, propane, etc. [*e.g.*, 5-9]. Actual exhaust gases include alkanes with a carbon number

higher than C_3. Therefore, we chose *n*-hexane as the HC species. Besides, few studies on the complete catalytic oxidation of hexane (C_6) have been reported. In addition to the foregoing main purpose of clarifying the cause of the reaction selectivity, another purpose of this study is to estimate the complete oxidation of *n*-hexane over platinum catalysts.

2. EXPERIMENTAL

2.1. Catalyst preparation

The two types of Pt/ZrO_2 catalysts examined for this study are summarized in Table 1 with the corresponding BET surface areas and ZrO_2 phase. The low surface area zirconia (referred as to ZrO_2-8) was supplied by Mitsuwa Chemicals, Japan. On the other hand, the high surface area zirconia (referred as to ZrO_2-75) was prepared by calcining $Zr(OH)_4$ (Hayashi Pure Chemical Industries, Japan) in air at 500°C for 3 h. The Pt/ZrO_2 catalysts were prepared by the wet impregnation of ZrO_2 powders with a $Pt(NH_3)_2(NO_2)_2$ (Tanaka Precious Metals, Japan) aqueous solution. The impregnated powders were dried overnight at 110°C and calcined at 500°C for 3 h in air. The amount of Pt loading of these catalysts was 0.64 wt.%. Also, Pt/SiO_2 (SiO_2 Nippon Aerosil Co., Ltd., specific surface area: 50 m^2/g) catalysts with several Pt loading amounts were prepared as references. The catalysts for the activity measurement were pressed into disks and pulverized to 1.0–2.0 mm size.

Table 1. The Pt/ZrO_2 catalysts, the BET surface areas and phase identification of ZrO_2.

Catalyst [a]	Pt loading (wt. %)	BET surface area of ZrO_2 (m^2 / g)	Phase of ZrO_2
Pt/ZrO_2-8	0.64	8	Monoclinic
Pt/ZrO_2-75	0.64	75	Tetragonal + Monoclinic

[a] For catalyst description, see Experimental.

2.2. Activity measurement

The catalytic activity was determined by using a conventional fixed-bed flow

reactor at atmospheric pressure. The reaction temperature was detected by a thermocouple inserted into the catalyst bed, and controlled from 500 °C to 150 °C at a rate of -6°C min^{-1}. The simulated exhaust gas was composed of 100 ppm *n*-hexane, 50 ppm SO_2, 10% O_2, 5 % CO_2, 10 % H_2O and the balance N_2. The total flow rate was 8.36 l/min and 3.6 g of catalyst was used. The concentration of the HC and SO_2 were continuously analyzed by a flame ionization detector and a flame photometric detector, respectively. The pre-treatment was carried out at 500 °C in the same flowing gas until the conversions of HC and SO_2 became constant. The conversions of HC and SO_2 were calculated based on the following equation:

$$\text{Conversion (\%)} = (X_{in} - X_{out}) / X_{in} \times 100 \quad (1)$$

where X_{in} and X_{out} are the concentrations of HC or SO_2 entering and leaving the catalyst bed, respectively.

The Arrhenius parameter measurements were made using the same above-mentioned conditions, except using the feed gas without CO_2 and H_2O. The Arrhenius parameters were calculated from the conversions of HC and SO_2 at less than about 15 %.

2.3. Catalyst characterization

2.3.1. Surface area measurements

The specific surface areas of the samples were estimated using the N_2 adsorption isotherm at 77 K by the one-point Brunauer-Emmett-Teller (BET) method with an automatic surface analyzer (Micro Sorp 4232II from Micro Data Co., Ltd.). The samples were degassed in flowing N_2 at 200 °C for 20 min.

2.3.2. X-Ray diffraction (XRD)

The powder XRD experiments were carried out using a RINT2000 (Rigaku Co., Ltd.) diffractometer with Cu-K_α radiation (1.5406 Å). The catalyst powder samples were pressed into wafers and affixed to standard-sized microscope slides. The identification of the phase was made by comparison to the JCPDS cards (Joint Committee on Powder Diffraction Standards). The average particle size of Pt was estimated from the Pt(1 1 1) line width using Scherrer's equation with the Gaussian line shape approximation.

2.3.3. Transmission electron micrograph (TEM)

TEM images were obtained using a JEOL JEM-2000EX. The accelerating voltage was 200 keV. The samples used for the measurement were pretreated at 400°C in air for 30 min.

2.3.4. X-ray photoelectron spectra (XPS)

The XPS measurements were carried out using a PHI model 5500MC with Mg K_α X-rays. The catalyst sample was placed on a grid, and pretreated under 0.1 atm O_2 pressure at 400°C for 15 min. The pretreated sample was cooled to room temperature, and then transferred to the XPS measurement stage. The Pt 4f core electron levels were recorded. The oxidation state and its proportion of Pt species were investigated by using reported BE values of Pt^{n+}(n = 0, 2, 4) [10, 11].

2.3.5. Infrared (IR) spectra

The IR spectra were recorded using a JASCO FT/IR-8900 spectrometer equipped

with a diffuse reflectance attachment (JASCO DR-800/H) and an MCT detector. The catalyst sample placed in an *in situ* IR cell with a KBr window was pretreated at 400°C for 20 min in flowing 7 % O_2/N_2 and then cooled to 200°C. The chemisorption of CO was then performed in flowing 0.28 % CO/N_2 at 200°C. The IR spectra of CO adsorbed on the sample were obtained by subtracting the spectra before the CO adsorption from those after the adsorption.

2.3.6. CO_2 temperature-programmed desorption (TPD) experiments

The basicity of the zirconia was measured by CO_2-TPD. The TPD experiments were carried out using the same experimental set-up as that used for the activity measurements. An 18 g sample was pretreated at 500°C for 15 min in flowing N_2 (5 l/min), cooled to 100°C, then saturated with a 0.26 % CO_2/ N_2 flowing gas mixture. After purging the sample with the N_2 gas, the sample was heated to 400°C at the rate of 50°C/min in flowing N_2 (5 l/min). The concentration of the desorbed CO_2 was analyzed by a nondispersive infrared detector.

3. RESULTS AND DISCUSSION

3.1. Catalytic activity

Figs. 1(a) and (b) show the conversion of *n*-C_6H_{14} and SO_2 on the Pt/ZrO_2-8 and Pt/ZrO_2-75 catalysts, respectively, as a function of temperature. The conversion of both on Pt/ZrO_2-8 reached over 80 % at 400°C. In contrast, it is noteworthy that the SO_2 conversion on Pt/ZrO_2-75 is much lower than that on Pt/ZrO_2-8. The Pt/ZrO_2-75 catalyst has only a 20 % SO_2 conversion at 400°C. The temperature at 50 % *n*-C_6H_{14} conversion on Pt/ZrO_2-75 was 296°C, which was somewhat higher than that (273°C) on Pt/ZrO_2-8. The ΔT shown in Figure 1 denotes the temperature difference between the 50 % conversion of *n*-C_6H_{14} and SO_2. The ΔT (203°C) of Pt/ZrO_2-75 was much wider than that (65°C) of Pt/ZrO_2-8. Therefore, the Pt/ZrO_2-75 catalyst has a desirably higher selectivity for the oxidation of *n*-C_6H_{14} than that of SO_2.

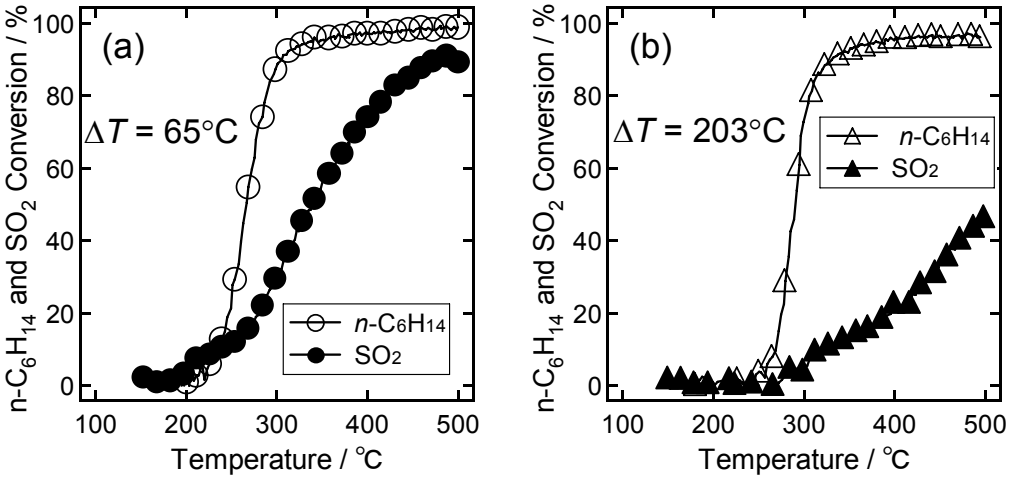

Figure 1. *n*-C_6H_{14} and SO_2 conversion efficiency as a function of temperature. (a) Pt/ZrO_2-8, (b) Pt/ZrO_2-75. ΔT denotes the temperature difference between the 50 % *n*-C_6H_{14} and SO_2 conversion efficiencies.

3.2. Arrhenius parameters

The Arrhenius plots for the rates of the *n*-C_6H_{14} and SO_2 conversions are shown in Figs. 2 (a) and (b), respectively. All the data points obtained with the Pt/ZrO_2-8 and Pt/ZrO_2-75 catalysts provide a linear relationship. The apparent activation energy (*E*a) and the pre-exponential factor (*A*) calculated from the Arrhenius plots are summarized in Table. 2. First, the Pt/ZrO_2-8 and Pt/ZrO_2-75 catalysts have almost same *E*a value for the *n*-C_6H_{14} oxidation, suggesting that these catalysts have identical active sites. On the other hand, the *A* value for the *n*-C_6H_{14} oxidation on Pt/ZrO_2-8 is one order of magnitude greater than that on Pt/ZrO_2-75. The term *A* is interpreted as being proportional to the number of catalytic active sites. Thus, an increase in *A* on Pt/ZrO_2-8 indicates an increase in the number of active sites. Secondly, the *E*a for the SO_2 oxidation on Pt/ZrO_2-8 is somewhat higher than that on Pt/ZrO_2-75, but its difference is not much greater, therefore, these catalysts would have identical active sites. As for the *A* value of the SO_2 oxidation, the same trend as for the *n*-C_6H_{14} oxidation is observed. Based on the results mentioned above, it is suggested that for the oxidation of *n*-C_6H_{14} and SO_2, these catalysts have identical active sites, and that the number of active sites on Pt/ZrO_2-8 is one order of magnitude greater than that on Pt/ZrO_2-75.

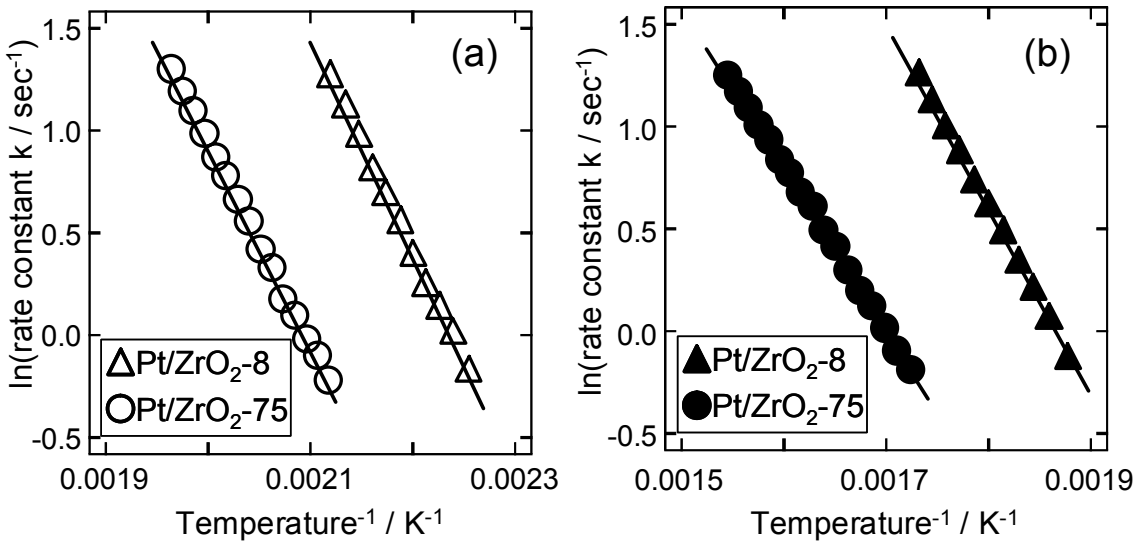

Figure 2. Arrhenius plots for the oxidations of (a) *n*-C_6H_{14} and (b) SO_2.

Table 2. Apparent activation energies (*E*a) and pre-exponential terms (*A*) for the oxidation of *n*-C_6H_{14} and SO_2 over Pt/ZrO_2 catalysts.

Catalyst	*E*a (kcal / mol)		*A* (1/sec)	
	n-C_6H_{14}	SO_2	*n*-C_6H_{14}	SO_2
Pt/ZrO_2-8	21	19	3.2×10^{10}	5.6×10^{7}
Pt/ZrO_2-75	20	17	1.4×10^{9}	1.1×10^{6}

3.3. Characterization of catalysts

3.3.1. Average platinum particle size of the Pt/ZrO_2 catalysts

Table 3 shows the average platinum particle size of the catalysts estimated by XRD and TEM. The diffraction peaks from the Pt particles in both Pt/ZrO_2-8 and Pt/ZrO_2-75 could not be detected due to their small particle size. The average particle size in Pt/ZrO_2-8 estimated by TEM was 1 – 4 nm. On the other hand, the Pt particles in

Pt/ZrO_2-75 could not be observed even by TEM, suggesting that the Pt particle size in Pt/ZrO_2-75 was less than 1 nm. It is found that the Pt/ZrO_2-75 catalyst has a higher Pt dispersion when compared to Pt/ZrO_2-8.

Table 3. Average platinum particle size of the catalysts estimated by XRD and TEM.

Catalyst	XRD [a] (nm)	TEM (nm)
Pt/ZrO_2-8	N.D. [b]	1 – 4
Pt/ZrO_2-75	N.D. [b]	N.D. [c]

[a] Average particle size was estimated from Pt(1 1 1) line width.
[b] The diffraction peak from the Pt particles could not be detected.
[c] Pt particles could not be detected in the TEM images.

3.3.2. Oxidation state of Pt in the Pt/ZrO_2 catalysts

Figure 3 shows the XPS spectra of the catalysts at the Pt 4f band. Metallic Pt (Pt^0) has Pt $4f_{7/2}$ and Pt $4f_{5/2}$ bands at 70.7 and 74.0 eV, respectively [10]. In addition, the binding energy of Pt^{2+} and Pt^{4+} is ca. 73.0 and 74.7 eV for $4f_{7/2}$, and 76.4 and 78.1 eV for $4f_{5/2}$, respectively [11]. The peak assigned to Pt^0 $4f_{7/2}$ (70.7 eV) was observed for Pt/ZrO_2-8, while that peak for Pt/ZrO_2-75 almost disappeared. In contrast, the peak assigned to Pt^{4+} $4f_{5/2}$ (78.1 eV) was observed for Pt/ZrO_2-75, but not for Pt/ZrO_2-8. The proportion of Pt^0, Pt^{2+} and Pt^{4+} in the catalysts was quantitatively calculated from the peak fitting of the XPS spectrum (Figure 4). As shown in Figure 4, the main constituent of Pt in Pt/ZrO_2-8 was the Pt^0 species, while the Pt^{2+} and Pt^{4+} species with a high oxidation state were mainly present in Pt/ZrO_2-75.

Furthermore, we examined the state of Pt by IR using CO as the probe molecule.

Figure 5 shows the IR spectra of CO adsorbed at 200°C on Pt. The peaks at around 2070 – 2090 cm^{-1} observed in both Pt/ZrO_2-8 and Pt/ZrO_2-75 are assigned to CO adsorbed on Pt^0 [12]. The peak intensity for Pt/ZrO_2-75 drastically decreased as compared with Pt/ZrO_2-8. This result is in accord with the XPS observation that the proportion of Pt^0 in Pt/ZrO_2-75 is much lower than that in Pt/ZrO_2-8. We have confirmed that the peak area of the IR is proportional to the amount of CO adsorbed on the catalysts. Therefore, the ratio of the peak area in the IR spectrum is equivalent to that of the number of Pt^0 sites. Consequently, it is found that the number of Pt^0 sites for Pt/ZrO_2-8 is about eighteen times greater than that for Pt/ZrO_2-75.

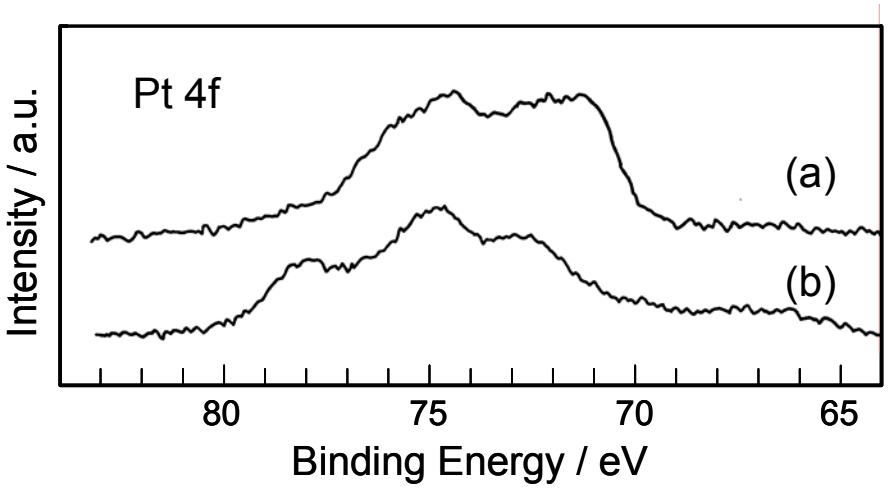

Figure 3. XPS spectra of the catalysts at the Pt 4f bands. (a) Pt/ZrO_2-8, (b) Pt/ZrO_2-75.

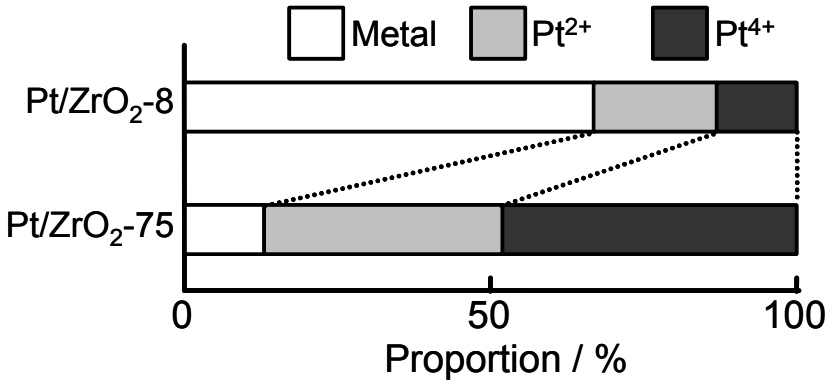

Figure 4. The proportion of Pt^0(metal), Pt^{2+} and Pt^{4+} in the catalysts determined by XPS measurements.

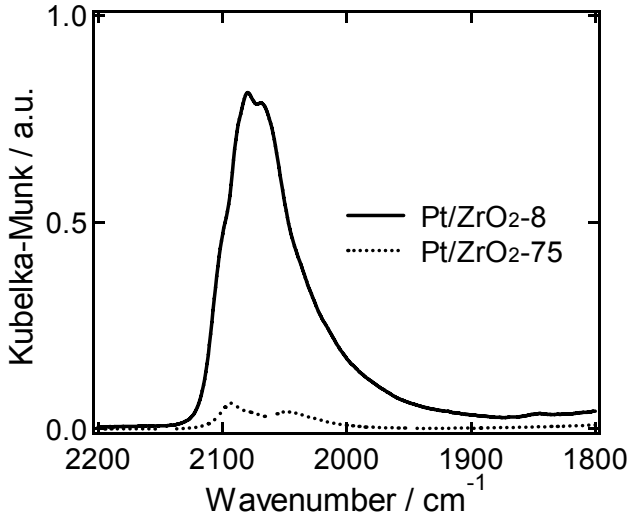

Figure 5. IR spectra of CO adsorbed at 200°C on the catalysts.

3.3.3. Relationship between the basicity of zirconia supports and the oxidation state of Pt

The basicity of the zirconia supports was measured by CO_2-TPD. The CO_2-TPD profiles of ZrO_2-8 and ZrO_2-75 are shown in Figure 6. Broad peaks were observed for ZrO_2-8 and ZrO_2-75, both having the maximum point at about 200°C. However, the

desorption peak area from ZrO_2-75 is larger than that from ZrO_2-8. This indicates that the base strength on these two samples may be the same, but that the base amount on ZrO_2-75 is much more than that on ZrO_2-8. Base amounts measured by CO_2-TPD are listed in Table 4. The base amount per gram sample (BA) of ZrO_2-75 is about eight times greater than that of ZrO_2-8. On the other hand, the base amounts per square meter (base site density) of ZrO_2-8 and ZrO_2-75 have almost same value. Therefore, it is suggested that the high BA of ZrO_2-75 is due mainly to its high surface area.

Yoshida et al. investigated the support effect on the state of the Pt catalysts by XAFS analysis [13]. The Pt on a basic support such as MgO and La_2O_3 is fully oxidized in an oxidative atmosphere, while the Pt on the acidic support contains more metallic Pt. Thus, it could be considered in our system that the extremely high BA of ZrO_2-75 stabilized the high oxidation state of Pt such as Pt^{2+} and Pt^{4+} compared to ZrO_2-8.

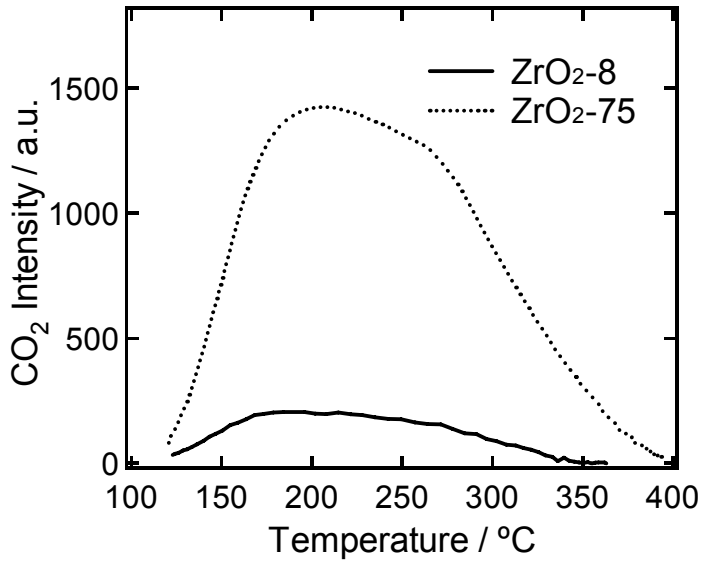

Figure 6. CO_2-TPD profiles of the ZrO_2 supports.

Table 4. Base amounts of the ZrO_2 supports measured by CO_2-TPD.

Sample	Amount of CO_2 desorbed	
	(μmol/g)	(μmol/m^2)
ZrO_2-8	14	1.7
ZrO_2-75	116	1.5

3.4. The cause of the reaction selectivity for n-hexane and SO_2 oxidations

As mentioned above, the Arrhenius parameter measurements indicated that both catalysts have identical active sites for the complete oxidation of *n*-C_6H_{14}, and that the pre-exponential factor on Pt/ZrO_2-8 is one order of magnitude greater than that on Pt/ZrO_2-75. This same trend applies to the oxidation of SO_2. On the other hand, from the IR peak area of adsorbed CO, the number of Pt^0 sites on Pt/ZrO_2-8 is at least ten times greater than that for Pt/ZrO_2-75. The correlation between the pre-exponential factor and the Pt^0 sites indicates that the Pt^0 sites mainly act as active sites for the *n*-C_6H_{14} and SO_2 oxidations. Additionally, it is postulated that the difference in the number of Pt^0 active sites causes the apparent selectivity for the *n*-C_6H_{14} and SO_2 oxidations to change. Since the reaction rate for the SO_2 oxidation is much slower than that for the *n*-C_6H_{14} oxidation, the decrease in the active Pt^0 sites apparently suppresses the SO_2 oxidation compared to the *n*-C_6H_{14} oxidation. Therefore, the cause of the high selectivity for Pt/ZrO_2-75 is the extreme decrease in the active Pt^0 site. Furthermore, in order to verify this hypothesis, we estimated the catalytic activity on the Pt/SiO_2 catalysts with various number of Pt^0 sites (Figure 7). These Pt/SiO_2 catalysts were prepared by modifications of the Pt loading amount and calcination temperatures. In addition, it have been reported that most of the Pt on the SiO_2 support exist in the

metallic state in an oxidative atmosphere [13]. As shown in Figure 7, the SO_2 oxidation is more suppressed by decreasing the active Pt^0 sites than the n-C_6H_{14} oxidation, causing ΔT to widen. From these results, it is clear that the apparent oxidation selectivity between n-C_6H_{14} and SO_2 could be controlled by the number of active Pt^0 sites.

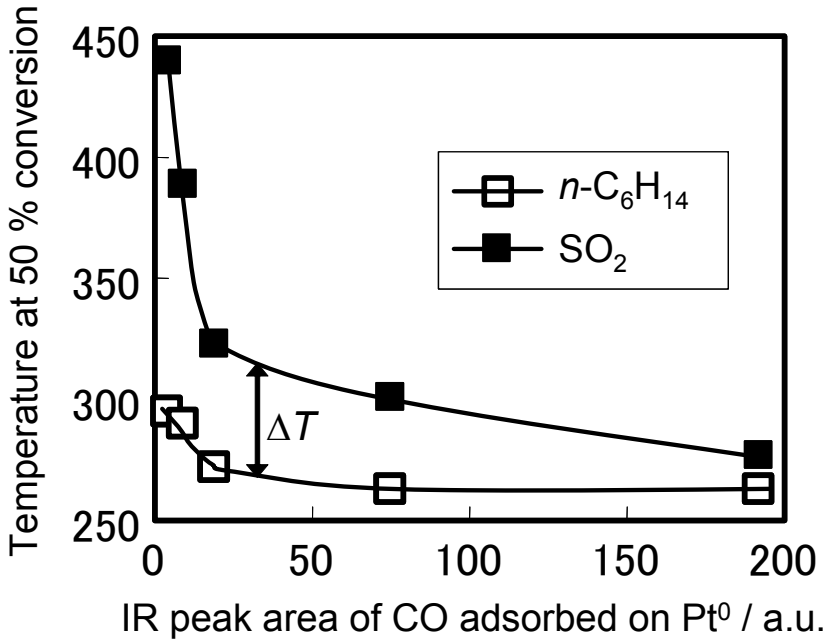

Figure 7. The relation between the conversion of n-C_6H_{14} and SO_2 oxidation and the amount of the Pt^0(metal) site. Pt/SiO_2 catalysts with various amounts of Pt^0 sites were employed. The IR peak area of CO adsorbed on Pt^0 is proportional to the amount of the Pt^0 site. ΔT denotes the temperature difference between the 50 % n-C_6H_{14} and SO_2 conversion efficiencies.

4. CONCLUSIONS

In this study, we estimated the reaction selectivity for the *n*-C_6H_{14} and SO_2 oxidations over two types of Pt/ZrO_2 catalysts with low and high ZrO_2 support surface areas. The Pt/ZrO_2-75 catalyst with a high surface area has a desirably higher selectivity for the complete oxidation of *n*-C_6H_{14} than that of SO_2, as compared with the Pt/ZrO_2-8 catalyst with a low surface area. Namely, the Pt/ZrO_2-75 remarkably suppresses the SO_2 oxidation as compared with the *n*- C_6H_{14} oxidation. In order to clarify the cause of this reaction selectivity, we investigated the Arrhenius parameter for these oxidation reactions and characterized the catalysts using XPS, XRD, TEM, IR and CO_2-TPD methods. The number of Pt^0 (metal) sites in the Pt/ZrO_2-75 was significantly lower than that in the Pt/ZrO_2-8, because the high basicity of the ZrO_2-75 stabilized the high oxidation state of Pt such as Pt^{2+} and Pt^{4+}. Since the reaction rate for the SO_2 oxidation is much slower than that for the *n*-C_6H_{14} oxidation, the decrease in the active Pt^0 site apparently suppresses the SO_2 oxidation as compared with the *n*-C_6H_{14} oxidation. Therefore, the cause of the high selectivity for the Pt/ZrO_2-75 was the extreme decrease in the active Pt^0 sites. It was clarified that the apparent oxidation selectivity between *n*-C_6H_{14} and SO_2 could be controlled by the number of active Pt^0 sites.

ACKNOWLEDGEMENTS

We wish to thank Messrs. K. Doumae (XPS), Y. Matsuoka (TEM), Y. Watanabe and K. Banno for their contributions.

REFERENCES

[1] P. Zelenka, W. Cartellieri, P. Herzog, *Appl. Catal. B* **10** (1996) 3.

[2] R.J. Farrauto, K.E. Voss, *Appl. Catal. B* **10** (1996) 29.

[3] Y. Watanabe, K. Banno, M. Sugiura, *Appl. Clay Sci.* **16** (2000) 59.

[4] W.O. Siegl, R.H. Hammerle, H.M. Herrman, B.W. Wenclawiak, B. Luers-Jongen, *Atmospheric Environment* **33** (1999) 797.

[5] J.K. Lampert, M.S. Kazi, R.J. Farrauto, *Appl. Catal. B* **14** (1997) 211.

[6] T.F. Garetto, C.R. Apesteguía, *Catal. Today* **62** (2000) 189.

[7] L. Kiwi-Minsker, I. Yuranov, E. Slavinskaia, V. Zaikovskii, A. Renken, *Catal. Today* **59** (2000) 61.

[8] T. Maillet, C. Solleau, J. Barbier Jr., D. Duprez, *Appl. Catal. B* **14** (1997) 85.

[9] K. Ruth, M. Hayes, R. Burch, S. Tsubota, M. Haruta, *Appl. Catal. B* **24** (2000) L133.

[10] K.S. Kim, N. Winorgrad, R.E. Davis, *J. Am. Chem. Soc.* **93** (1971) 6296.

[11] F. Grasset, P. Alphonse, C. Labrugère, J. Darriet, A. Rousset, *Mater. Res. Bull.* **34** (1999) 2101.

[12] R.L. Keiski, M. Härkönen, A. Lahti, T. Maunula, A. Savimäki, T. Slotte, *Stud. Surf. Sci. Catal.* **96** (1995) 85.

[13] H. Yoshida, Y. Yazawa, N. Takagi, A. Satsuma, T. Tanaka, S. Yoshida, T. Hattori, *J. Synchrotron Rad.* **6** (1999) 471.

Chapter 5: Sintering inhibition mechanism of Pt supported on ceria-based oxide and Pt-oxide–support Interaction

ABSTRACT

Sintering inhibition mechanism of Pt in Pt/ceria-based oxide catalyst under oxidizing condition at high temperature has been studied by several analysis techniques. Pt in Pt/ceria-based oxide catalyst did not sinter at all after ageing treatment at 800 °C in air, when compared to in Pt/Al_2O_3 catalyst. By using X-ray absorption analysis, we found that the Pt-O-Ce bond, that is, the Pt-oxide-support interaction acts as an anchor and inhibits the sintering of Pt particles on ceria-based oxide. As a result of further systematic investigation on various Pt catalysts, it was clear that there was an excellent correlation between the strength of the Pt-oxide-support interaction and the electron density of oxygen in the support oxide. The sintering inhibition effect on Pt can be controlled by the electron density of oxygen in the support through the Pt-oxide-support interaction.

1. INTRODUCTION

Three-way catalysts (TWCs) can efficiently purify harmful automobile emissions. Since TWCs were commercialized in the USA and Japan in 1977 [1], they have played an important role in environmental protection. Recently, along with growing demands for global environmental protection, more stringent regulations have been imposed on automobile industries. Therefore, automobile companies are making strong efforts to clean up automobile exhaust, and we have to encourage technical innovation for more advanced TWCs.

Basically, the TWC consists of precious metals such as Pt and Rh, supports such as Al_2O_3, and ceria-based oxide as an oxygen storage component [2-4]. The precious metal particles are a few nanometer (nm) in diameter and are dispersed on a support oxide. These precious metals act as the active site to simultaneously purify harmful automotive exhaust such as nitrogen oxides (NOx), carbon monoxide (CO) and unburned hydrocarbons (HC). When the TWC is exposed to high-temperatures of about 800 °C and above, the precious metal will agglomerate and sinter, lowering the active surface area [8-11]. Generally, the sintering of the precious metal particles during operation is considered to cause a decrease in the catalytic activity i.e. degradation. Besides, exhaust conditions from an automotive gasoline engine fluctuate between oxidative and reductive atmospheres during vehicle operation. Specifically, the activity of Pt-supported catalysts significantly decreases after high-temperature ageing in an oxidative atmosphere due to the sintering of Pt particles when compared to in a reductive atmosphere [8, 9]. Therefore, the development of highly durable catalysts without Pt sintering in an oxidative atmosphere is strongly required in automotive industrial research.

Ceria-based oxide is widely utilized for automotive catalysts because of its performances not only to store/release oxygen, but to stabilize precious metal dispersion [2, 5]. Several studies have been conducted on the Pt sintering and Pt-support interaction in Pt/ceria catalysts and significant progress in knowledge has been made. Diwell et al. [6] reported that the formation of Pt-ceria complex under oxidizing condition could maintain Pt stability against sintering. In addition, Murrell et al. [7] showed by using Laser Raman technique that precious metal oxide structure interacts strongly with the ceria surface. However, the nature of Pt-ceria interaction still remains very complicated, and there is room for further investigation.

In this paper we investigated two objects. First one is to understand the sintering inhibition mechanism of Pt particles on ceria-based oxide at the atomic level by using X-ray absorption analysis. Secondly, we conducted further systematic investigation on various Pt catalysts, and we clarified the essence of the Pt-oxide-support interaction and its relation to Pt sintering in an oxidizing atmosphere.

2. EXPERIMENTAL

2.1. Catalysts preparation and ageing treatment

Pt/Al_2O_3 and Pt/ceria-based mixed oxide (Ce-Zr-Y mixed oxide, referred to as CZY) catalysts were prepared by the following methods. Al_2O_3 as a support oxide was supplied by Nikki Universal Co., Ltd.: its crystal structure was γ-type. CZY powders as a support oxide was prepared using a coprecipitation process with aqueous NH_3 using $Ce(NO_3)_3$, $ZrO(NO_3)_2$ and $Y(NO_3)_3$ in aqueous solutions. The precipitate was dried at 110 °C and calcined in air at 700 °C for 3 h. CZY contains 50 wt% CeO_2, 46 wt% ZrO_2 and 4 wt% Y_2O_3, and its crystal structure was cubic. 2 wt% Pt/Al_2O_3 and 2 wt% Pt/CZY catalysts were prepared by the conventional wet impregnation of Al_2O_3 and CZY powders with $Pt(NH_3)_2(NO_2)_2$ aqueous solution. The impregnated powders were dried overnight at 110 °C and calcined at 500 °C for 3 h in air. These samples are referred to as “fresh catalyst”. Portion of the fresh sample were aged in air for 5 h at 800 °C. This ageing treatment corresponds to an accelerated test for durability in an oxidative atmosphere. These samples are referred to as “aged catalyst”. Pt/SiO_2, Pt/ZrO_2, Pt/TiO_2 and Pt/CeO_2 for a systematic study were prepared by the same method as the above, using commercial support oxides. These catalysts were aged in the same way.

The aged Pt/CZY was reduced by 5 % H_2 (N_2 balance) at 400 °C for 30 min. The reduced sample was cooled to room temperature, and then put into a bag with oxygen scavenger to avoid the oxidation. Aged and fresh samples were put into a bag without oxygen scavenger, respectively. The samples in the bag were used for the after-mentioned XAFS experiment.

2.2. Characterization

2.2.1. Adsorption methods

The specific surface areas of the samples were estimated using the N_2 adsorption isotherm at 77 K by the one-point Brunauer-Emmett-Teller (BET) method using an automatic surface analyzer (Micro Sorp 4232II, Micro Data Co., Ltd.). The samples were pretreated in flowing N_2 at 473 K for 20 min. The BET surface areas of the fresh and aged catalysts examined for this study are summarized in Table 1, together with the information on the support.

The average particle size of Pt metal was measured using a CO pulse adsorption method [12]. The catalysts were pre-treated in flowing pure oxygen, and then pure hydrogen at 400 °C. With this reductive treatment of hydrogen, Pt is reduced to Pt metal. CO pulse adsorption was carried out in flowing He at -78 °C. At this temperature, the CO uptake on ceria support was almost entirely suppressed, and CO was adsorbed to only the surface of Pt [13]. The average particle size was calculated from CO uptake assuming that CO was adsorbed on the surface of spherical Pt particles at CO/(surface Pt atom) = 1/1 stoichiometry.

Table 1. The Catalyst samples and BET surface area.

Sample [a]	Pt loading (wt.%)	Support	BET surface area (m^2/g)	
			Fresh catalyst	Aged catalyst [b]
Pt/Al_2O_3	2	γ-Al_2O_3	185	154
Pt/CZY	2	Ce-Zr-Y mixed oxide, Cubic-type, 50 wt% CeO_2-46 wt% ZrO_2-4 wt% Y_2O_3,	99	58
Pt/CeO_2	2	Cubic-type CeO_2	107	81
Pt/SiO_2	2	Amorphous SiO_2	51	47
Pt/ZrO_2	2	Tetragonal + monoclinic-type ZrO_2	87	30
Pt/TiO_2	2	Rutile-type TiO_2	67	34

[a] For sample description, see Experimental.
[b] Fresh samples were aged in air for 5 h at 800 °C.

2.2.2. Structure analysis

Microstructure of the catalysts was investigated by transmission electron microscopy (TEM) using a JEOL JEM-2000EX.

The powder XRD experiments were carried out in air at room temperature using a RINT2000 (Rigaku Co. Ltd.) diffractometer with Cu Kα radiation (1.5406 Å). The catalyst samples were reduced by 5 % H_2 (N_2 balance) at 400 °C for 30 min before the XRD measurement. The catalyst powder were pressed into wafers and affixed to standard-sized microscope slides. The average particle size of Pt was estimated from the Pt(1 1 1) line width using Scherrer's equation with the Gaussian line shape

approximation.

The Pt L_3-edge (11.5 keV) X-ray absorption fine structure (XAFS) measurement was carried out at BL01B1 and BL16B2 of SPring-8 (Hyogo, Japan). The storage ring energy was operated at 8 GeV with a typical current of 100 mA. The XAFS spectra at Pt L_3-edge were measured using a Si (1 1 1) double crystal monochromator in the fluorescence mode at room temperature in air. Data reduction of the XAFS was carried out as described elsewhere [14]. The curve-fitting analysis of the EXAFS spectra was performed for the inverse Fourier transforms on the Pt-oxygen and Pt-cation (cation = Pt, Ce and Zr) shells using theoretical parameters calculated by McKale et al. [20].

The X-ray photoelectron spectroscopy (XPS) measurements were carried out using a PHI model 5500MC with Mg Kα X-rays. The catalyst sample was placed on a grid, and pretreated under 0.5 atm O_2 pressure at 500 °C for 5 min. The pretreated sample was cooled to room temperature and then transferred to the XPS measurement stage without exposure to air atmosphere. The oxygen 1s core electron levels in support oxides were recorded to evaluate the chemical property of the support. Binding energies were calibrated with respect to Pt($4f_{7/2}$) at 71.4 eV.

3. RESULTS AND DISCUSSION

3.1. Sintering of Pt particles in Pt/Al_2O_3 and Pt/CZY catalysts

First of all, the Pt sintering behavior in Pt/Al_2O_3 and Pt/CZY catalysts were investigated. Figure 1 shows the transmission electron microscopy (TEM) images of the Pt/Al_2O_3 and Pt/CZY catalyst after ageing treatment at 800 °C in air for 5h. In the aged Pt/Al_2O_3, large Pt particles ranging from 3 to 150 nm could be observed. On the other hand, no explicit Pt particles were observed on the aged Pt/CZY. In the aged Pt/CZY, Pt could be detected by energy dispersive X-ray (EDX) analysis. This indicates that Pt particles are highly dispersed on the CZY support.

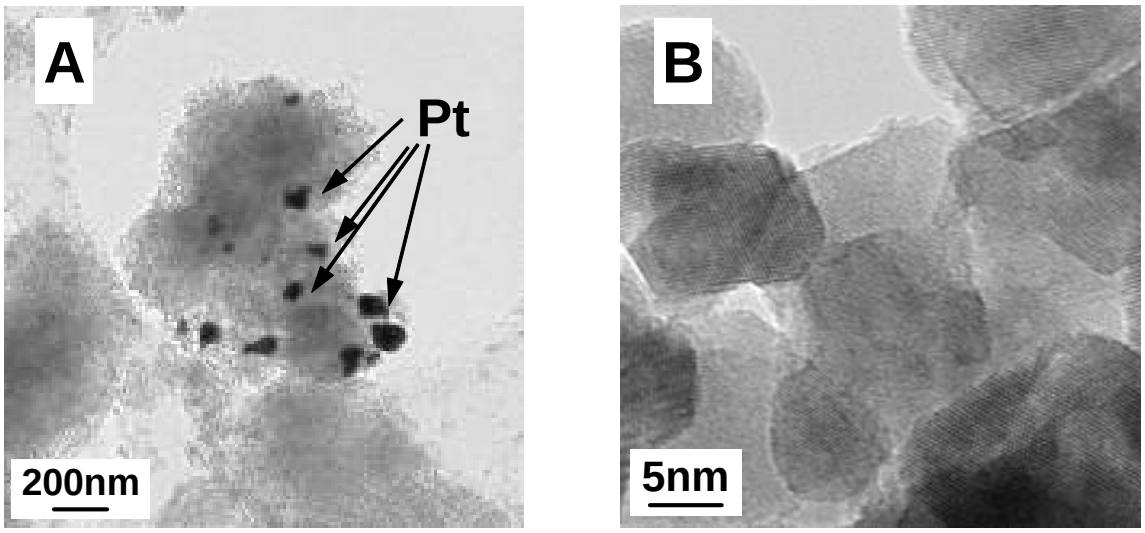

Figure 1. TEM images of Pt supported catalysts after 800 °C ageing in air for 5h. (A) Pt/Al_2O_3 catalyst. (B) Pt/CZY (CZY denotes Ce-Zr-Y mixed oxide, see experimental) catalyst.

The average size of Pt metal particles for these catalysts was determined by XRD and CO pulse method (Table 2). The diffraction peaks from the Pt particles in both fresh Pt/Al_2O_3 and Pt/CZY could not be detected by XRD due to their small particle size. Pt particles size on the Al_2O_3 support before the ageing treatment, which was estimated by

the CO pulse method, was almost the same as that on CZY. The size was about 1 nm in diameter. On the contrary, this situation changed completely after the ageing. Pt particles in the Pt/Al_2O_3 grew up to large particles during the ageing treatment. The Pt particle size in the aged Pt/Al_2O_3 determined by the XRD and CO pulse method was 61 and 23.6 nm, respectively. On the other hand, Pt particles in the Pt/CZY could not be observed by XRD even after the ageing, suggesting that the Pt particles on CZY support continued to be highly dispersed. The Pt particle size of 1.1 nm in the aged Pt/CZY estimated by CO pulse was the same as that in the fresh catalyst. This indicates that Pt in Pt/CZY catalyst did not sinter at all after the ageing treatment.

Table 2. Average platinum particle size of the catalysts estimated by XRD and CO pulse adsorption method.

Sample		Average Pt particle size (nm)	
		XRD [a]	CO pulse
Pt/Al_2O_3	Fresh	ND [b]	1.0
	Aged	61	23.6
Pt/CZY	Fresh	ND [b]	1.1
	Aged	ND [b]	1.1

[a] Average particle size was estimated from Pt(1 1 1) line width.
[b] The diffraction peak from the Pt particles could not be detected.

3.2. XAFS analysis of Pt/Al_2O_3 and Pt/CZY catalysts after ageing

In order to clarify the cause of the sintering inhibition of Pt in Pt/CZY, the state of Pt atoms supported on Al_2O_3 or CZY was investigated using XAFS analysis. Generally, the XAFS spectra can be divided into two spectral regions: the X-ray absorption near edge structure (XANES) and the extended X-ray absorption fine structure (EXAFS)

regions. We can get information on the electronic state from XANES analysis [15] and the local structure around a target element from EXAFS analysis [16].

3.2.1. Pt L_3-edge XANES spectra

Figure 2 shows the XANES spectra at Pt L_3-edge for the aged catalysts and reference samples. The steeply rising absorption edge is referred to as “white line”. In the case of the Pt L-edge XANES, the absorption intensity of the white line reflects on the vacancy in the 5d orbital of Pt atoms [15]. Large white line is observed on oxidized Pt, while small white line is observed on reduced Pt. Therefore, it is possible to estimate the average oxidation state of the Pt atoms in each sample. The white line intensity of Pt/Al_2O_3 was the same as that of Pt foil. It suggests that Pt on Al_2O_3 is in the Pt^0 (metal) state after the ageing. In contrast, the white line intensity of Pt/CZY was similar to that of PtO_2, suggesting that the Pt^{2+} and Pt^{4+} species with a high oxidation state are mainly present in the aged Pt/CZY. The average oxidation state of Pt can be quantitatively evaluated from the white line intensity [22]. There is a linear relationship between the while line intensity and the oxidation state of PtOx on some metal oxide supports. On the basis of this linear relationship, the estimated oxidation state of Pt in the aged Pt/Al_2O_3 and the aged Pt/CZY was 0 and 3.53, respectively.

Generally, it is well known that PtO_2 decomposes to Pt metal under oxidizing conditions at around 600 °C and above according to the thermodynamic phase diagram [17]. The result that Pt on Al_2O_3 was in the Pt^0 state after 800 °C ageing in the oxidizing atmosphere was consistent with the thermodynamics. On the other hand, the CZY support could stabilize a high-oxidation state of Pt even after the ageing. Thus, it is suggested that the strong Pt-support interaction in the Pt/CZY under the oxidizing

condition causes the stabilization of high-oxidation state of Pt.

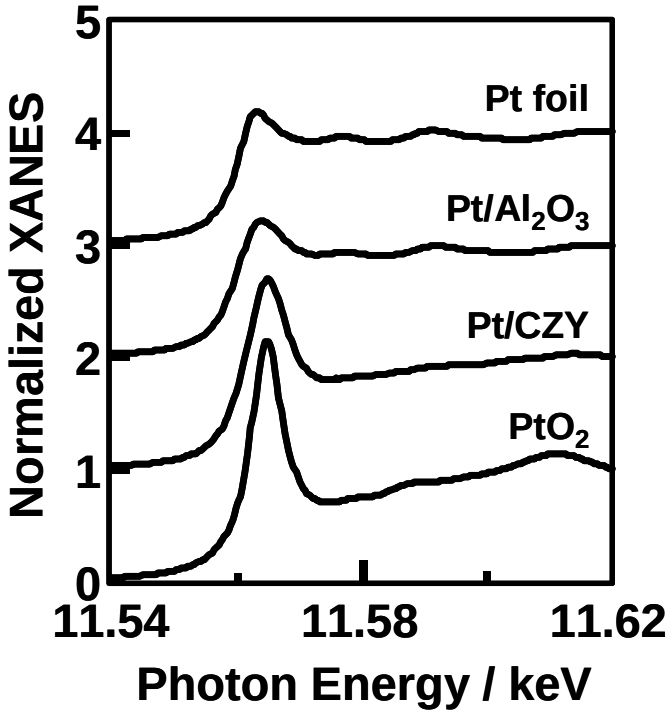

Figure 2. Pt L_3-edge XANES spectra for supported Pt catalysts after 800 °C ageing in air, together with standard samples of Pt foil and PtO_2 powder.

3.2.2. Fourier transforms (FTs) of Pt L_3-edge EXAFS spectra

Fourier transforms (FTs) of the aged catalysts and reference samples are presented in Figure 3. The FTs were performed on the Pt L_3-edge EXAFS spectra in about 3.0–16$Å^{-1}$ region. The quantitative curve-fitting analysis of the EXAFS spectra was performed for the inverse FTs on the Pt–oxygen and Pt-cation (cation = Pt, Ce and Zr) shells, respectively. The results of curve-fitting analysis are summarized in Tables 3. The FTs are not corrected for phase shift. Therefore the peaks in the FTs are shifted to lower *R* values. The values of bond length in the text and table are corrected for phase shift. In the FT spectrum of Pt foil, the peak at 2.76 Å is assigned to the Pt-Pt bond. In

the FT of PtO_2 powder, the peaks at 2.04 and 3.10 Å are assigned to the Pt-O and Pt-O-Pt bonds, respectively. The FT of the Pt/Al_2O_3 after the ageing was obviously different from that of the Pt/CZY. As for the aged Pt/Al_2O_3, only the intense peak at 2.76 Å, which corresponds to the Pt-Pt bond, was observed. The FT spectrum of the Pt/Al_2O_3 was coincided with that of Pt foil. The coordination number (CN) of the Pt-Pt shell in the aged Pt/Al_2O_3 was 11.5. This indicates that the Pt metal particles on Al_2O_3 after the ageing are at least 20 nm in size [18]. In the Pt/CZY after the ageing, the FT spectrum was different from those of both Pt foil and PtO_2 powder. The position of the first peak at 2.02 Å in the Pt/CZY was close to that of PtO_2, and this peak was fitted with the Pt-O bond. It should be noted that the second evident peak, which was absent in both Pt foil and PtO_2 powder, was found at 3.01 Å. A curve-fitting simulation of this second peak was carefully made. Figure 4 shows the results of curve-fitting analysis on the second peak of the Pt/CZY on the supposition that the second neighboring atom is Ce or Pt. An excellent fitting result for the simulation of Ce atom could be obtained. On the other hand, in the case of Pt, an appropriate fit could not be obtained, because the EXAFS oscillation pattern of Pt was very different from that of the experimental data. It is clear that the second neighboring atom in the aged Pt/CZY is Ce atom, not Pt one. Curve-fitting analysis for the simulation of other cation such as Zr and Y was also conducted in order to investigate the second neighboring atom in the aged Pt/CZY, but an appropriate fit for Ce when compared to Zr(Y) could not be obtained. These results lead to the conclusion that Pt atoms strongly interact with the CZY support during the ageing and form Pt-O-Ce bond. The value of CN of Pt-Ce shell in the aged Pt/CZY was 3.5. This coordination number of 3.5 is lower than 12 which is the saturated coordination number in cubic fluorite structure. This indicates that Pt ions exist on the

surface of CZY support. In addition, intense Pt-Pt or Pt-O-Pt peaks could not be observed in the aged Pt/CZY, suggesting that there are no large Pt metal or oxide particles on the CZY. In other words, highly dispersed Pt oxides are present on the surface of CZY support.

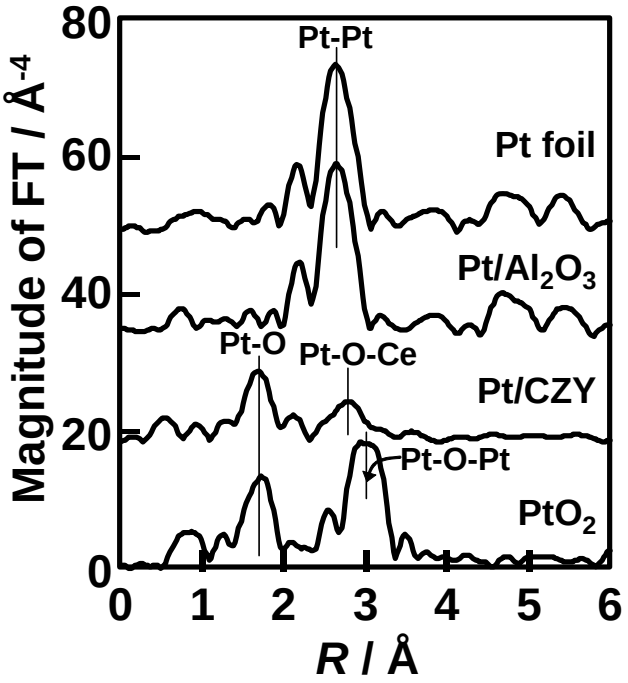

Figure 3. Fourier-transformed k^3x data of Pt L_3-edge EXAFS for supported Pt catalysts after 800 °C ageing in air and the standard samples of Pt foil and PtO_2 powder.

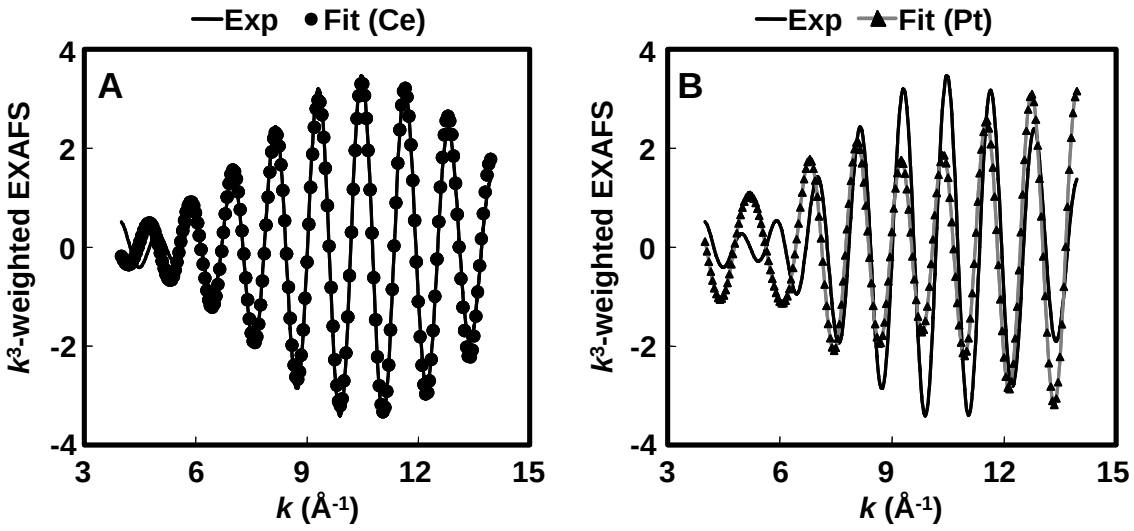

Figure 4. The results of curve-fitting analysis on the inverse Fourier-transform of the second peak on the aged Pt/CZY catalyst in Figure 3 and the corresponding curve-fit. (A) Experimental (—) and curve-fit on Ce atom (●). (B) Experimental (—) and curve-fit on Pt atom (··▲··).

Table 3. Results of curve-fitting analysis for the aged catalysts and standard samples.

Sample	Shell	CN	*R* (Å)	σ^2 (Å^2)
Pt foil [a]	Pt-Pt	12.0	2.76	0.0045
Pt/Al_2O_3	Pt-Pt	11.5	2.76	0.0046
Pt/CZY	Pt-O	4.1	2.02	0.0007
	Pt-Ce	3.5	3.01	0.0037
PtO_2 [a]	Pt-O	5.7	2.04	0.0026
	Pt-Pt	5.3	3.10	0.0019

[a] The curve-fitting analysis for the standard samples were performed by reference to [23, 24].

A similar Pt-O surface complex on CeO_2 has been reported by Murrell et al. [7]. Murrell et al. reported the following: ”using Laser Raman Spectroscopy, a strong

Raman band at ca. 700 cm^{-1} was observed for Rh, Ir, Pd, and Pt dispersed on CeO_2. This Raman band was assigned to a surface oxide metal-O formed on the CeO_2 surface. Metal oxides on CeO_2 exhibit a Strong Oxide-Support Interaction (SOSI).” Our results by XAFS analysis could give the direct evidence for the formation of Pt-O-Ce bond on the surface of ceria-based oxide support. Moreover, we showed that this Pt-oxide support interaction on CZY surface is stronger than that on Al_2O_3 surface.

Generally, it is considered that Pt^0 (metal) is the active site for the catalytic reaction in automotive exhaust condition. The CZY support could stabilize a high-oxidation state of Pt after the ageing. Therefore, Pt on CZY support has to be reducible during the catalytic reaction. Figure 5 gives the FTs of the aged Pt/CZY, which is the same spectrum mentioned in Figure 3, and the reduced Pt/CZY after ageing. The aged Pt/CZY was reduced by 5 % H_2 at 400 °C. After the reductive treatment, the Pt-O peak in the aged Pt/CZY decreased significantly, and the Pt-O-Ce peak almost disappeared. In addition, intense Pt-Pt could not be observed in the reduced Pt/CZY. From these results, it is suggested that the Pt-O-Ce bond breaks by the reductive treatment, and that Pt metal particles are highly dispersed on the CZY support. According to the results of CO pulse method mentioned above, the average size of Pt metal particles in the reduced Pt/CZY after the ageing is estimated at about 1 nm.

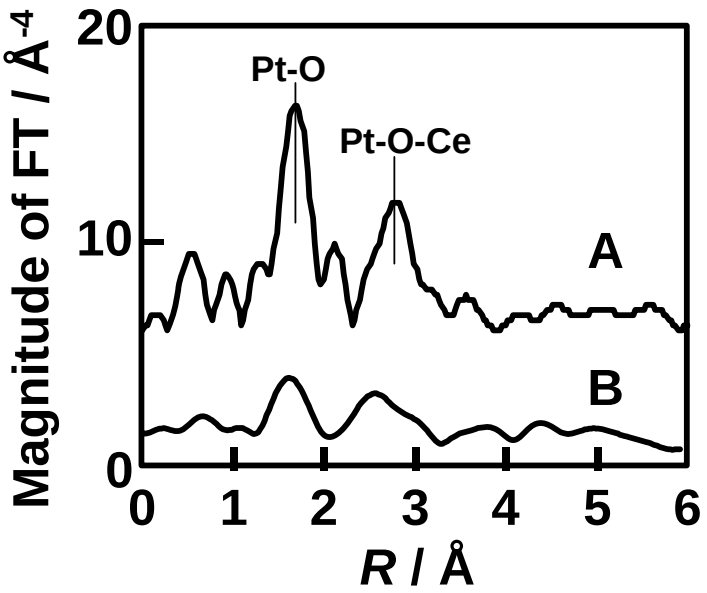

Figure 5. Fourier-transformed k^3x data of Pt L_3-edge EXAFS for (A) Pt/CZY after 800 °C ageing in air and (B) reduced Pt/CZY after ageing.

3.3. Pt Sintering inhibition mechanism

Based on our observation above, we proposed the sintering inhibition mechanism of Pt supported on CZY as shown in Figure 6. In the case of Pt/Al_2O_3, since the interaction between Pt and Al_2O_3 is weak, Pt particles transport across the surface of the Al_2O_3 support and sinter during an 800 °C ageing treatment in an oxidizing atmosphere according to the molecular migration model [9, 19, 21]. In contrast, Pt supported on CZY has a strong interaction with the CZY support. Therefore the CZY support stabilizes a high-oxidation state of Pt, and then the formation of the rigid Pt-O-Ce bond acts as an anchor. The formation of the Pt-O-Ce bond on the CZY suppressed the sintering of Pt. It is considered that the highly dispersed Pt oxide on the surface of CZY support under oxidizing condition are more stable since the Pt-O-Ce bond energies are greater than the Pt-Pt bond energies in large Pt crystallites. On the other hand, during catalytic reaction under stoichiometric or reducing conditions, the Pt-O-Ce bond on the

CZY breaks, and Pt metal particles are highly dispersed on the support.

It is well known that the sintering of supported metal occurs not only via the foregoing metal migration, but also decreases in support surface area during ageing treatment [9, 19, 21]. The surface areas of the fresh and aged Pt/Al_2O_3 were 185 and 154 m^2/g, respectively (Table 1). In contrast, the surface area of Pt/CZY decreased from 99 to 58 m^2/g as shown in Table 1. The ageing treatment resulted in a 40% decrease in the surface area of Pt/CZY. Although the Al_2O_3 support has a high thermal stability when compared to the CZY support, Pt particles on the Al_2O_3 support sintered significantly. Therefore, the Pt sintering was mainly caused by Pt migration, not by decreases in surface area of supports. As for the sintering inhibition mechanism, the Pt-O-Ce bond, that is, the Pt-oxide-support interaction inhibits Pt migration, and this point is the main reason why Pt supported on CZY does not sinter during the high-temperature ageing in oxidative atmosphere.

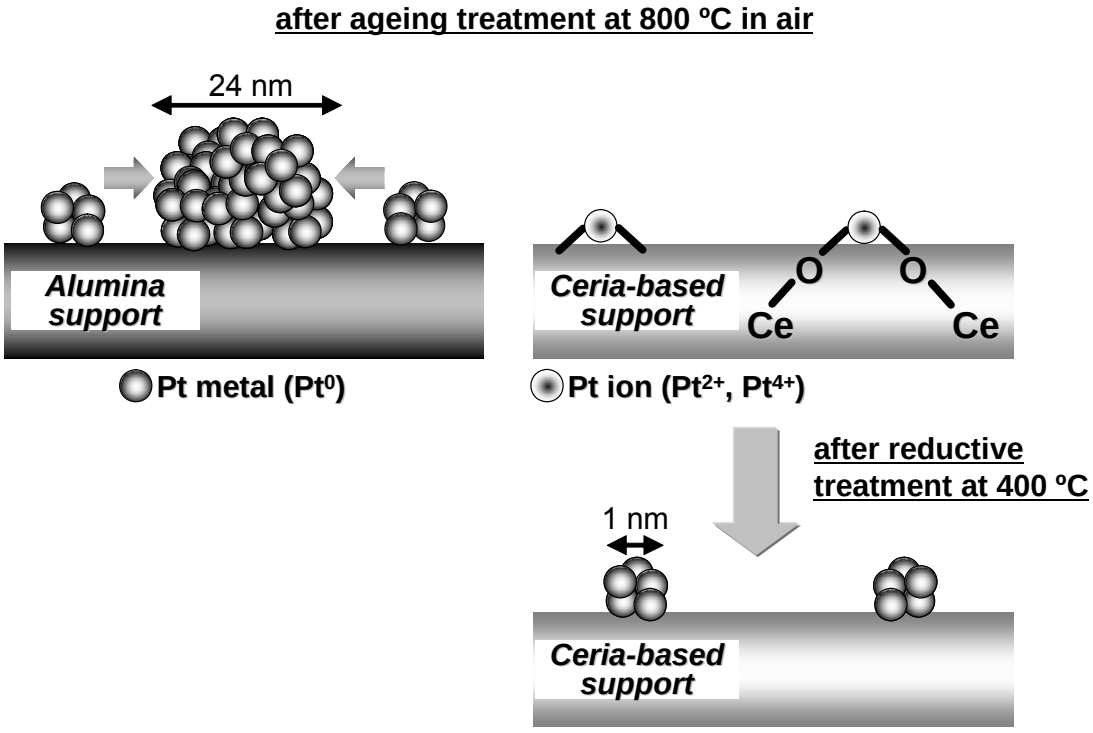

Figure 6. Model illustration of the Pt sintering inhibition mechanism for a Pt/ceria-based catalyst and a conventional Pt/Al_2O_3 catalyst. Since the Pt- Al_2O_3 interaction is weak, Pt metal particles are formed and sintered during 800 °C ageing treatment in air. In contrast, Pt supported on CZY has a strong interaction with CZY support. The generation of Pt-O-Ce bond prevents Pt particles from sintering during the ageing treatment. After the reductive treatment, the Pt-O-Ce bond on the CZY breaks, and Pt metal particles are highly dispersed on the support. The average size of Pt metal particles was estimated by a CO pulse adsorption method.

3.4. Inhibition effect of Pt sintering and Pt-oxide-support interaction

Finally we investigated the essence of the Pt-oxide-support interaction and its relation to Pt sintering in an oxidizing atmosphere. We tried to consider "on what property of the support does the strength of Pt-oxide-support interaction depend?" As has been pointed out, the Pt-O-M (M: cation in the support) bond was the key for the Pt-oxide-support interaction. Therefore, it is reasonable to suppose that the electron density of oxygen in the support oxide predominantly influences the strength of the Pt-O-M bond. As a result, it is expected that the electron density of oxygen in the

support would control the sintering of supported Pt particles. In order to verify this hypothesis, we conducted a systematic investigation on various Pt supported catalysts such as Pt/SiO_2, Pt/TiO_2 and so on. Specifically, we quantified the following three properties for various catalysts: the electron density of oxygen in the support, the strength of the Pt-oxide-support interaction and the sintering inhibition effect on Pt. Besides, the correlation between these properties was investigated. Firstly, regarding the electron density of oxygen in the support, the binding energy of the O(1s) electron in the support oxide was measured by XPS analysis. XPS spectra of the O(1s) core level region in the supports are given in Figure 7. Significant changes could be observed in the spectra. The binding energy of the O(1s) electron decreases in the order of SiO_2, Al_2O_3, ZrO_2, TiO_2, CeO_2 and CZY. Second, concerning the quantification of the strength of the Pt-oxide-support interaction, we investigated the white line intensity in the Pt L_3-edge XANES spectra after the ageing test in the same way as the Pt/Al_2O_3 and Pt/CZY catalysts. As mentioned above, Pt oxide decomposes to Pt metal under oxidizing conditions at around 600 °C and above. The strong Pt-oxide-support interaction stabilizes the high-oxidation state of Pt through the generation of the Pt-O-M bond after 800 °C ageing in an oxidizing atmosphere. Accordingly, it is reasonable to expect that the average oxidation state of Pt after ageing would correspond to the strength of the Pt-oxide-support interaction. The average oxidation state of Pt can be quantitatively evaluated from the white line intensity in the same way as the Pt/Al_2O_3 and Pt/CZY catalysts. Third, as to the sintering inhibition effect on Pt, we measured the average Pt particle size after the ageing at 800 °C in an oxidizing atmosphere. The average size of the Pt metal particles is estimated using the CO pulse method. Figure 8 shows the correlation between these three factors on the various supported Pt catalysts.

It is clear that these three factors have excellent correlation with each other. The oxidation state of Pt after ageing increased with the decreasing binding energy of the O(1s) electron. This indicates that Pt-oxide-support interaction strengthens as the electron density of oxygen of support oxide increases. Subsequently, Pt particle size after the ageing decreased as the electron density of oxygen in the support increased. As a result, the sintering inhibition effect on Pt can be controlled by the electron density of oxygen in the support oxide through the Pt-oxide-support interaction. That is the essence of the Pt-oxide-support interaction and its relation to Pt sintering in oxidizing atmosphere.

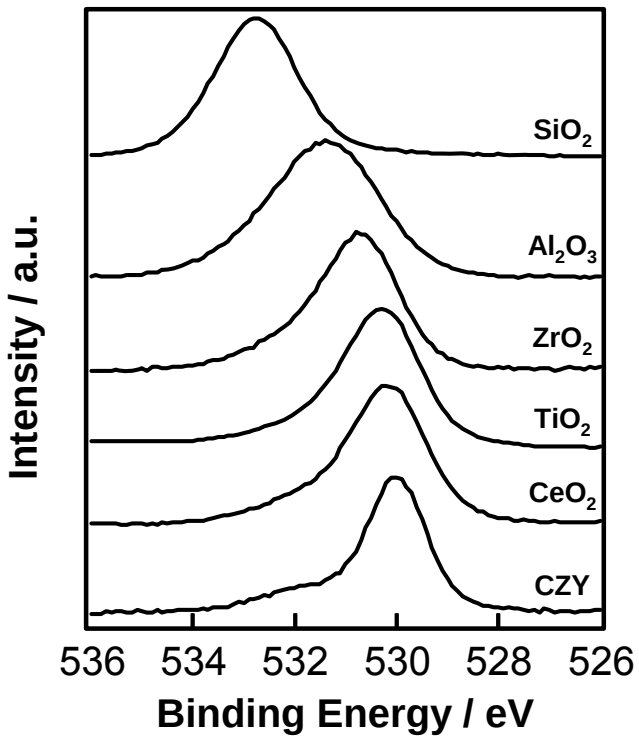

Figure 7. XPS spectra of the O(1s) core level region in the supports.

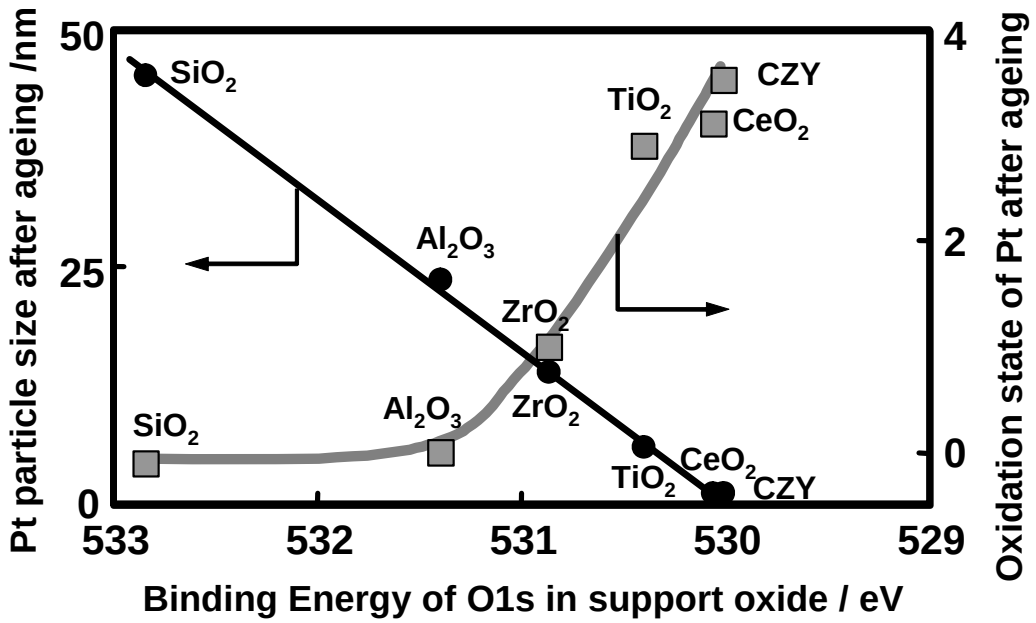

Figure 8. Pt-oxide-support interaction and its relation to Pt sintering in an oxidizing atmosphere. The binding energy of the O(1s) electron in support oxide was measured by XPS analysis. The oxidation state of Pt after ageing was quantitatively evaluated from the white line intensity of the Pt L_3-edge XANES spectra. Pt particle size after ageing was estimated by the CO pulse method.

4. CONCLUSIONS

First, using TEM, XRD and CO pulse method, this study presented that Pt supported on ceria-based oxide (CZY) did not sinter under oxidizing condition at 800 °C while Pt atoms on Al_2O_3 sinter significantly. Pt particles in the Pt/Al_2O_3 grew up to 23.6 nm (by CO pulse method) during the ageing treatment. On the other hand, Pt particles in the Pt/CZY after the ageing continued to be highly dispersed with a diameter of about 1 nm.

Second, we clarified that the sintering inhibition mechanism of Pt particles on CZY at the atomic level by using XAFS analysis. Pt supported on CZY had a strong interaction with the CZY support. Therefore the CZY support stabilized high-oxidation state of Pt under oxidizing condition at high-temperature, and then the rigid Pt-O-Ce bond, that is, the Pt-oxide-support interaction generated. The Pt-O-Ce bond acted as an anchor, and inhibited Pt migration.

Finally, this report clearly showed the relationship between the inhibition effect of Pt sintering and Pt-oxide-support interaction. We conducted a systematic investigation on various Pt supported catalysts and quantified the physical and chemical properties of various catalysts. There was an excellent correlation between the strength of the Pt-oxide-support interaction and the electron density of oxygen in the support oxide. Consequently, it was clear that the sintering inhibition effect on Pt can be controlled by the electron density of oxygen in the support through the Pt-oxide-support interaction.

Due to the advanced analysis techniques such as synchrotron radiation based analysis, the approach to catalytic design for practical use would transit from trial-and-error to planned design and control. We hope that our report can lead the way for the planed catalytic design.

ACKNOWLEDGEMENTS

The X-ray absorption experiments were performed at the SPring-8 with the approval of the Japan Synchrotron Radiation Research Institute (JASRI). We greatly thank Dr. Uruga and Dr. Tanida at SPring-8 for the X-ray measurements.

REFERENCES

[1] S. Matsumoto, *Catal. Today* **90**, (2004) 183.

[2] H.C. Yao, Y.F. Yao, *J. Catal.* **86** (1984) 254.

[3] M. Ozawa, M. Kimura, A. Isogai, *J. Alloys Comp.* **193** (1993) 73.

[4] Y. Nagai, T. Yamamoto, T. Tanaka, S. Yoshida, T. Nonaka, T. Okamoto, A. Suda, M. Sugiura, *Catal. Today* **74** (2002) 225.

[5] E.C. Su, W.G. Rothschild, *J. Catal.* **99** (1984) 506.

[6] A.F. Diwell, R.R. Rajaram, H.A. Shaw, T.J. Truex, *Stud. Surf. Sci. Catal.* **71** (2001) 139.

[7] L.L. Murrell, S.J. Tauster, D.R. Anderson, *Stud. Surf. Sci. Catal.* **71** (2001) 275.

[8] P. J. F. Harris, *J. Catal.* **97** (1986) 527.

[9] R. M. J. Fiedorow, B. S. Chahar, S. E. Wanke, *J. Catal.* **51** (1978) 193.

[10] C. H. Bartholomew, *Appl. Catal. A* **212** (2001) 17.

[11] H. Birgersson, L. Eriksson, M. Boutonnet, S. G. Järås, *Appl. Catal. B* **54** (2004) 193.

[12] T. Uchijima, *Catalytic Science and Technology* (Kodansha-VCH, Weinheim, 1990)

[13] A. Holmgren, B. Andersson, D. Duprez, *Appl. Catal. B* **22** (1999) 215.

[14] T. Tanaka, H. Yamashita, R. Tsutitani, T. Funabiki and S. Yoshida, *J. Chem. Soc., Farad. Trans.* **84** (1988) 2987.

[15] A. N. Mansour, J. W. Cook, D. E. Sayers, *J. Phys. Chem. A* **88** (1984) 2330.

[16] B. K. Teo, EXAFS: *Basic Principles and Data Analysis* (Springer-Verlag, Berlin, 1986).

[17] S. E. Livingstone, *Pergamon Text in Inorganic Chemistry* **25** (1973).

[18] R. B. Greegor, F. W. Lytle, *J. Catal.* **63** (1980) 476.

[19] R. M. J. Fiedorow, S. E. Wanke, *J. Catal.* **43** (1976) 34.

[20] A. G. McKale, B. W. Veal, A. P. Paulikas, S. K. Chan, G. S. Knapp, *J. Am. Chem. Soc.* **110** (1988) 3763.

[21] P. Forzatti, L. Lietti, *Catal. Today* **52** (1999) 165.

[22] H. Yoshida, S. Nonoyama, Y. Yazawa, T. Hattori, *Physica Scripta* **T115** (2005) 813.

[23] M. Vaarkamp, *Catal. Today* **39** (1998) 271.

[24] A. F. Lee, K.Wilson, R. M. Lambert, C. P. Hubbard, R. G. Hurley, R. W. McCabe, H. S. Gandhi, *J. Catal.* **184** (1999) 491

Chapter 6: Real-time observation of platinum redispersion on ceria-based oxide by in-situ turbo-XAS

ABSTRACT

A real-time observation of the redispersion behavior of sintered Pt on ceria-based oxide was made possible by in-situ time-resolved Turbo-XAS in fluorescence mode. 2 wt% Pt/Ce-Zr-Y mixed oxide samples were prepared, and then treated under an aging condition. The average Pt particle size measured by CO absorption method after aging was 7 nm. Redispersion treatments of the previously aged catalyst were carried out at 600 °C within an in-situ XAS cell in a flow of reducing/oxidizing gases cyclically. Pt L_3-edge XANES spectra were collected every 1.1 second under in-situ condition. From a change in the XANES spectra, we observed that the Pt particle size of the aged catalyst decreased from 7 to 5 nm after 60 seconds and then to 3 nm after 1000 seconds. High temperature of 500 °C and above, high concentration of oxygen and strong Pt-oxide-support interaction are required to produce the redispersion of the aged catalyst.

1. INTRODUCTION

Automotive three-way catalysts (TWCs) can efficiently purify harmful automobile emissions. Ever since TWCs were commercialized in the U.S. and Japan in 1977 [1], they have played an important role in the purification of automobile emissions and have improved in performance in concert with growing demands for global environmental protection.

Basically, a TWC consists of precious metals such as Pt and Rh, supports such as Al_2O_3, and some additives. These precious metals act as the active site to simultaneously purify harmful automotive exhaust such as nitrogen oxides (NOx), carbon monoxide (CO), and unburned hydrocarbons (HC). When the TWC is exposed to high temperatures, the precious metal agglomerates and sinters, decreasing the active surface area [2-4]. The sintering of the precious metal particles during operation causes a decrease in catalytic activity (i.e., degradation). Pt particles supported on ceria-based oxide does not sinter under oxidizing condition at 800 °C while Pt atoms on Al_2O_3 sinter significantly in the preceding chapter. However, even Pt/ceria-based oxide catalyst would sinter at higher temperature. Figure 1 shows average Pt particle size for aged Pt/ceria-based oxide catalysts at various temperatures under lean condition. Pt particle size was measured by CO pulse adsorption method. The Pt particle size increased with increasing ageing temperature, especially, the significant sintering of Pt particles could be observed at high temperature of 900 °C and above. Recently, along with growing demands for high-power engine, exhaust gas temperature is getting higher and higher. Therefore, more stringent thermal resistance of catalysts has been required.

Moreover, exhaust conditions from an automotive gasoline engine fluctuate between oxidative and reductive atmospheres during vehicle operation. Therefore, in-situ dynamic observation on the sintering and redispersion phenomena of the precious metal in the automotive catalysts is important for the development of advanced

catalysts. In this report, we present the real-time observation of the redispersion of Pt supported on ceria-based oxide catalysts.

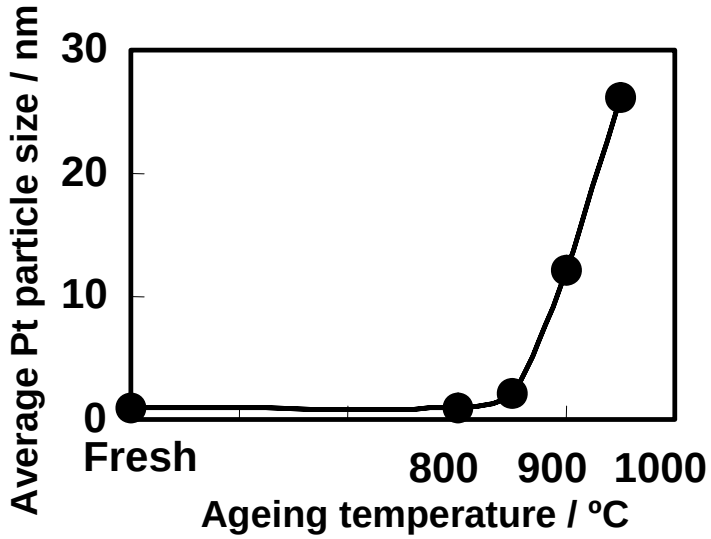

Figure 1. Average Pt particle size for aged Pt/ceria-based oxide catalysts at various temperatures under lean condition.

2. EXPERIMENTAL

2.1. Catalysts preparation and ageing treatment

Ce-Zr-Y mixed oxide (referred to as CZY) powder as a support oxide was prepared using a coprecipitation process with aqueous NH_3 using $Ce(NO_3)_3$, $ZrO(NO_3)_2$, and $Y(NO_3)_3$ in aqueous solutions. The precipitate was dried at 110 °C and calcined in air at 700 °C for 3 h. CZY contains 50 wt% CeO_2, 46 wt% ZrO_2, and 4 wt% Y_2O_3, and its crystal structure by XRD method is cubic. 2 wt% Pt/CZY catalysts were prepared by the conventional wet impregnation of CZY powders with $Pt(NH_3)_2(NO_2)_2$ aqueous solution. The catalyst powders were aged in 3% CO in He at various temperatures in order to obtain specifically sized particles of sintered platinum.

2.2. CO pulse adsorption method

The average particle size of Pt metal was measured using a CO pulse adsorption method [12]. The catalysts were pre-treated in flowing pure oxygen, and then pure hydrogen at 400 °C. With this reductive treatment of hydrogen, Pt is reduced to Pt metal. CO pulse adsorption was carried out in flowing He at -78 °C. At this temperature, the CO uptake on ceria support was almost entirely suppressed, and CO was adsorbed to only the surface of Pt [13]. The average particle size was calculated from CO uptake assuming that CO was adsorbed on the surface of spherical Pt particles at CO/(surface Pt atom) = 1/1 stoichiometry.

2.3. XAFS measurement

A real-time observation of the redispersion behavior of preliminary sintered Pt was made possible by in-situ time-resolved Turbo-XAS (T-XAS) in fluorescence mode

at ID-24 (ESRF) [5]. Figure 2 shows the experimental set-up for the T-XAS measurement. In T-XAS, a narrow slit is scanned through the polychromatic fan of radiation downstream of the crystal, selecting a monochromatic beam. Incoming X-rays (I_0) and fluorescence X-rays (I) are simultaneously recorded by two detectors. The sample is placed in an in-situ cell equipped with a rapid gas switching system, allowing to alternate the gas flow over the sample from an oxidative to reductive atmosphere. The cell was specially designed for fluorescence XAS detection at high sample temperatures (T_{max} ~ 800 °C), while minimizing dead volume. Throughout the redispersion experiment, the pellet samples were heated to 500 - 700 °C before alternately introducing 3 - 20% O_2 in He (oxidizing) and 3% H_2 in He (reducing) every 60 seconds. Pt L_3-edge XAS spectra were collected every about 1.1 second.

2.4. Transmission electron micrograph (TEM)

TEM images were obtained using a JEOL JEM-2000EX. The accelerating voltage was 200 keV. The samples used for the measurement were pretreated at 400°C in 5 %H_2/N_2 for 30 min.

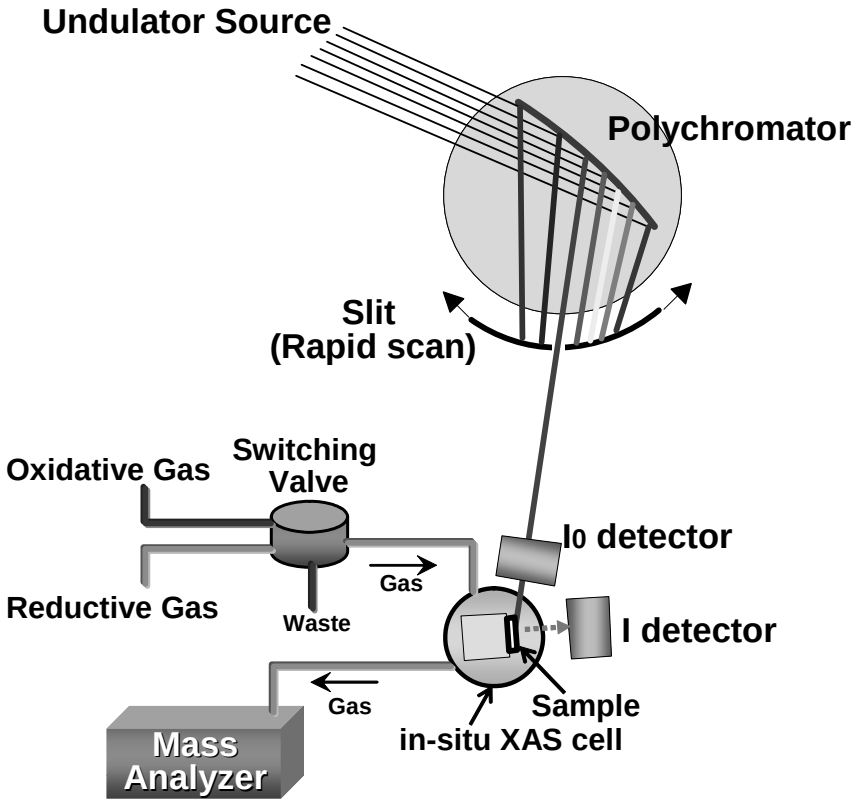

Figure 2. Experimental set-up for in-situ time-resolved Turbo-XAS in fluorescence mode at ID-24 (ESRF).

3. RESULTS AND DISCUSSION

3.1. Comparison of the transmission and fluorescence methods

To test the feasibility of dispersive XAS at the Pt L_3-edge on our Pt/CZY catalysts, we first carried out measurements in air and at room temperature, using both the conventional transmission method as well as Turbo-XAS in the fluorescence mode. Figure 3 shows the comparison of raw XANES spectra at Pt L_3-edge in transmission mode and in fluorescence mode. Transmission data is seen to be very noisy, and the baseline is not flat, making quantitative analysis very difficult. High loading amount of heavy elements such as Ce and Zr in this sample strongly absorbs the X-ray, reducing the optimal thickness of the pellet. The low quality of this data is mainly to be attributed to strong X-ray absorption and thickness inhomogenity of the sample. In contrast, a reasonable quality data could be collected using T-XAS in fluorescence mode. Fluorescence T-XAS therefore permits time-resolved measurements on Pt/CZY catalysts.

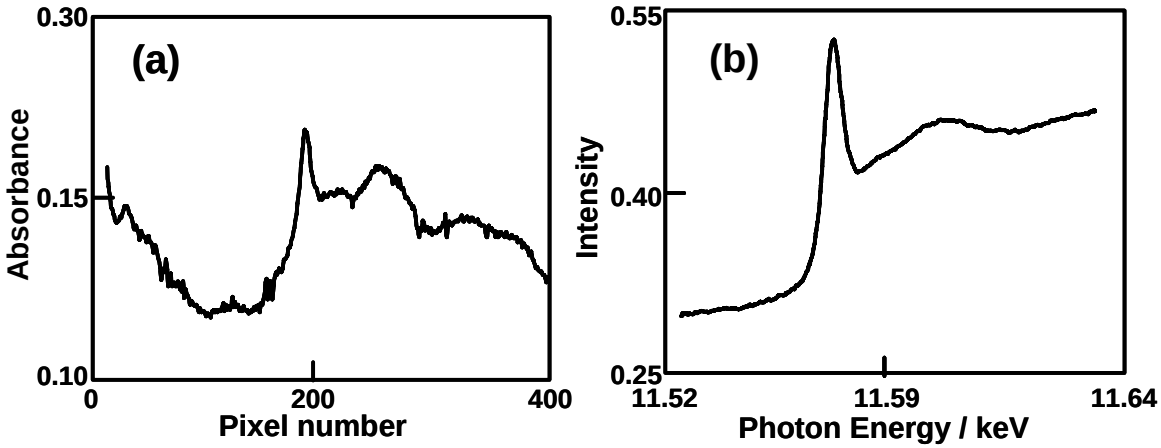

Figure 3. Comparison of Pt L_3-edge XANES spectra of 2 wt% Pt/CZY catalyst which were measured at ID24 of ESRF. (a) D-XAFS in transmission mode with CCD detector. Acquisition time is 3.8 sec per spectrum. (b) T-XAS in fluorescence mode with diode detector. Acquisition time is 1.1 sec per spectrum.

3.2. Correlation between the white-line peak height and Pt particle size

Next, a method to analyze the Pt redispersion was studied. Figure 4-a) shows Pt L_3-edge XANES spectra of Pt/CZY catalyst under oxidizing (20% O_2) / reducing (3% H_2) atmosphere at 400 °C. The ΔI denotes the difference between the white-line peak height of the oxidized and reduced samples. The ΔI did not change under the repetition of oxidizing/reducing conditions at 400 °C. The relationship between the various Pt particle size determined by the CO pulse method and the ΔI is presented in Figure 4-b). The ΔI increases with the decreasing particle size of Pt. This good relation between the ΔI and the Pt particle size suggests that the platinum particles are oxidized only the most surface region, and that the portion of oxidized platinum atoms is proportional to the surface area of platinum particles. As shown in Figure 5, in the case of small Pt particles, ΔI would be large, because the large proportion of Pt particles is exposed to the surface. Meanwhile, in the case of large Pt particles, ΔI would be small compared to the ΔI in small Pt particles. Hence, we can estimate the dispersion of platinum with the ΔI value. Moreover, time-resolved XAS under in-situ conditions enable “in-situ real-time measurements of Pt particle size”.

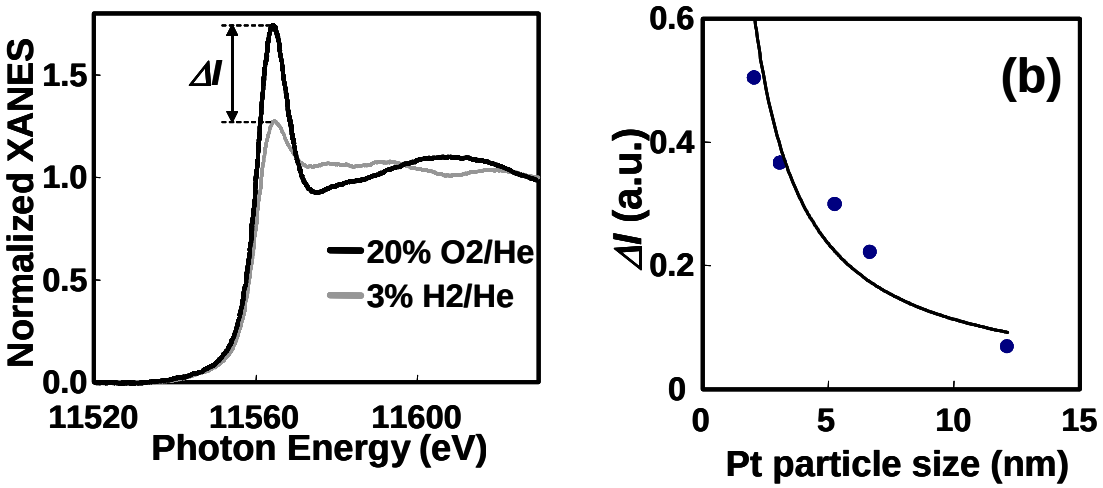

Figure 4. (a) Pt L_3-edge XANES of a Pt/CZY catalyst under oxidizing/reducing atmosphere at 400°C. b) Relationship between Pt particle size and ΔI.

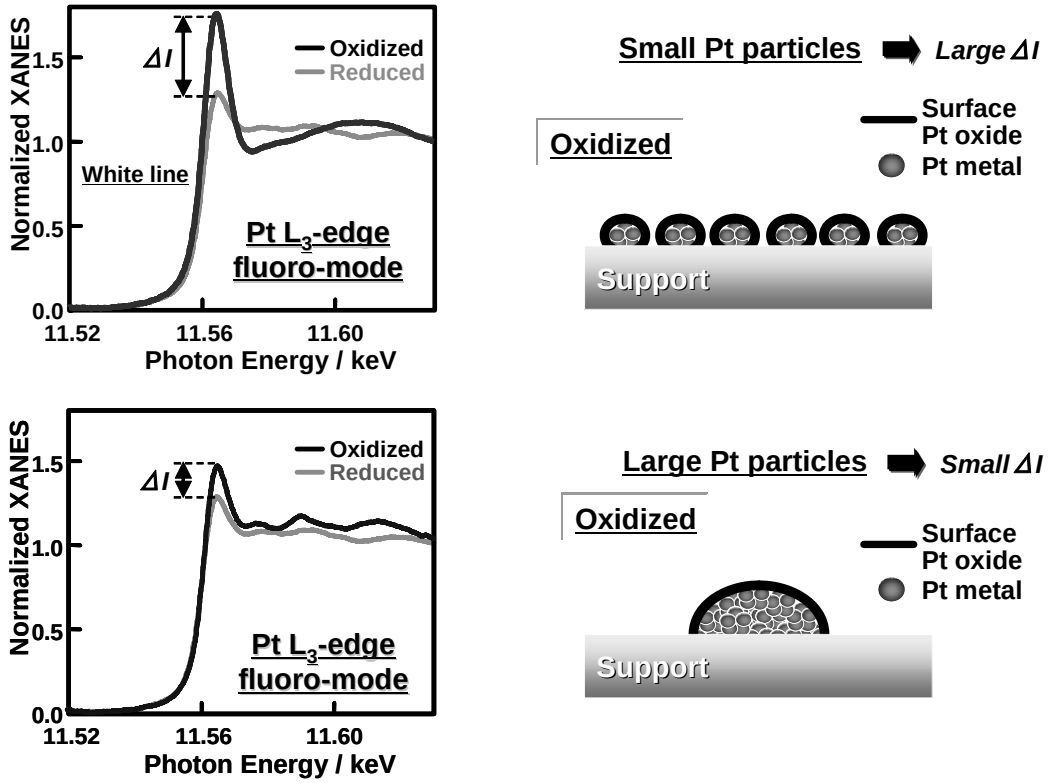

Figure 5. Schematic representations to under stand the relationship between Pt particle size and ΔI.

3.3. Real-time observation of Pt redispersion

A real-time observation of Pt redispersion on a CZY support is presented in Figure 6. The preliminarily sintered Pt/CZY catalyst with Pt particle size of 7 nm determined by the CO pulse adsorption method was used for the redispersion experiment. In this figure, the fluctuations of the white-line peak height of the normalized Pt L_3-edge XANES spectra under cyclical oxidizing/reducing condition at 600°C are shown as a function of time. The white-line peak height changed very quickly, within ~2 seconds, between the values of reduced and that of oxidized Pt after switching the gas atmosphere. This result indicates that the reduction and oxidation of Pt is very fast at 600 °C. While the height of the white-line peak for the reduced catalyst is constant, that for the oxidized catalyst is increased by the amount ΔI. ΔI is seen to gradually increase with time. Using the correlation between the Pt particle size and ΔI in Figure 4-b), this redispersion phenomenon is interpreted as follows. The Pt particle size of the aged catalyst decreases from 7 to 5 nm after 60 seconds, and then to 3 nm after 1000 seconds. This kind of Pt redispersion, not observed in a conventional Pt/Al_2O_3 catalyst, is reasonably attributed to the strong Pt-ceria support interaction [6].

TEM images also confirm the Pt redispaersion phenomena. Figure 7 shows the TEM images for the catalyst before and after the alternate gases treatment, which was used for the redispersion experiment in Figure 6. In the image of before the treatment several nm particles are mostly found, however after the treatment not only several nm but also less than 3 nm particles are observed. In fact, the size distribution of Pt particles after the treatment shifted to lower, compared with the initial state. Thus we have discovered the re-dispersion phenomena for the supported Pt under the cyclical oxidative/reductive gas conditions. These results indicate that the Pt re-dispersion

phenomena can occur in actual operating conditions.

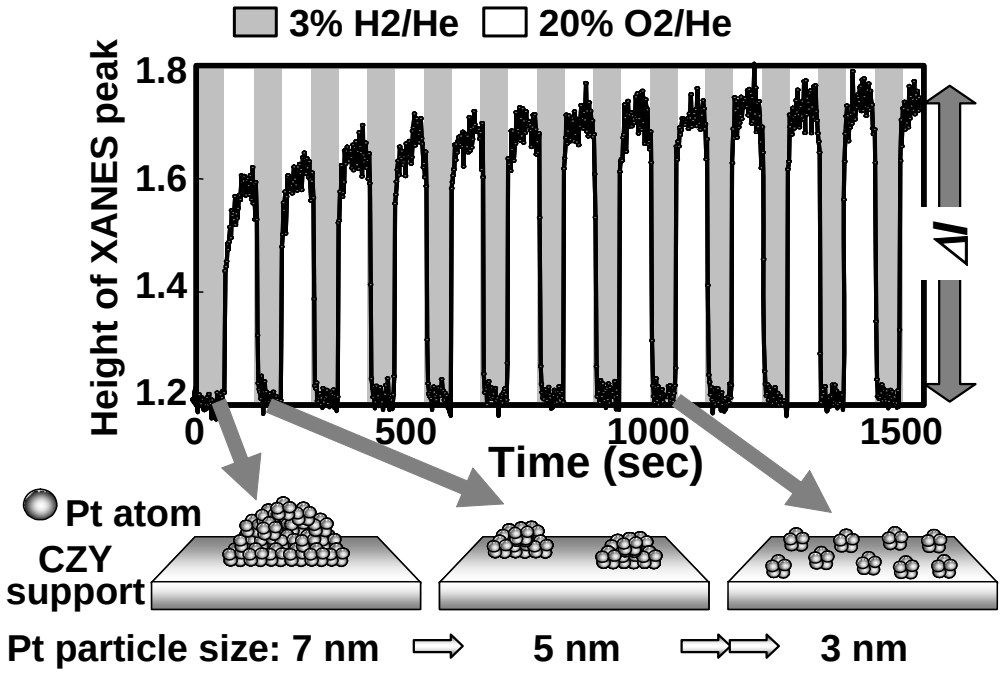

Figure 6. Time course of the XANES peak height for the sintered Pt/CZY catalyst (Pt particle size; 7nm) and the schematic representation of the redispersion behavior. 20% O_2 / He gas and 3% H_2 / He gas were alternately introduced into the cell every 60 seconds at 600 °C throughout the measurements.

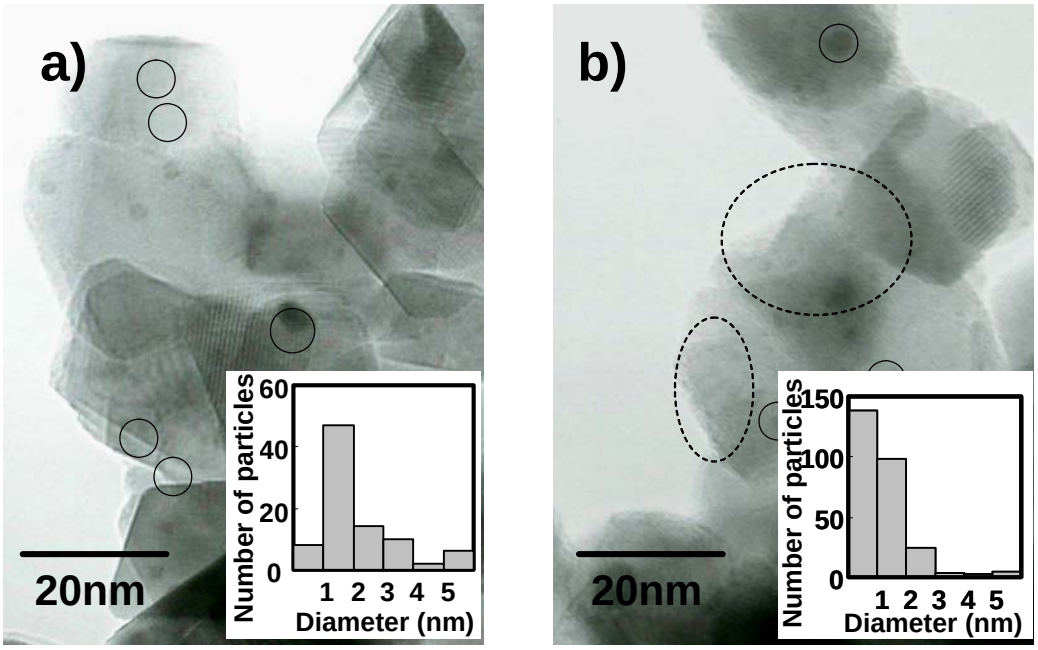

Figure 7. TEM images of for the sintered Pt/CZY catalyst and the size distribution of Pt particles, a) before the treatment, b) after alternate gases treatment.

3.4. Effect of temperature on Pt redispersion

In this section, the effect of temperature on the speed of Pt redispersion was investigated. The preliminarily sintered Pt/CZY catalyst with Pt particle size of 7 nm was used for this experiment. 20% O_2 / He gas and 3% H_2 / He gas were alternately introduced into the cell every 60 seconds at 400, 500, 600 and 700 °C. Figure 8 shows the time course of ΔI in the experiment of the redispersion at 600 °C. The ΔI curve was described one exponential function as the following equation:

$$\Delta I = \Delta I_f - (\Delta I_f - \Delta I_i) \exp(-t/\tau)$$

where ΔI_i and ΔI_f are the initial and final ΔI, respectively, t shows the real time in measurement, and τ is the time constant. The simulation curves calculated by the equation above are also shown in Figure 8. Here, $1/\tau$ gives a definition for the speed of

Pt redispersion. The redispersion speed at 500, 600 and 700 °C were calculated, and presented in Figure 9. As shown in Figure 9, the increase of the temperature tended to give an increase in the speed of the Pt redispersion, suggesting that the thermal energy would accelerate the speed of the Pt redispersion. Additionally, the ΔI did not change under the repetition of oxidizing/reducing conditions at 400 °C. This indicates that high temperature of 500 °C and above are required for the Pt redispersion phenomena.

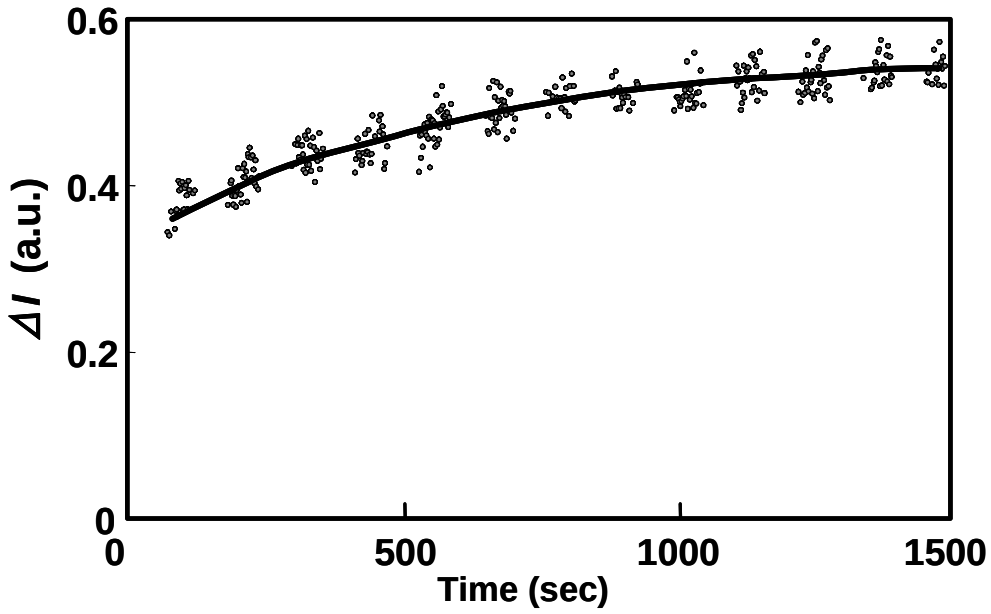

Figure 8. Experimental (dot) and simulation (line) decay curve of of ΔI in the redispersion experiment for the sintered Pt/CZY catalyst (Pt particle size; 7nm) at 600 °C.

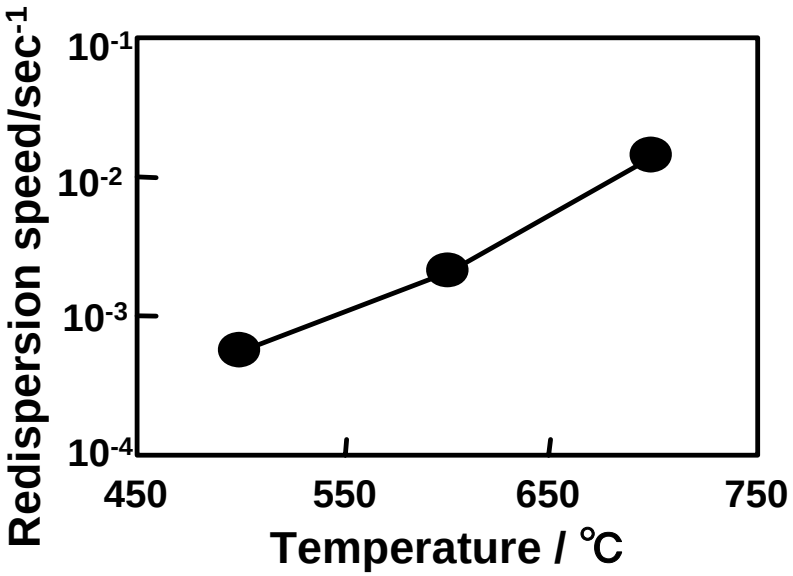

Figure 9. Effect of temperature on Pt redispersion speed.

3.5. Effect of O_2 concentration on Pt redispersion

Next, the effect of O_2 concentration in oxidative gas on Pt redispersion was also investigated. In the same way as the previous section, the preliminarily sintered Pt/CZY catalyst with Pt particle size of 7 nm was used for this experiment. 3, 10 or 20% O_2 / He gas and 3% H_2 / He gas were alternately introduced into the cell every 60 seconds at 600 °C. The redispersion speed for various O_2 concentrations was calculated by the simulation fitting in the same method as the preceding section. Figure 10 shows the redispersion speed as a function of O_2 concentrations in oxidative gas. The redispersion speed of Pt particles increased with increasing O_2 concentration up to 20 mol%. It is postulated that O_2 concentration is the important factor in Pt redispersion.

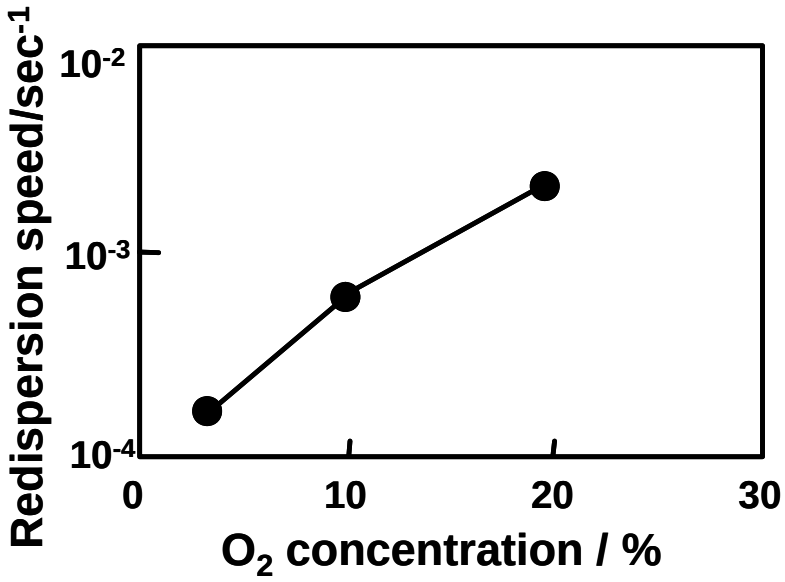

Figure 10. Effect of O_2 concentration on Pt redispersion speed.

3.6. Proposed Mechanism of Pt redispersion

It was found that the rate of Pt redispersion depends on temperature and O_2 concentration. This fact demonstrates that both of the temperature and oxygen is required to produce the redispersion of the aged catalyst. Several mechanisms have been proposed for the dispersion: through volatilization of metals as oxides at temperatures higher than about 500 °C; via atomic migration, causing the migration of atoms or molecules to new regions on the support; through particle break-up, where a single "parent" particle breaks up into two or more smaller particles [7 - 9]. These suggestions are in agreement with our findings on the here studied thermally oxygen-treated catalysts. High temperature and oxygen concentration are required to produce the volatilization of Pt oxides. The schematic representations of Pt redispesion on ceria-based support in presented in Figure 11. As discussed in detail in Chapter 5, the CZY support stabilizes a high-oxidation state of Pt, and then the formation of the rigid

Pt-O-Ce bond acts as an anchor. It is considered that the highly dispersed Pt oxide on the surface of CZY support under oxidizing condition are more stable since the Pt-O-Ce bond energies are greater than the Pt-Pt bond energies in large Pt crystallites. In general, a metal oxide (platinum oxide in the present case) interacts more strongly with the substrate than a metal does [10, 11]. Therefore a strong interaction between Pt oxide and support under oxidative atmosphere is the key to the Pt redispersion. Actually, the Pt redispersion, not observed in a conventional Pt/Al_2O_3 catalyst, is reasonably attributed to the strong Pt-ceria support interaction. On the other hand, during reducing conditions, the Pt-O-Ce bond on the CZY breaks, and Pt oxides are reduced to metal, and then new small particles of Pt metal are formed. It is considered that the Pt redispersion process proceeds by the repetition of the volatilization of Pt oxide from the surface of large metal particles and the reduction of Pt-O-support species.

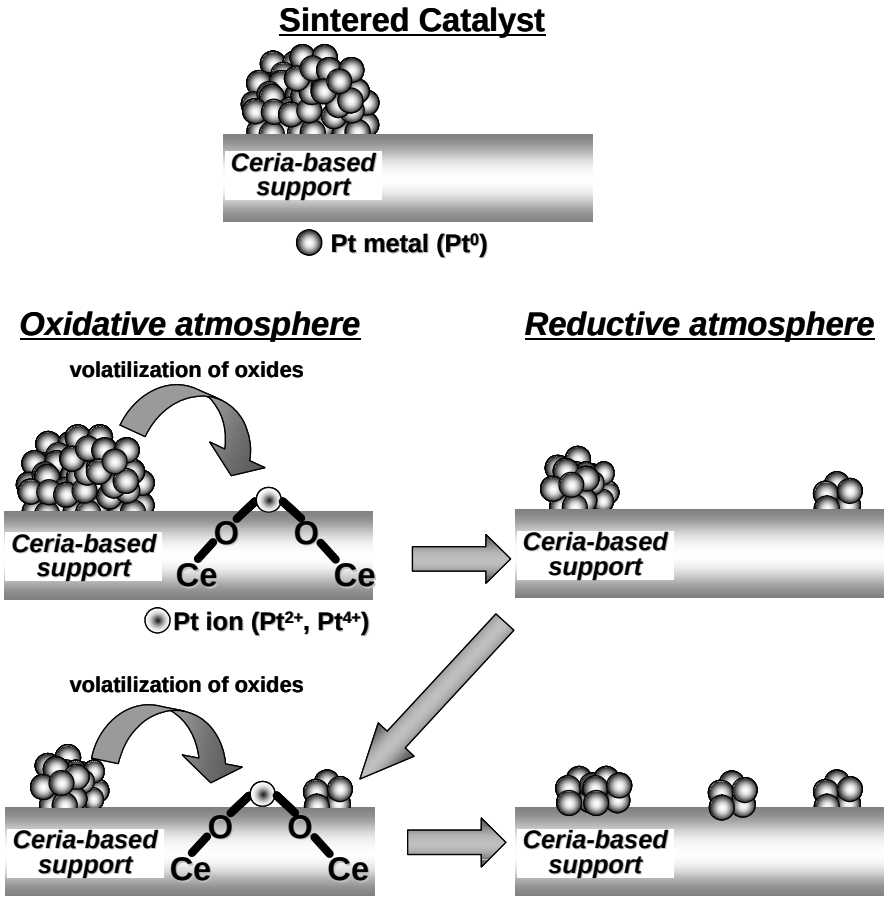

Figure 11. Schematic representations of Pt redispesion on ceria-based support.

4. CONCLUSIONS

First, we have exploited for the first time the in-situ Turbo-XAS technique in fluorescence mode. The low quality of the date in conventional transmission mode is mainly to be attributed to strong X-ray absorption by high loading amount of heavy elements such as Ce and Zr in the Pt/CZY catalyst and thickness inhomogenity of the sample. This Turbo-XAS technique in fluorescence mode technique permitted time-resolved measurements on the second timescale for Pt supported on ceria-based oxide.

Second, we showed that it was possible to perform in-situ real-time measurements of Pt particle size using the white-line height of Pt L_3-edge XANES under oxidative atmosphere. The good relationship between the white-line height and the Pt particle size suggested that the platinum particles are oxidized only the most surface region, and that the portion of oxidized platinum atoms is proportional to the surface area of platinum particles.

Third, we discovered a dynamic redispersion behavior for sintered Pt supported ceria-based oxide catalysts in simulated exhaust flowing. We observed that the Pt particle size of the aged Pt/CZY catalyst decreased from 7 to 5 nm after 60 seconds and then to 3 nm after 1000 seconds at 600 °C.

Finally, we proposed the mechanism of Pt redispaersion. High temperature of 500 °C and above, high concentration of oxygen and strong Pt-oxide-support interaction are required to produce the redispersion of the aged catalyst. The redispersion speed of Pt particles increased with increasing O_2 concentration and the temperature. Additionally, the Pt redispersion was not observed in a Pt/Al_2O_3 catalyst with weak Pt-support interaction. It is considered that the Pt redispersion process proceeds by the

repetition of the volatilization of Pt oxide from the surface of large metal particles under oxidative atmosphere at high temperature of 500 °C and above, and the formation of Pt-O-support species through the strong interaction between the Pt oxide and support.

ACKNOWLEDGMENTS

The author is grateful to Bernard Gorges, Olivier Mathon, Sebastien Pasternak, Florian Perrin, Steven Fiddy (ESRF), Naoyuki Hara, Muriel Lepage, Takashi Kuzuya, (TOYOTA Motor Europe), Takamasa Nonaka, Satoshi Yamaguchi and Yoshiki Seno (TOYOTA Central R&D) for their excellent work.

REFERENCES

[1] S. Matsumoto, *Catal. Today* **90**, (2004) 183.

[2] P.J.F. Harris, *J. Catal.* **97** (1986) 527.

[3] R.M.J. Fiedorow, B.S. Chahar, S.E. Wanke, *J. Catal.* **51** (1978) 193.

[4] C.H. Bartholomew, *Appl. Catal. A* **212** (2001) 17.

[5] . Pascarelli, T. Neisius, S. De Panfilis, *J. Synchrotron Rad.* **6** (1999) 1044.

[6] Y. Nagai, T. Hirabayashi, K Dohmae, N. Takagi, T. Minami, H. Shinjoh and S. Matsumoto, *J. Catal.* **242** (2006) 103.

[7] D.S. Jordan, A.T. Bell, *J. Catal.* **107** (1987) 338.

[8] H.N. Nijs, P.A. Jacobs, *J. Catal.* **66** (1980) 66.

[9] A. Monzon, T.F. Garetto, A. Borgana, *Appl. Cat. A* **248** (2003) 279.

[10] I. Sushumna, E. Ruckenstein, *J. Catal.* **94** (1986) 239.

[11] E. Ruckenstein, I. Sushumna, in "Hydrogen Effects in Catalysis" (Z. Paal and P.G. Menon, Eds.). Dekker, New York, 1987.

[12] T. Uchijima, *Catalytic Science and Technology* (Kodansha-VCH, Weinheim, 1990)

[13] A. Holmgren, B. Andersson, D. Duprez, *Appl. Catal. B* **22** (1999) 215.

Chapter 7: General conclusions

Throughout the physicochemical study of automotive catalysts in this thesis, two principal goals have been attained: (1) The mechanism of OSC improving and thermal degradation of CeO_2-ZrO_2 mixed oxide as an OSC promoter used for TWCs in Chapters 2 and 3, (2) The knowledge of the reaction selectivity, Pt sintering and Pt redispersion on the basis of Pt-support interaction in Chapters 4, 5 and 6. The concrete significance of each chapter is described below, and then the author will describe how these results have contributed to practical application.

Chapter 2 clearly showed the relationship between the OSC and local structure around Ce and Zr in three types of CeO_2-ZrO_2 mixed oxides (Ce:Zr = 1:1 molar ratio) prepared by three different methods. In conclusion, the OSC increases by enhancing the homogeneity of the Ce and Zr atoms in the CeO_2-ZrO_2 solid solution. Especially, an atomically homogeneous "κ-$CeZrO_4$" solid solution with the ordered arrangement of the Ce and Zr cations exhibited the highest OSC among these CeO_2-ZrO_2 samples. The mechanism of OSC improvement was also investigated. The enhancement of the homogeneity of the Ce and Zr atoms could ease the valence change of the Ce (Ce^{4+}→ Ce^{3+}). By the atomically homogeneous introduction of Zr ions into the cubic CeO_2 framework, the Ce-O bond length in the CeO_2-ZrO_2 shortens, and the configuration of the oxygen around Zr has a more centrosymmetric 8-fold coordination. This modification of the local oxygen environment around Ce and Zr will generate some active oxygens for the OSC improvement.

In Chapter 3, the thermal degradation of κ-$CeZrO_4$ and its structure under an oxidative atmosphere at high temperature was studied. The OSC performance deteriorated with increasing temperature. Furthermore, the author found that the κ-structure was still maintained upon aging at 973 K. However, if the temperature went beyond 1273 K, the Ce/Zr ordered arrangement would collapse. A phase separation occurred at 1473 K, and that the $CeZrO_4$ solid solution becomes partially divided into more stable CeO_2 and ZrO_2. The homogeneity of the Ce and Zr atom decreased in the order: the fresh sample ≈ 973 K > 1273 K > 1473 K-aged samples. Moreover, Zr-O and Ce-O geometry also changed remarkably in aged samples. These results indicated that OSC strongly depends on its atomic structure, and hinted us a key point on how to enhance or optimize the oxygen storage performance involved in TWCs.

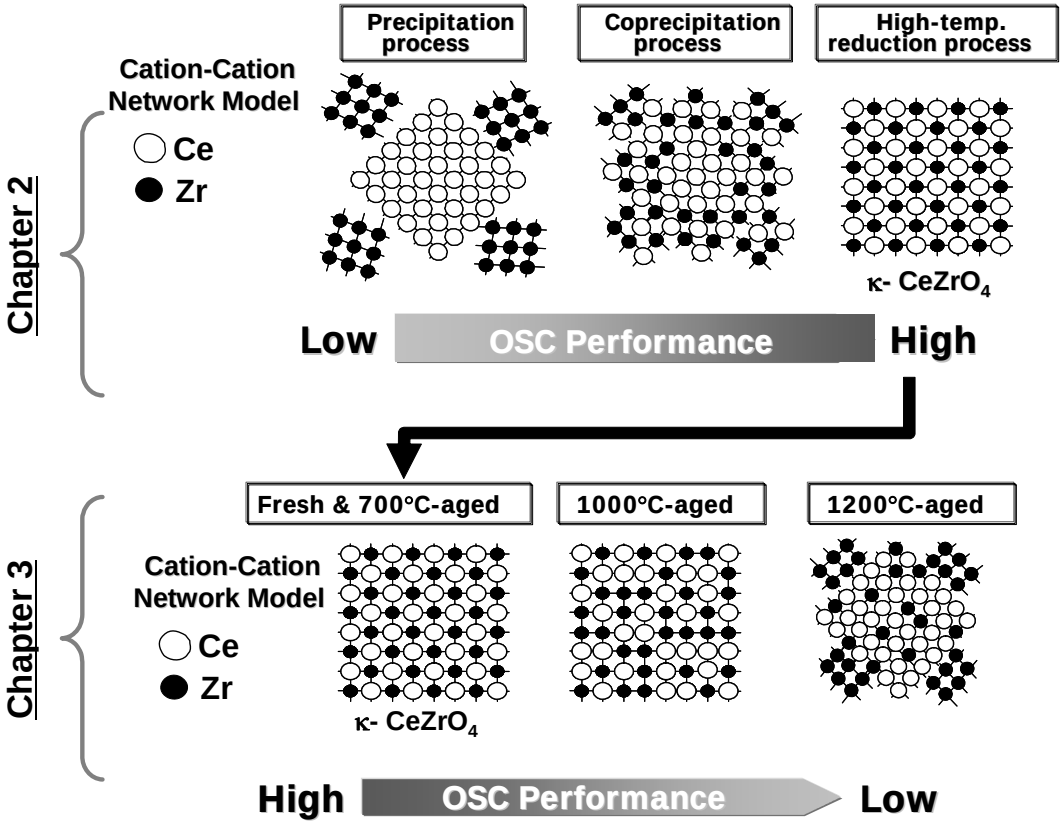

Figure 1. Schematic representations of OSC improvement and thermal degradation under oxidizing condition.

The schematic representations of OSC improvement and thermal degradation are summarized in Figure 1. From the start of development, the author's team aimed at the practical use of κ-$CeZrO_4$ which exhibited the highest OSC among several CeO_2-ZrO_2 samples. However, the thermal durability of κ-$CeZrO_4$ was inadequate for practical use, because the OSC performance of κ-$CeZrO_4$ dramatically drops after ageing test. This degradation caused by the structural change is beyond recovery. The rapid change of OSC performance has an adverse affect on engine control. Simultaneous pursuit of high performance and high thermal stability are essential function for practical use. Therefore, OSC material has been developed on the basis of CZ55-2 which has a sufficient performance and high thermal stability. The deep understanding based on scientific notion can eradicate trouble in the market and provide highly dependable vehicles. The developed material, which was based on this research, has been already on-board to most TOYOTA's gasoline vehicles all over the world. The synchrotron radiation based analysis made a big contribution to practical use.

In Chapter 4, the reaction selectivity for the *n*-C_6H_{14} and SO_2 oxidations over two types of Pt/ZrO_2 catalysts with low and high ZrO_2 support surface areas was estimated. The Pt/ZrO_2-75 catalyst with a high surface area has a desirably higher selectivity for the complete oxidation of *n*-C_6H_{14} than that of SO_2, as compared with the Pt/ZrO_2-8 catalyst with a low surface area. The number of Pt^0 (metal) sites in the Pt/ZrO_2-75 was significantly lower than that in the Pt/ZrO_2-8, because the strong interaction between the Pt and the ZrO_2-75 stabilized the high oxidation state of Pt such as Pt^{2+} and Pt^{4+}. Since the reaction rate for the SO_2 oxidation is much slower than that for the *n*-C_6H_{14}

oxidation, the decrease in the active Pt^0 site apparently suppresses the SO_2 oxidation as compared with the *n*-C_6H_{14} oxidation.

The sintering inhibition mechanism of Pt particles on CZY and Pt-oxide–support interaction was studied in Chapter 5. Pt supported on ceria-based oxide (CZY) did not sinter under oxidizing condition at 800 °C while Pt atoms on Al_2O_3 sinter significantly. Pt particles in the Pt/Al_2O_3 grew up to 23.6 nm during the ageing treatment. The author clarified that the sintering inhibition mechanism of Pt particles on CZY at the atomic level by using XAFS analysis. Pt supported on CZY had a strong interaction with the CZY support. Therefore the CZY support stabilized high-oxidation state of Pt under oxidizing condition at high-temperature, and then the rigid Pt-O-Ce bond, that is, the Pt-oxide-support interaction generated. The Pt-O-Ce bond acted as an anchor, and inhibited Pt migration. As a result of further systematic investigation on various Pt catalysts, it was clear that there was an excellent correlation between the strength of the Pt-oxide-support interaction and the electron density of oxygen in the support oxide. The sintering inhibition effect on Pt can be controlled by the electron density of oxygen in the support through the Pt-oxide-support interaction.

As described above, Pt particles supported on ceria-based oxide does not sinter under oxidizing condition at 800 °C. However, even Pt/ceria-based oxide catalyst would sinter at higher temperature of 900 °C and above. In Chapter 6, a dynamic redispersion behavior for sintered Pt supported ceria-based oxide catalysts in simulated exhaust flowing could be observed by using a novel technique of in-situ time-resolved Turbo-XAS in fluorescence mode. The Pt particle size of the aged Pt/CZY catalyst decreased from 7 to 5 nm after 60 seconds and then to 3 nm after 1000 seconds at 600 °C. Moreover, the mechanism of Pt redispersion was proposed. High temperature of

500 °C and above, high concentration of oxygen and strong Pt-oxide-support interaction were required to produce the redispersion of the aged catalyst. It was considered that the Pt redispersion process proceeds by the repetition of the volatilization of Pt oxide from the surface of large metal particles under oxidative atmosphere at high temperature of 500 °C and above, and the formation of Pt-O-support species through the strong interaction between the Pt oxide and support.

From the studies in Chapters 4, 5 and 6, Pt regeneration cycle has been established, as shown in Figure 2. Pt in Pt/ceria-based oxide catalyst does not sinter at all up to 800 °C, because the rigid Pt-O-Ce bond, that is, the strong Pt-oxide-support interaction generates. The Pt-O-Ce bond acted as an anchor, and inhibited Pt migration (Chapter 5). However, even Pt/ceria-based oxide catalyst would sinter at higher temperature of 900 °C and above. So, sintered Pt particles on ceria-based oxide can be dispersed under oxidizing condition at the temperature ranging from 500 to 800 °C. The strong Pt-oxide-support interaction is required to produce the Pt redispersion (Chapter 6). It was considered that Pt^0 (metal) is the active site for the catalytic reaction in automotive exhaust condition (Chapter 4). The ceria-based support stabilizes a high-oxidation state Therefore, Pt on ceria-based support has to be reducible during the catalytic reaction. Under stoichiometric or reducing conditions, the Pt-O-Ce bond on the CZY breaks and then new small particles of Pt metal are formed (Chapter 5 and 6). The Pt sintering inhibition technique in the Pt regeneration cycle, which was based on this research, was put to practical use for some of TOYOTA's gasoline vehicles in 2005. Concerning the Pt redispersion technique, a precise and complicated engine control is required to take full advantage of this technique, because Pt redispersion occurs within a limited operation area. The author deeply hopes this technique will be on-board to TOYOTA's vehicles in

near future.

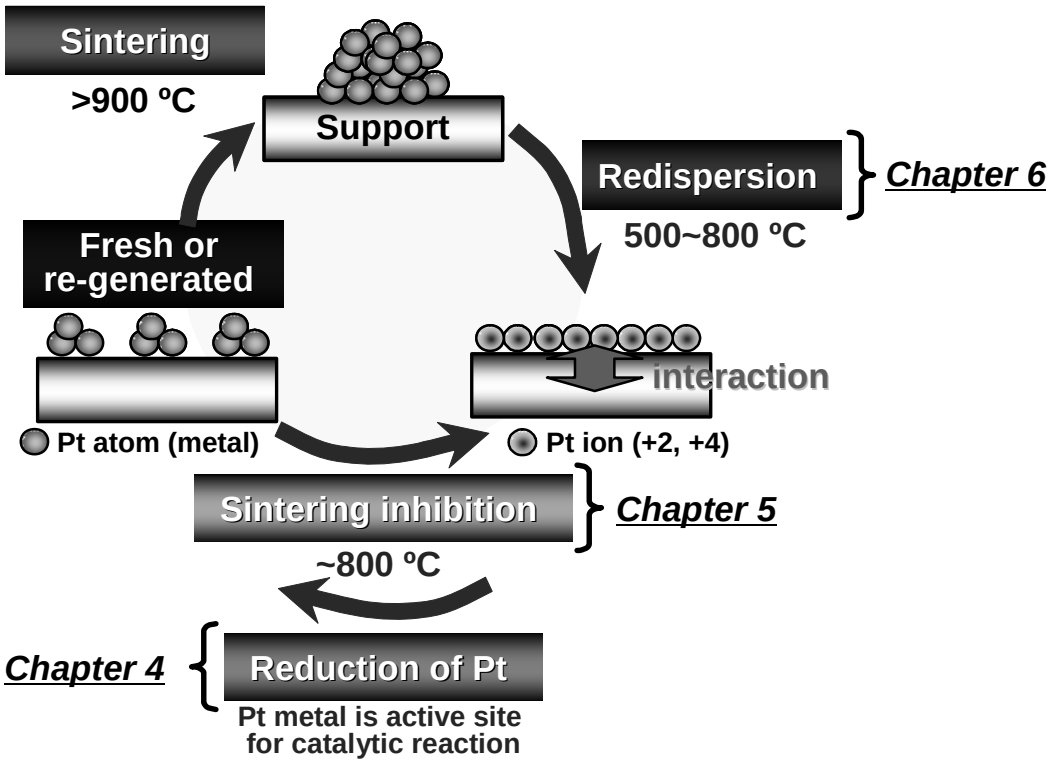

Figure 2. Regeneration cycle of Pt/Ceria-based oxide catalyst.

In this thesis, a wide variety and number of analysis techniques were used to investigate physicochemical properties of automotive catalysts in accordance with the purpose. The analysis techniques used in each chapter are summarized in Table 1. X-ray absorption spectroscopy was mainly used to study the structural and electronic properties of catalysts. Recent progress of synchrotron radiation analysis has been achieving a remarkable breakthrough. XAFS measurements in Chapters 2, 3 and 5 were carried out in air at room temperature, in order to make a structural analysis in a static state. On the other hand, XAFS spectra of Chapter 6 were measured under in-situ condition to investigate the dynamic change of Pt. Exhaust condition from a gasoline

engine changes quickly and dramatically, in response to an operation. Temperature goes up to around 1000 ºC, and gas condition fluctuates between oxidative and reductive atmospheres. Therefore, in-situ dynamic observation will take an important role in the field of XAFS analysis of automotive catalysts.

This synchrotron-based analysis technique gains a deeper appreciation on catalysts. A basic understanding of the structure of automotive catalysts at an atomic level will change the development process of the catalysts and can pave the way for planed catalytic design, rather than adopting a trial-and-error approach. Of course, the XAFS analysis is not an all-powerful tool. It is important to synthetically investigate them in combination with other analytical method.

Table 1. Summary of analysis techniques used in each chapter.

	Catalyst & Purpose	Analysis technique	
		Physical property	Chemical property
Chapter 2	Ceria-Zirconia OSC performance and its atomic structure	B.E.T: surface area XRD: phase EXAFS: molecular structure XANES: oxygen environment	T.G.: OSC performance
Chapter 3	Ceria-Zirconia Structural change along with the thermal degradation	B.E.T: surface area XRD: phase EXAFS: molecular structure XANES: oxygen environment	T.G.: OSC performance
Chapter 4	Pt supported on Zirconia Reaction selectivity and Pt-support interaction	B.E.T: surface area XRD: phase TEM: particle size	CO-IR: oxidation state CO_2-TPD: basicity XPS: oxidation state Flow reactor: catalytic activity
Chapter 5	Pt supported on Ceria-based oxide Pt sintering inhibition and Pt-support interaction	B.E.T: surface area XRD: phase EXAFS: molecular structure TEM: particle size CO-pulse: particle size	XANES: oxidation state EXAFS: Pt-support interaction XPS: oxidation state
Chapter 6	Pt supported on Ceria-based oxide Pt redispersion and Pt-support interaction	TEM: particle size CO-pulse: particle size XANES: particle size	XANES: oxidation state

List of Publications

Publications Related to Work Described in This Thesis

Chapter 2:

1. Y. Nagai, T. Yamamoto, T. Tanaka, S. Yoshida, T. Nonaka, T. Okamoto, A. Suda and M. Sugiura, *Journal of Synchrotron Radiation* **8** (2001) 616.
   "Local Structure Analyses of $Ce_{0.5}Zr_{0.5}O_2$ Mixed Oxides by XAFS"

2. Y. Nagai, T. Yamamoto, T. Tanaka, S. Yoshida, T. Nonaka, T. Okamoto, A. Suda, M. Sugiura, *Catalysis Today* **74** (2002) 225.
   "X-ray Absorption Fine Structure Analysis of Local Structure of CeO_2－ZrO_2 Mixed Oxides with the Same Composition Ratio (Ce/Zr = 1)"

Chapter 3:

3. Y. Nagai, T. Yamamoto, T. Tanaka, T. Nonaka, A. Suda, *Physica Scripta* **T115** (2005) 664.
   "Study on the Thermal Degradation of CeO_2-ZrO_2 solid Solution by XAFS and XRD"

4. Y. Nagai, T. Yamamoto, T. Tanaka, S. Yoshida, T. Nonaka, T. Okamoto, A. Suda, M. Sugiura, *Topics in Catalysis*, in press (2007)
   "XAFS and XRD Analysis of Ceria-Zirconia Oxygen Storage Promoters for Automotive Catalysts"

Chapter 4:

5. Y. Nagai, H. Shinjoh, K. Yokota, *Applied Catalysis B Environmental* **39** (2002) 149.
   "Oxidation Reaction of n-Hexane and Sulfur Dioxide in Diesel Simulated Exhaust Gases over Platinum Loaded Zirconia"

Chapter 5:

6. Y. Nagai, T. Hirabayashi, K Dohmae, N. Takagi, T. Minami, H. Shinjoh and S. Matsumoto, *Journal of Catalysis* **242** (2006) 103.

"Sintering Inhibition Mechanism of Platinum Supported on Ceria-based Oxide and Pt-oxide–support Interaction"

Chapter 6:

7. Y. Nagai, N. Takagi, Y. Ikeda, K. Dohmae, T. Tanabe, G. Guilera, S. Pascarelli, M. Newton, H. Shinjoh, S. Matsumoto, *Studies in Surface Science and Catalysis*, in press (2007).
   "Real-time Observation of Platinum Redispersion on Ceria-based Oxide by In-situ Turbo-XAS"

Publications Not Included in This Thesis

[Original Papers]

1. T. Funabiki, I. Yoneda, M. Ishikawa, M. Ujiie, Y. Nagai, S. Yoshida, *J. Chem. Soc. Chem. Comm.* **12** (1994) 1453.
   "Extradiol Oxygenation of 3,5-di-tert-Butylcatechol with O_2 by Iron Chlorides in Tetrahydrofuran-Water as a Model Reaction for Catechol-2,3-Dioxygenases"

2. T. Funabiki, M. Ishikawa, Y. Nagai, J. Yorita, S. Yoshida, *J. Chem. Soc. Chem. Comm.* **17** (1994) 1951.
   "Activation of Chelated Catecholatoiron Species for Catalytic Oxygenation of Catechols by Catecholdioxygenase-Model Iron Complexes"

3. T. Funabiki, Y. Nagai, H. Kojima, T. Tanaka, S. Yoshida, H. Masuda, *Inorg. Chim. Acta* **275-276** (1998) 222.
   "X-ray Crystallographic and Absorption Spectroscopic Analyses of Structures of Catecholato(pyridine)iron Chloride Complexes in Relevance to Functional Model Complexes for Catechol 1,2-dioxygenases"

4. F. Dong, A. Suda, T. Tanabe, Y. Nagai, H. Sobukawa, H. Shinjoh, M. Sugiura, C. Descorme, D. Duprez, *Catalysis Today* **90** (2004) 223.
   "Characterization of the Dynamic Oxygen Migration over Pt/CeO_2-ZrO_2 Catalysts by O-18/O-16 Isotopic Exchange Reaction"

5. F. Dong, A. Suda, T. Tanabe, Y. Nagai, H. Sobukawa, H. Shinjoh, M. Sugiura, C. Descorme, D. Duprez, *Catalysis Today* **93** (2004) 827.
   "Dynamic Oxygen Mobility and a New Insight into the Role of Zr Atoms in Three-way Catalysts of Pt/CeO_2-ZrO_2"

6. A. Suda, Y. Ukyo, K. Yamamura, H. Sobukawa, T. Sasaki, M. Sugiura, T. Tanabe, Y. Nagai, *Journal of the Ceramic Society of Japan* **112** (2004) 586.
   "Effect of ordered arrangement of Ce and Zr ion on oxygen storage capacity of Ceria-Zirconia solid solution"

7. A. Suda, K. Yamamura, Y. Ukyo, H. Sobukawa, T. Sasaki, T. Tanabe, Y. Nagai, M. Sugiura, *Journal of the Ceramic Society of Japan* **112** (2004) 581.

"Effect of specific surface area of ceria-zirconia solid solutions on their oxygen storage capacity"

8. A. Suda, K. Yamamura, H. Sobukawa, Y. Ukyo, T. Tanabe, Y. Nagai, F. Dong, M. Sugiura, *Journal of the Ceramic Society of Japan* **112** (2004) 623.
"Effect of the amount of pt loading on the oxygen storage capacity of ceria-zirconia solid solution"

9. A. Suda, K. Yamamura, A. Morikawa, Y. Nagai, H. Sobukawa, Y. Ukyo, H. Shinjoh, *Journal of Materials Science*, in press (2007)
"Atmospheric Pressure Solvothermal Synthesis of Ceria-Zirconia Solid Solutions and Their Large Oxygen Storage Capacity"

[Reviews, Overviews, Proceedings and Books]

1. Y. Nagai, T. Yamamoto, T. Tanaka, *SPring-8 Research Frontiers*, 1999/2000, p. 46-49.
"XAFS Analysis on Local Structure of CeO_2-ZrO_2 Mixed Oxides"

2. Y. Nagai, H. Shinjoh, K. Yokota, *R&D Review of Toyota CRDL* **37(1)** (2002) 51.
"Oxidation Selectivity btween n-Hexane and Sulfur Dioxide in Diesel Simulated Exhaust Gas over Platinum-Supported Zirconia Catalyst"

3. Y. Nagai, T. Nonaka, A. Suda, M. Sugiura, *R&D Review of Toyota CRDL* **37(4)** (2002) 20.
"Structure analysis of CeO_2-ZrO_2 mixed oxides as oxygen storage promoters in automotive catalysts"

4. Y. Nagai, T. Hirabayashi, K Dohmae, N. Takagi, T. Minami, H. Shinjoh and S. Matsumoto, *R&D Review of Toyota CRDL* **41(4)** (2006) 32.
"Sintering Inhibition Mechanism of Platinum on Ceria-based Oxide Support for Automotive Catalysts"

5. Y. Nagai, N. Takagi, Y. Ikeda, K. Dohmae, T. Tanabe, G. Guilera, S. Pascarelli, M. Newton, H. Shinjoh, S. Matsumoto, *AIP conference proceedings* **882** (2007) 594.
"Real-time Observation of Platinum Redispersion on Ceria-based Oxide by In-situ

Turbo-XAS in Fluorescence Mode”

6. Y. Nagai, *Housyakou* **15** (2002) 37.
   “XAFS Analysis of CeO_2-ZrO_2 Mixed Oxides as Oxygen Storage Promoters in Automotive Catalysts” (in Japanese)

7. Y. Nagai, T. Tanabe, *Materials Integration* **16** (2003) 39.
   “Dynamical Oxygen Storage/Release Behavior and Structural Characterization of Ceria-Zirconia” (in Japanese)

8. Y. Nagai, *Materials Integration* **19** (2006) 15.
   “XAFS and XRD Analysis of Ceria-Zirconia Oxygen Storage Promoters for Automotive Catalysts” (in Japanese)

9. Y. Nagai, *Development of Catalyst State-of-the-art on the Basis of the Utilization of High Emittance Synchrotron Radiation from SPring-8,* NTS, Japan (2006) p.305, (ISBN4-86043-137-5)
   “XAFS Analysis of CeO_2-ZrO_2 Mixed Oxide, Oxygen Storage Material for Automotive Catalyst” (in Japanese)